UNIVERSITAT POLITÈCNICA DE CATALUNYA
BARCELONATECH

ICFO
The Institute of Photonic Sciences

Micro-structured ferroelectric superlattice for efficient acousto-optic devices

Didit Yudistira

Thesis Advisor: Dr. Valerio Pruneri

Thesis Co-advisor: Dr. Davide Janner

PhD Thesis

2011

This thesis is dedicated to my late parents....

CONTENTS

LIST OF TABLES

LIST OF FIGURES

LIST OF NOTATIONS

F	Acoustic frequency
v	Acoustic velocity
λ	Acoustic wavelength
Λ	Gratings period
k	Acoustic wavenumber
u	Acoustic displacement
S	Acoustic strain
T	Acoustic stress
c	Stiffness constant
e	Piezoelectric constant
E	Electric field
D	Electric displacement
ε	Permittivity constant
ϕ	Electric potential
B	Magnetic field
ρ	Mass density of the crystal
Ω	Angular frequency of acoustic wave
P	Acoustic power
$\bar{W}$	Acoustic energy
K^2	Electromechanical coupling coefficient
C	Static capacitance
V	Applied voltage
p	Photoelastic constant
ΔB	Dielectric impermeability

LIST OF NOTATIONS

n	Refractive index
N	Effective refractive index
r	Electrooptic constant
β	Optical or acoustical mode propagation
λ_0	Optical wavelength
η	Optical mode conversion efficiency
M	Figure of merit
κ	Acousto-optic coupling coefficient
P_0	Optical power
I	Optical intensity
Y	Complex admittance
W	Width of the coplanar electrodes
G_E	Gap between the electrodes
C_T	Capacitance of the electrodes
G_a	Radiation conductance of the transducer
S	Scattering parameters

ACKNOWLEDGMENT

This thesis would not be exist without the help and support of the kind people around me. Foremost, I would like to gratefully thank my supervisor Valerio Pruneri, who has supported me throughout my PhD, and for his guidance on this research topic and his motivation. He has thought me to be pragmatic and to stay focus on obtaining results that matter, which has somewhat changed the way I see the world of research and my approach in doing research in general. Many thanks also to committee members: Christopher Pannell, Sakellaris Mailis, David Artigas, Maria-Pilar Bernal Artajona, and Marc De Micheli, for reviewing and examining my thesis.

Many people who were in direct way involved during my PhD work at ICFO, they have my sincere gratitude. In particular I am very thankful to Sarah Benchabane who has introduced me to the world of acoustics. She has kindly shared her knowledge of device fabrications and also patiently showed me how to properly execute the work in the clean room, and has helped me in many ways throughout my PhD. I would like to thank Davide Janner for his assistance and valuable advice in science discussion. He has kindly shared his knowledge of optical characterizations, simulations, and preparation of the devices among others, also with whom I discuss about various topics beside science ranging from Italian foods to geeks stuffs. I want to thank Vittoria Finazzi who has helped me with Labview program so that I was able to work with our ancient Network Analyzer long before brand new analyzer arrived in the

lab. I want to thank Carme Gómez for her assistance in the PPL lab. I want to thank Daniel Infante for spanish translation of this thesis abstract. I want thank my PhD fellows, Domenico Tulli and Dhiriti Gosh, whom I shared about commons PhD stuffs with and for being nice office mates and I would like also to extend my thankfulness to all members of Opto group whom I cannot mention one by one. Furthermore, I would thank all people in ICFO administration, in particular Manuela Furkert, Anne Gstöttner, Maria José Martínez Villellas, and Maria del Mar Gil Sánchez.

I thank my Indonesian and Malaysian friends in Barcelona: Mas Fahmi and Mba Emmy and family, Pak Nino and Mba Anggi, Indra, Zul and Merlinda for their warm friendship during my PhD years.

Lastly and most importantly I want to thank my family. The support, encouragement, and endless patience from my beloved wife Fiska have given my PhD life in Barcelona enjoyable and unforgettable. She has given me a joyful baby boy Fatir who becomes my motivation and source of energy to finish my thesis. Special acknowledgment is dedicated to my late parents whom I dearly miss.

Chapter 1 - Introduction

1.1 Background

Optical fiber telecommunication plays a key role in our daily life and has allowed the internet era. In early days, optical fiber telecommunication was established based on point-to-point optical links that generally consisted of one light source at the transmitting end, one photodetector at the receiving end, and a single optical fiber that connects the two terminals [1].

Wavelength-division multiplexing (WDM) [2-5] or Dense WDM (DWDM) [6] optical communication systems have been introduced as an immediate solution to improve the capability of the point-to-point fiber telecommunication system. A WDM system allows increasing the capacity of the optical fiber without replacing the fiber cable plant, thus being an economically viable solution. This is possible as WDM enables different independent wavelengths (channels) to be transported along the same optical fiber as if each wavelength was being carried by a dedicated fiber, producing a huge increase of overall data bandwidth.

A narrowband optical filter is a key component of a WDM system. The filter is applied for selecting or adding one channel from the wavelength-multiplexed signal. It is crucial that signals outside of filter passband are sufficiently suppressed in order to avoid cross talks among neighboring channels. In addition, if the efficiency of the filter in the passband is high then it will reduce the

need of optical amplifiers. Figure 1.1 pictures the functional features of a narrowband add and drop filter for WDM and DWDM communication systems.

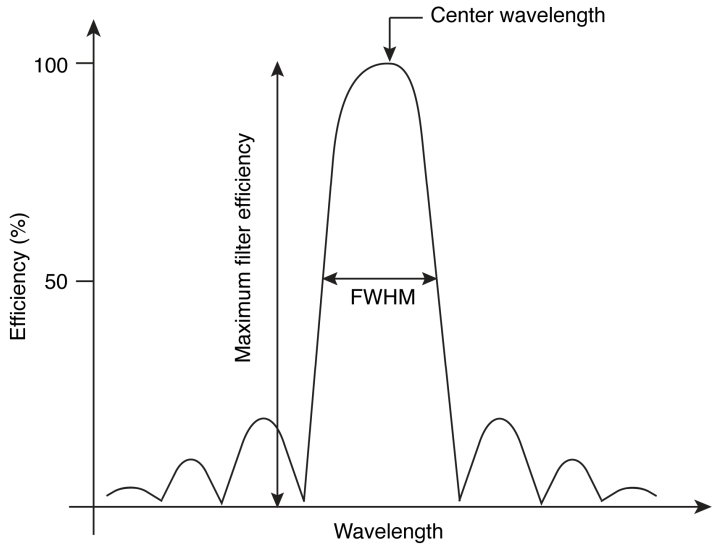

Figure 1.1: Add and drop filter characteristics.

An add and drop filter for WDM or DWDM has several specifications, including:

- Center wavelength located at around one of the telecommunication windows, e.g. 1550 nm
- High filter efficiency, i.e. optical conversion vs. electrical power
- Narrow bandwidth (FWHM), still large enough to allocate the channel bandwidth
- Low “cross-talk”, i.e. high side mode suppression
- Polarization insensitivity

In addition to those, with the advent of reconfigurable WDM or DWDM systems, the filter should possess wavelength tunability, either for functionality reasons in tunable networks or for reducing spare-parts inventory in fixed wavelength networks. Acousto-optic (AO) filters can meet these requirements, thus have the potential to become widely used devices in optical communication systems.

In this thesis we will investigate and develop a new class of integrated (waveguide) AO filters based on domain inverted superlattices. The building blocks of the integrated AO filter include a polarization converter and two linear polarizers at the input and output of the converter. The polarization converter allows a rotation of the polarization selected by the input linear polarizer through an AO interaction. The second polarizer sets the transmission of the device depending on the polarization rotation. The polarization converter is based on a piezoelectric (acoustic) medium with also good optical properties to make a low loss optical waveguide, in our case $LiNbO_3$. That combines acoustic, optical and the possibility to create domain inverted piezoelectric superlattices.

1.2 State-of-the-art and novelty of the thesis

1.2.1 Surface acoustic wave devices

The acoustic transducer is a key component in AO filters since it allows generating the acoustic wave from the electrical signal. The acoustic wave will then interact with the optical wave to produce the designed AO interaction. In the case the AO interaction takes place in an optical waveguide, it is necessary to generate a

surface acoustic wave (SAW). Interdigitated transducers (IDTs), which were introduced for the first time by White and Voltmer [7] are widely used for SAW generation, hence in integrated (waveguide) AO filters. As the voltage is applied to two series of electrode fingers, the electric field between the fingers penetrates into the substrate and, due to the piezoelectric coupling, an acoustic wave can be excited. Conversely, when the acoustic wave is present in the material, due to the inverse piezoelectric effect, it can be transformed back to electric field and voltage. Therefore, the IDTs can simultaneously operate as a transmitter and receiver of time dependent electrical signals. Nowadays, SAW finds a wide range of applications, in particular in RF-electronics, where SAW devices are used for signal processing and frequency filtering [8].

The SAW frequency (f_R) depends on the intrinsic SAW velocity (v_R) of the piezoelectric medium and on the electrode geometry given by the period (Λ), according to the following expression

$$f_R = v_R / \lambda_R \tag{1.1}$$

where λ_R is acoustic wavelength and $\lambda_R = 2\Lambda$. The SAW velocity (v_R) strongly depends on the crystal orientation of the piezoelectric material. Typical velocities of acoustic waves range from 3000 m/s to 6000 m/s for ferroelectric crystals such as $LiNbO_3$ substrate. The operating frequency (f_R) could be increased either by increasing v_R or by decreasing Λ. Attempts to reduce the period (Λ) to increase the operating frequency would be limited by the processing

technology that is currently available, namely photo lithographic process. For example to fabricate 0.8 microns of feature size with standard photo lithography processes is not easy, if not impossible. The maximum achievable frequency of most existing SAW devices based on IDTs is thus in practice estimated to be approximately 2 GHz. The limitation due to fabrication could be overcome by utilizing more advances fabrication techniques, such as electron beam lithography. However these techniques are not economic enough for large-scale production.

Several authors have also tried to increase the operating frequency by investigating SAW propagating with higher acoustic velocity v_R, such as leaky SAW (L-SAW). The velocity of L-SAW, for example propagating in 36 YX-cut $LiTaO_3$ substrate, is about 4100 m/s [9]. From a practical point of view, L-SAW may be achieved using layered configurations where a piezoelectric thin film, such as ZnO, is deposited onto non piezoelectric medium like sapphire, diamond, and silicon carbide, with the latter functioning only as the medium for the interaction between the acoustic and optical waves. However, piezoelectric films deposited by sputtering are polycrystalline, that means the propagation loss tends to be higher than that in monocrystalline bulk material. Furthermore, surface-wave properties, such as velocity and coupling coefficient, are also sensitive to the thickness of the film, and, consequently, the thickness of the film needs to be precisely controlled.

Instead of using polycrystalline material, some authors use monocrystalline bulk substrates to excite different kinds of high

velocity SAW, longitudinal L-SAW (LL-SAW) being an example [10], [11]. The phase velocity of LLSAW is around 6100 m/s. The LLSAW exists in certain highly anisotropic crystal materials, such as lithium tetraborate ($Li_2B_4O_7$) [12]. The LL-SAW may also exist in $LiTaO_3$ and $LiNbO_3$, only when relatively thick electrode gratings are present [13].

In this thesis a new approach for SAW excitation will be employed. The main aim is to achieve higher efficiency in AO devices besides improving the operating frequency. Here, instead of using standard interdigitated metallic fingers deposited on homogenous piezoelectric substrate to generate the SAW, the so-called acoustic superlattice (ASL) is employed.

The building block of the ASL is a ferroelectric crystal where its domains are inverted using ad-hoc electrical poling techniques. Due to domain inversion, all odd rank tensors, e.g. piezoelectric tensors, change sign, from positive to negative from one domain to the next, whereas all even rank tensor, such as refractive index, elastic constant, are unaltered. When an alternating time-variant uniform external electric field is applied, the domain walls will be subjected to a periodic strain because of periodic change of piezoelectric coefficient, effectively resulting in a sound source. This is the basic principle of acoustic wave excitation in ASL.

The configurations of ASL can be divided into two schemes depending on the direction of electric field, namely “in-line” when the electric field is parallel to the propagation direction, whereas

"crossed-field" scheme when the field is perpendicular to the direction of wave propagation [14], [15]. The advantage of the ASL approach consists in the fact that the SAW can be launched using uniform electrodes, such as coplanar electrode configuration. In ASL, the SAW frequency is inversely proportional to the period of the domain inverted grating, following Eq. (1.1) with $\lambda_R = \Lambda$. That means the operating frequency of the acoustic transducer that can be achieved is in principle twice the frequency that can be obtained from standard IDTs with the same period. Therefore the ASL approach has great potentials in AO applications and high operating frequency.

1.2.2 Acousto-optic filters

Depending on the acoustic wave utilized in the AO interaction, AO filters can be divided into two main categories: bulk AO filters [16-23] and integrated (waveguide) AO filters [24-32]. Bulk AO filters involve interaction between a bulk acoustic wave and the optical field whereas integrated AO filters rely on surface acoustic wave (SAW) interacting with optical signals that propagate inside an optical waveguide. The bulk AO filters usually consist of a thin piezoelectric acoustic transducer, e.g. made of $LiNbO_3$, to generate acoustic wave that is attached to a single domain AO crystal (Bragg cell), e.g. made of TeO_2. Despite a steadily improvement [17] in performance ,since they were introduced for the first time [23], bulk AO filters still suffer from fabrication issues, e.g. expensive, low yield wafer bonding and lapping processes.

Current state-of-the-art integrated AO filters comprise an IDT for SAW generation and an integrated optical waveguide (Figure 1.2.1). Such filter devices are mostly based on a collinear AO interaction resulting in a wavelength-selective polarization conversion [30]. At the beginning the integrated AO filter devices had poor performance, i.e. the RF power requirement for complete conversion was significantly high [33], [34]. This problem was mainly related to the large aperture of the IDT to avoid diffraction of the generated SAW, which meant that only a small percentage of the elastic power overlapped with the optical waveguide [35]. Additional SAW beam spreading could even worsen the overall performance of the device [34].

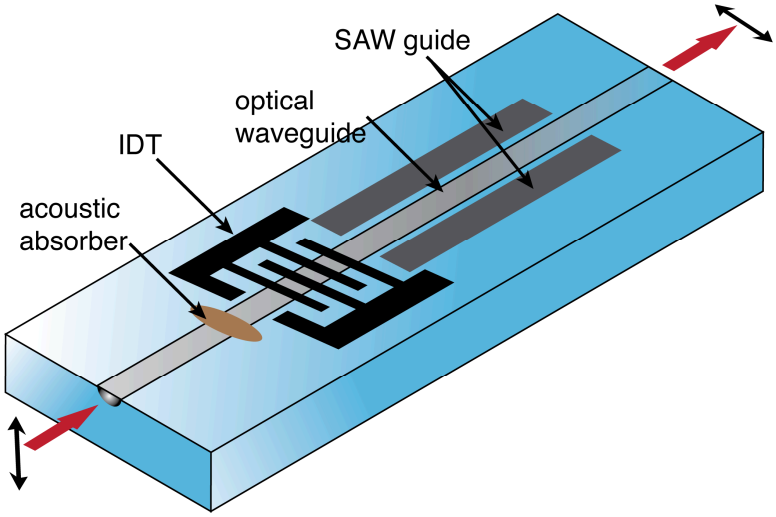

Figure 1.2: Integrated AO filter.

In references [27-29], [36], [37] improved filter configurations have been proposed, making use of an acoustic waveguide to form a

doubly confined structure as a solution to the aforementioned problems (Figure 1.2). The SAW waveguide, e.g. Ti strip [37] or Ti slot [36] waveguide, is laterally guided and confined, yielding large acoustical power density even at low or moderate power levels and also leading to a significant increase in the interaction length.

The purpose of our work is, on the one hand, to make monolithic devices (i.e. the piezo and acousto-optic functions are realized in the same medium) and, on the other hand, achieve waveguide configurations, which can in principle be more efficient. To reach these goals the aforementioned ASL structure is employed where a SAW interacts with an optical guided mode in an electrode-free region. This can lead to significant benefits in terms of optical insertion loss for the devices.

1.3 Objectives

The main objective of this project is to investigate micro-structured optical materials, which can induce, guide and process both acoustic waves, i.e. SAW, and optical waves, which will be used to produce efficient integrated AO devices. The engineering of acoustic properties in optical media on the wavelength scale can open up a new way of AO interactions, with associated exciting basic physics phenomena, that can result in efficient AO devices to be exploited in the optoelectronics industry.

The materials that will be used are ferroelectric crystals, such as lithium niobate ($LiNbO_3$), in which the electrical and mechanical fields are mutually coupled through the piezoelectric effect. $LiNbO_3$

has proven to be of particular interest in both fields of optics and acoustics due to its numerous physical properties as it possesses, e.g., strong piezoelectric, electro-optic and AO coefficients. Therefore $LiNbO_3$ is widely used in integrated optics, also because low loss optical waveguides can be conveniently fabricated through well-established techniques, such as proton exchange (PE), and Ti indifussion (Ti-$LiNbO_3$).

A new approach is proposed for SAW generation that uses the so-called ASL, i.e. a micro- or nano-structured domain engineered ferroelectric crystal, instead of the commonly used uniform bulk piezoelectric substrate with interdigitated (IDT) electrodes. Apart from improving SAW generation in terms of operating frequency, the proposed approach will allow launching SAW using uniform electrodes. Optical waveguides will then be incorporated in the ASL structure with the aim of achieving and integrated AO structure, which will have two important features: (i) they will be monolithic, i.e. the generation of acoustic wave and their interaction with optical waves take place in the same medium; (ii) the region where the optical waveguides are located can be free of any metallic electrode, hence produce low insertion loss.

1.4 Thesis outline

This thesis outline is as follows. After giving an introduction on the background of the project, in **chapter 1** we have described the **state-of-the-art and the novelty** of the thesis by presenting the **objectives** of the work.

In **chapter 2**, we present the basic **theory of SAW and its possible applications to AO filters.** We will start presenting in detail the governing equation as well as the characteristics of SAW in piezoelectric media. We will then present the analysis of **integrated (waveguide) AO filters** with particular focus to the AO interaction in a collinear scheme.

In **chapter 3**, we present the **modeling and design for both ASL acoustic transducers and ASL based AO filters**. We will start deriving analytical models to calculate the modal propagation of the SAW excitation in the ASL transducer. Subsequently, for a correct interpretation of the results, some features of FEM implementation in COMSOL MULTIPHYSICS will be presented. The impulse response model will also be derived for the ASL transducer to analyze the efficiency of SAW generation. Furthermore, we also present FEM simulation to analyze the propagating mode in Ti-$LiNbO_3$ channel waveguide. Finally, these modeling tools will be used to design AO filters.

In **chapter 4**, we describe the **fabrication process of the designed devices** as well as the **characterization techniques and set-ups**. We will start presenting the fabrication processes of the ASL structure and of the coplanar electrodes. After that we will give a brief description of the Ti-$LiNbO_3$ channel waveguide fabrication and RF characterization of the ASL transducers. The scheme of laser interferometry measurement is presented for imaging the SAW displacement. Finally, we present the optical

characterization setup of the AO filter response (loss and conversion efficiency measurements).

In **chapter 5**, we present and discuss **experimental measurements and results** of fabricated ASL transducer and the corresponding AO filter. We will also propose and demonstrate different ways of optimizing the filter's performance, particularly with respect to the filter efficiency in terms of driving RF power.

In **chapter 6**, the results obtained throughout this work are briefly summarized, and we also present the future outlook regarding the improvement of the AO filters as well as other possible applications of the ASL transducer.

Chapter 2 - Basic theory

2.1 Introduction

This chapter describes the basic theory of surface acoustic waves (SAWs) in piezoelectric materials, e.g. in $LiNbO_3$ crystals, as well as the application principles of the SAW in acousto-optical (AO) filters. Along the way, several basic definitions on SAW, AO interaction and also the standardized terms in relation to these fields will be provided. The content of this chapter will be used to understand and compare the underlying principles and assumptions of the modeling tools, which will be developed in the following chapter. The same concept and modeling will be essential to design the devices used in the experiments. Therefore, one could consider this chapter essential to understand the rest of the work contained in this thesis.

2.2 Surface acoustic waves in piezoelectric media

2.2.1 Elastic wave

A solid body deforms when subjected to external forces. If it returns to its original form when the forces are removed, it is said to be elastic. Therefore, elastic waves carry energy from one point to another in a medium without causing permanent deformation of it. Generally, elastic waves can be classified in two very basic forms depending on the direction (polarization) of mass displacement in the medium with respect to the direction of the wave, namely shear waves and longitudinal waves. Shear waves are elastic waves with polarization perpendicular to the propagation direction, whereas

longitudinal waves also known as compression waves, are elastic waves with polarization parallel to the propagation direction. With respect to the surface of the medium, shear waves can be categorized into shear horizontal and shear vertical, respectively. Figure 2.1 illustrates each of the aforementioned waves.

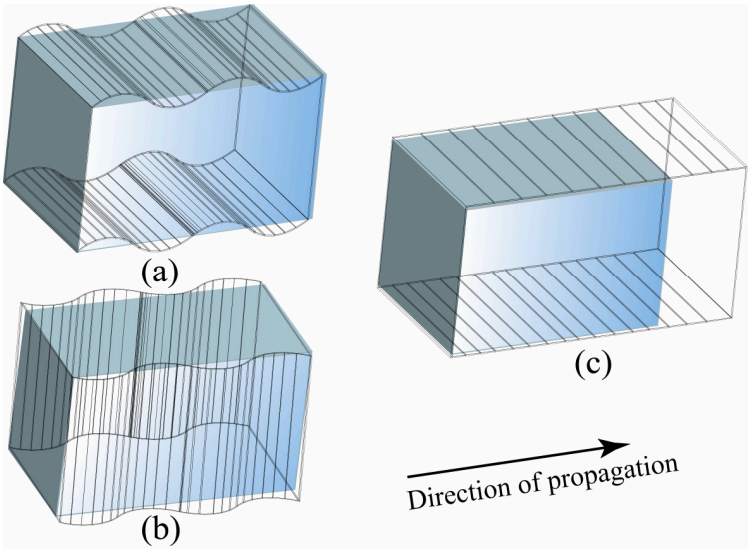

Figure 2.1: (a) Shear vertical wave (b) Shear horizontal vertical wave. (c) Longitudinal wave.

2.2.2 Acoustic wave terminology

In a solid material the elastic wave or acoustic wave involves changes of the relative positions of the particles from the equilibrium state, named displacements u_1, u_2 and u_3 for a given point with coordinates (x_1, x_2, x_3). The displacement is generally a function of position and time. The mechanical state of the acoustic

wave is described by two second-order tensors, the strain *S* and the stress *T*.

The strain is the displacement per unit length, which is related to the internal forces that tend to return the material to its equilibrium, unstrained, state. A displacement or rotation of the solid as a whole causes no strain. The strain at each point is defined by

$$S_{ij}(x_1, x_2, x_3) = \frac{1}{2}\left(\frac{\partial u_i}{\partial x_j} + \frac{\partial u_j}{\partial x_i}\right), \tag{2.1}$$

with $i, j = 1,2,3$. The strain as described in Eq. 2.1 is a dimensionless ratio and is symmetrical. Thus only six of the nine tensor components are independent.

The internal forces that accompany the strain are described by the stress, which may be defined as the force acting on a unit area (N/m^2). Similarly to the strain, the stress tensor is also symmetric, that is $T_{ij} = T_{ji}$.

In piezoelectric materials such as $LiNbO_3$ - the crystal considered in this thesis - the mechanical stress and the strain are coupled to electric field as a result of piezoelectricity:

$$T_{ij} = c_{ijkl}^{E} S_{kl} - e_{kij} E_k \tag{2.2}$$

where c_{ijkl}^{E} denotes the *stiffness* tensor for constant electric field, e_{kij} is the *piezoelectric* tensor, and E_k is the electric field. Similarly for the electromagnetic term, the electric displacement **D** is usually determined by the field E and the permittivity tensor ε_{ij}, but in piezoelectric material it is also related to the strain:

$$D_i = \varepsilon_{ij}^{S} E_j + e_{ijk} S_{jk} \tag{2.3}$$

where ε_{ij}^{S} denotes the permittivity tensor for constant strain.

The stiffness and piezoelectric tensors are of the fourth and third order, respectively. Because of the symmetry of the strain and the stress tensor previously outlined, the stiffness components do not change if *i* and *j* are interchanged, or if *k* and *l* are interchanged, so that

$$c_{ijkl} \equiv c_{jikl} \text{ and } c_{ijlk} \equiv c_{ijkl} \tag{2.4}$$

Therefore the four subscripts notation can be simplified by using the abbreviated subscript notation given in
Table 2.1.

Table 2.1: The abbreviated subscript notation.

I	*ij*
1	11
2	22
3	33
4	23,32

5	13,31
6	12,21

Applying these abbreviations, the constitutive equations, Eqs. 2.1 and 2.2, become:

$$\begin{aligned} T_I &= c_{IJ}^E S_J - e_{kI} E_k \\ D_i &= \varepsilon_{ij}^S E_j + e_{iJ} S_j \end{aligned} \tag{2.5}$$

$LiNbO_3$ is a trigonal crystal, therefore, the stiffness c_{IJ}^E consists of six independent constants:

$$c = \begin{pmatrix} c_{11} & c_{12} & c_{13} & c_{14} & 0 & 0 \\ c_{12} & c_{11} & c_{13} & -c_{14} & 0 & 0 \\ c_{13} & c_{13} & c_{33} & 0 & 0 & 0 \\ c_{14} & -c_{14} & 0 & c_{44} & 0 & 0 \\ 0 & 0 & 0 & 0 & c_{44} & c_{14} \\ 0 & 0 & 0 & 0 & c_{14} & c_{66} \end{pmatrix}, c_{66} = (c_{11} - c_{12})/2 \tag{2.6}$$

four independent components for the piezoelectric constant:

$$e = \begin{pmatrix} 0 & 0 & 0 & 0 & e_{15} & -e_{22} \\ -e_{22} & e_{22} & 0 & e_{15} & 0 & 0 \\ e_{31} & e_{31} & e_{33} & 0 & 0 & 0 \end{pmatrix} \tag{2.7}$$

and two independent components for the dielectric constant:

$$\varepsilon = \begin{pmatrix} \varepsilon_{11} & 0 & 0 \\ 0 & \varepsilon_{11} & 0 \\ 0 & 0 & \varepsilon_{33} \end{pmatrix} \tag{2.8}$$

The measured values of the tensor components for $LiNbO_3$ are taken from [38]. Table 2.2 provides a summary of the relevant material constants and their respective units.

Table 2.2: Summary of material constants for Piezoeletric material.

Constant group	Constant	Definition	Dimension
Elastic	Elastic Stiffness	c_{IJ}	m^{-2} N
Dielectric	Permittivity	ε_{ij}	m^{-1} F
Piezoelectric	Piezoelectric	e_{iK}	V m^{-1}

Since $LiNbO_3$ is anisotropic, the orientation of the internal crystal structure is specified by a set of crystallographic axes usually indicated with uppercase symbols (X, Y, Z). The surface orientation and the wave propagation direction must be defined with respect to the X, Y, Z axes. That is the surface normal x_3, followed by the propagation direction x_1. For example YX-$LiNbO_3$ indicates that x_3 is parallel to the crystal *Y* axis and x_1 is parallel to *Z* axis (Figure 2.2). In other words, YX-$LiNbO_3$ means Y cut and X propagating. The material tensors given in Table 2.2 are specified with respect to X, Y, and Z axes. In general a transformation rotation is necessary to calculate the components in the x_1, x_2, x_3 frame [39].

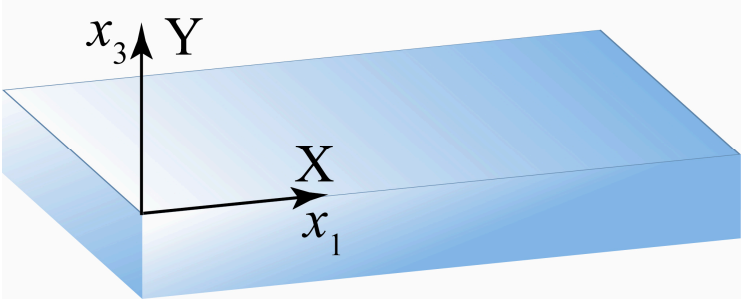

Figure 2.2: YX-$LiNbO_3$ crystal substrate.

2.2.3 Characteristics of surface acoustic waves

For the surface wave analysis, we consider the coordinate system shown in Figure 2.3.

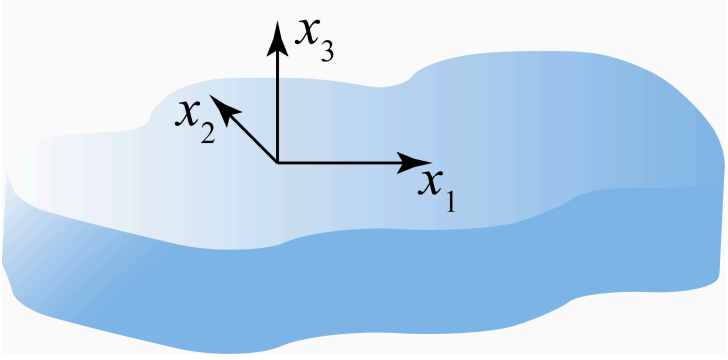

Figure 2.3: The considered coordinate system for surface wave analysis.

The medium is assumed to be infinite in the x_1 and x_2 directions with a boundary at x_3=0 as shown in Figure 2.3. The wave propagation is assumed to be in the x_1 direction, so that wavefronts are parallel to x_2. The (x_1, x_3) plane containing the surface normal vector and propagation direction is known as the *sagittal plane*.

Note that the coordinate system shown in Figure 2.3 will always be the one considered throughout this thesis.

A few approximations must be made regarding the electromagnetic term resulting from piezoelectricity. First, as the velocity of the acoustic waves is 10^4 to 10^5 times smaller than the velocity of the electromagnetic waves, the magnetic field component associated to mechanical vibrations can be neglected. This implies that the electromagnetic field associated with an elastic field is quasi-static, and obeys to a simplified Maxwell's equation:

$$\nabla \times E = -\frac{\partial B}{\partial t} \cong 0 \tag{2.9}$$

Equation 2.9 enables us to express the electric field using a quasi-static approximation given by

$$E = -\nabla \phi \tag{2.10}$$

where ϕ is the electric potential. In addition, as piezoelectric materials are close to perfect insulators, the Maxwell's equation for the displacement D can be written as:

$$\nabla \cdot D = 0 \tag{2.11}$$

Taking into account these assumptions and approximations, the governing equation of motion for the acoustic wave, also called electromechanical wave equation, can be expressed in the following way:

$$\rho \frac{\partial^2 u_i}{\partial t^2} - c_{ijkl} \frac{\partial^2 u_k}{\partial x_j \partial x_l} - e_{kij} \frac{\partial^2 \phi}{\partial x_k \partial x_j} = 0$$
$$e_{ikl} \frac{\partial u_k}{\partial x_i \partial x_l} - \varepsilon_{ik} \frac{\partial^2 \phi}{\partial x_i \partial x_k} = 0 \qquad (2.12)$$

where ρ denotes the mass density of the piezoelectric crystal. Equation 2.12 gives four relations for the four quantities u_i (in meters) and ϕ (in volts). Its unique solution will be determined when the appropriate boundary conditions are given as follows.

For the case of SAW, the mechanical boundary condition that needs to be satisfied is the stress free condition at $x_3 = 0$, that is

$$T_{i3} = c_{i3kl} \frac{\partial u_l}{\partial u_k} + e_{ki3} \frac{\partial \phi}{\partial u_k} = 0 \text{ at } x_3 = 0 \qquad (2.13)$$

For a piezoelectric material it is necessary to take into account an additional electrical boundary condition at the surface. Two cases are usually considered, namely *free-surface* and *metalized*, respectively. The former case applies when the medium above the substrate is vacuum. The latter case corresponds to a substrate covered with a thin metal layer with infinite conductivity. In the case of free-surface, the normal component of **D** is continuous at the interface between the air and the substrate, so that:

$$D_3 = -\varepsilon_0 \frac{\partial \phi}{\partial x_3}, \text{ at } x_3 = 0 \qquad (2.14)$$

In the case of metalized substrate, the potential at the surface is zero:

$$\phi = 0 \text{, at } x_3 = 0 \tag{2.15}$$

The general solution to Eq. 2.12 can be given by a linear combination of plane waves, each of them assuming the following form:

$$\begin{aligned} u_j &= \alpha_j \exp(i\chi x_3)\exp\left[\, j\left(\Omega t - k_{\mathrm{R}} x_1\right)\right], \; j = 1,2,3 \\ \phi_{\mathrm{R}} &= \alpha_4 \exp(i\chi x_3)\exp\left[\, j\left(\Omega t - k_{\mathrm{R}} x_1\right)\right], \text{ for } x_3 \le 0 \end{aligned} \tag{2.16}$$

with coefficient α such that the solution satisfies the boundary conditions as given by Eqs. 2.13 to 2.15, respectively. Here, $\Omega = 2\pi f_{\mathrm{R}}$ is the angular frequency in Hz of the applied electrical signal, while k_{R} is the wave number of the surface wave such that $\lambda_{\mathrm{R}} k_{\mathrm{R}} = 2\pi$. Note we always assume a harmonic solution of the SAW.

The solution, Eq. 2.16, shows that a SAW displacement (u) is always accompanied by an electrical potential ϕ. Both the displacement u and potential ϕ amplitudes decay rapidly over distances from the surface comparable to the wavelength. A decay constant, denoted by χ, has a complex value with negative imaginary part, whose amplitude vanishes when $x_3 \to -\infty$, this being a necessary condition for the existence of surface waves. Figure 2.4 illustrates the characteristic of the SAW propagating on a semi-infinite substrate.

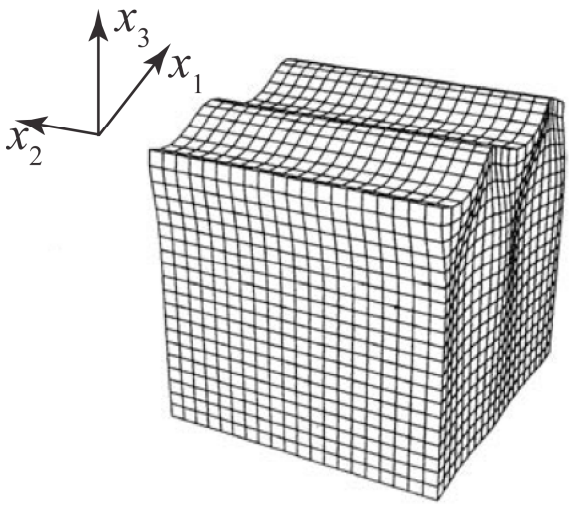

Figure 2.4: The characteristic of the SAW propagating on a semi-infinite substrate [40].

In most cases, the SAW during propagation has an elliptical polarization [41]. This comes from the fact that the SAW displacement is mostly consisting of transvers u_3 and longitudinal component u_1 on the sagittal-plane (x_1, x_3).

2.2.4 SAW power flow

The SAW power flowing on the substrate surface can be determined by the so-called Poynting vector, which is similar to the electromagnetic case, with the following complex form:

$$\overline{P}_j(x_i,t) = \frac{1}{2}\left(-T_{ij}\left(\frac{\partial u_i}{\partial t}\right)^* + \phi\left(\frac{\partial D_j}{\partial t}\right)^* \right) \qquad (2.17)$$

The first and second terms in Eq. 2.17 correspond to mechanical and electrical contributions, respectively, that can be

calculated using the SAW solution presented above. In fact, the measured value actually corresponds to the *time-averaged* of Eq. 2.17, $P = \mathrm{Re}\{\overline{P}\}$. If the SAW propagates along x_1, then the corresponding flowing SAW power can be calculated as: $P_{\mathrm{R}} = 1/2\,\mathrm{Re}\int_A \overline{P}(x_2, x_3)\cdot x_1\, dx_2 dx_3$ where A denotes an arbitrary cross-section of infinite size.

The acoustic power can be directly related to the amplitude of the SAW displacement components u_i. Since the amplitude of u_i depends only on $\tilde{x}_3 \equiv \chi$ as given by Eq. 2.16 and an acoustic beam width w is assumed in the x_2 direction, the acoustic power is given by

$$P_{\mathrm{R}} = \frac{1}{2}\rho\Omega^2 v_{\mathrm{R}} w \int_{-\infty}^{0} |u_i|^2\, dx_3 \tag{2.18}$$

The displacements can be calculated if the acoustic power is known using the following expressions:

$$u_i(x_1, x_3, t) = \left(\frac{2P_A}{\rho\Omega v_{\mathrm{R}}^2}\right) U_i(\tilde{x}_3) e^{j(\Omega t - k_{\mathrm{R}} x_1)} \tag{2.19}$$

where $P_A = P_{\mathrm{R}} / w$ is the power density per unit width of acoustic beam. $U_i(\tilde{x}_3)$ is the u_i component as a function of depth, satisfying the condition:

$$\int_{-\infty}^{0} |U_i(\tilde{x}_3)|^2 d\tilde{x}_3 = 1 \qquad (2.20)$$

2.2.5 Features of SAW excitation in $LiNbO_3$

Two of the most important properties of SAW excitation are velocity, v_R, and a figure of merit, K^2, called the *electromechanical coupling coefficient*.

The SAW propagates parallel to the surface with a SAW velocity v_R. In general, the velocity of the SAW must be less than the velocities of plane waves propagating in the x_1 direction in an infinite material [42]. Of the three plane waves: longitudinal (L), fast shear (FS), and slow shear (SS) mentioned earlier, the slow shear has the lowest velocity, so the SAW velocity must be less than the velocity of the slow shear, which can be written as follows:

$$v_R < v_{SS} < v_{FS} < v_L \qquad (2.21)$$

The velocity of the SAW is constant in all directions in the case of isotropic media whereas it is a function of propagation direction in the anisotropic (i.e. piezoelectric) case. For each direction a set of velocities should always be determined, so that the boundary conditions Eqs. 2.13 to 2.15 are satisfied. Table 2.3 shows the velocities of SAW in different $LiNbO_3$ crystal cuts reported in ref. [43].

Table 2.3: SAW velocities and the electromechanical coupling coefficients in various $LiNbO_3$ crystal cuts.

Crystal cut	SAW propagation direction	Free surface velocity v_f (m/s)	Metallized surface velocity v_m (m/s)	Electomechanical coupling coefficient (%)
X	Y	3748	3681	3.58
X	Z	3483	3396	5.00
Y	X	3769	3740	1.54
Y	Z	3488	3404	4.82
Z	X	3798	3788	0.53
Z	Y	3903	3859	2.25

Note that on a piezoelectric medium, the metalized velocity v_m is always lower than the free surface velocity v_f because a metal film deposited on the surface eliminates the tangential electric field, and thus partially suppresses the piezoelectricity of the material (*electrical loading*) [8]. If the layer thickness is finite, its mechanical effect can become important and changes the SAW velocity (*mass loading*). This change is frequency dependent, thus producing dispersion [8], [44].

We can identify three different cases for the SAW velocity depending on the adjacent medium (ε_d) through the piezoelectric surface permittivity $\bar{\varepsilon}(v)+\varepsilon_d=0$ after imposing the appropriate electrical boundary condition [8]:

1) If the piezoelectric surface is covered by a very thin metallic layer, then a short circuit condition applies: $\phi = 0$ giving $\varepsilon_d = \infty$. Therefore

$$v = v_m \text{ and } \bar{\varepsilon}(v_m) = \infty \tag{2.22}$$

2) If the open circuit condition applies, $\varepsilon_d = 0$, and we have

$$v = v_f \text{ and } \bar{\varepsilon}(v_f) = 0 \tag{2.23}$$

3) If the medium above the surface is vacuum, this gives: $\varepsilon_d = \varepsilon_0$. The SAW velocity ($v_R$) is in between two extreme values, v_m and v_f:

$$v_m < v_R < v_f \text{ and } \bar{\varepsilon}(v_R) = -\varepsilon_0 \tag{2.24}$$

The knowledge of the electromechanical coupling coefficient is of primary importance to design a SAW transducer because it determines the conversion efficiency between electrical and acoustic energy at the surface. This can be expressed as follows:

$$\bar{W}_{ac} = K^2 \bar{W}_e \tag{2.25}$$

where $\bar{W}_{ac}$ and $\bar{W}_e$ represent the acoustic and electrical energy, respectively. If the coefficients of the material are known, K^2 can be calculated directly from $K^2 = e^2 / c\varepsilon$ [41]. In practical cases the constants of the material are usually not precisely known. However the velocity of the SAW propagating under free, v_f, and metallic,

v_m, layers can be easily measured, which allows us to determine the K^2 in the following way.

Let us assume that a continuous voltage V_0 is applied between the two electrodes situated on the free surface. These electrodes will act as a capacitor with a stored energy $\bar{W}_e = 1/2CV_0^2$ where C corresponds to the static capacitance. If the electrodes are short-circuited at $t = 0$, the capacitor returns an electrical energy $\bar{W}_r = 1/2C_0V_0^2$. The difference $\bar{W}_e - \bar{W}_r$ gives the radiated mechanical energy $\bar{W}_{ac} = (C - C_0/C)\bar{W}_e$. Since the ratio $\bar{W}_{ac}/\bar{W}_e$ is nothing else but the electromechanical coupling coefficient as given by Eq.2.25, thus K^2 is then given by $K^2 = 2/(1+\varepsilon_d/\bar{\varepsilon}(\infty))(v_f - v_m)/v_f$ [8]. In the case of $LiNbO_3$, $\bar{\varepsilon}(\infty) >> \varepsilon_d$. Finally we obtain:

$$K^2 \cong 2\frac{v_f - v_m}{v_f} \tag{2.26}$$

Table 2.3 presents the values of electromechanical coupling coefficient for various $LiNbO_3$ crystal cuts.

2.3 Acousto-optic (AO) filters

2.3.1 Principles of AO interaction

In the previous chapter we have mentioned that the SAW and the optical wave can interact via the photoelastic (elasto-optic) effect. Depending on the optical properties of the AO crystals in which the interaction occurs, the interaction can be either isotropic

or anisotropic. In isotropic crystals, the AO interaction is also isotropic and does not change the polarization of the optical beam. Instead the polarization of the optical beam will be converted, i.e. TE (TM)->TM (TE) if the AO interaction takes place in an anisotropic crystal, e.g. $LiNbO_3$. Note that the AO interaction is "unidirectional", it refers to the effect of an acoustic wave on an optical wave since the optical wave will generally have little effect on the acoustic beam. This condition allows us treating the AO interaction as a parametric process, in which the acoustic field (strain) changes the refractive index of the medium according to the following relation [45]:

$$\Delta B_I = \Delta\left(\frac{1}{n^2}\right)_I = p_{IJ} S_J \tag{2.27}$$

where ΔB, the dielectric impermeability tensor variation, is the change of the $\left(1/n^2\right)_I$ component of the optical ellipsoid, p_{IJ} is the fourth-rank photoelastic tensor which for $LiNbO_3$ can be expressed as [45]:

$$p = \begin{bmatrix} p_{11} & p_{12} & p_{13} & p_{14} & 0 & 0 \\ p_{12} & p_{11} & p_{13} & -p_{14} & 0 & 0 \\ p_{31} & p_{31} & p_{33} & 0 & 0 & 0 \\ p_{41} & -p_{41} & 0 & p_{44} & 0 & 0 \\ 0 & 0 & 0 & 0 & p_{44} & p_{41} \\ 0 & 0 & 0 & 0 & p_{14} & p_{66} \end{bmatrix} \tag{2.28}$$

Depending on the direction of the incident optical beam with respect to the SAW, the AO interaction can be categorized into

collinear, when the propagation directions of optical and acoustic waves are parallel, or, non-collinear, when they are not parallel. In the following, we will investigate collinear AO interaction in anisotropic crystals. The corresponding vector diagram is shown in Figure 2.5.

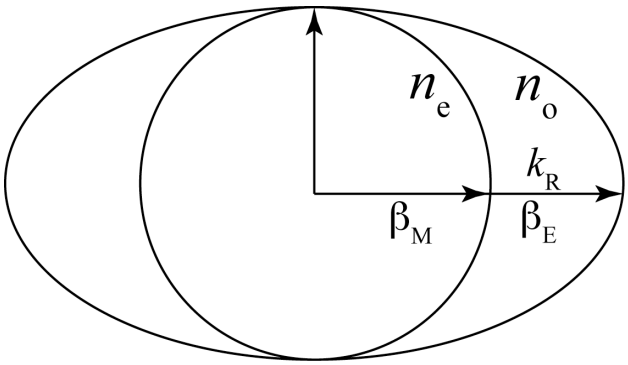

Figure 2.5: Collinear AO interaction in anisotropic crystal.

2.3.2 Characteristics of collinear mode conversion

An anisotropic interaction involves diffraction between ordinary and extraordinary optical beams. Since these beams experience different refractive indices, i.e. $n_o(ordinary)$ and $n_e(extraordinary)$, a consequence of such interaction is that a rotation of the polarization (also called polarization conversion) of the diffracted beam by 90 degrees with respect to the incident beam occurs [45]. In the case of integrated AO filter, the optical beam is guided by an optical waveguide, which is Ti-$LiNbO_3$ in our case. The AO interaction can described by the following wave equations [35]:

$$\nabla^2 E_2(\mathbf{r},t) = \mu_0 \varepsilon_0 \frac{\partial^2}{\partial t^2}\left(\varepsilon_{22} E_2(\mathbf{r},t) + \Delta\varepsilon_{23} E_3(\mathbf{r},t)\right) \qquad (2.29)$$

when the polarization of the incident optical field is TE and

$$\nabla^2 E_3(\mathbf{r},t) = \mu_0 \varepsilon_0 \frac{\partial^2}{\partial t^2}\left(\varepsilon_{33} E_3(\mathbf{r},t) + \Delta\varepsilon_{32} E_2(\mathbf{r},t)\right) \qquad (2.30)$$

when the incident optical field is TM polarized. We are referring to the coordinate system given in Figure 2.5. The perturbation term $\Delta\varepsilon$ in Eqs. 2.29 and 2.30 describes the effect of the SAW on the optical waveguide [35]:

$$\Delta\varepsilon_{23} = \Delta\varepsilon_{32} = -\varepsilon_{22}\varepsilon_{33}\left(\sum_{J=1}^{6} p_{4J} S_J + \sum_{m=1}^{3} r_{4m} E_{R,m}\right) \qquad (2.31)$$

Equation 2.31 shows that the perturbation term is not only through the photoelastic effect, as it was previously explained, There exists an electrooptic contribution, expressed by the product of r and the electric field $E_R = -\nabla\phi_R$. For $LiNbO_3$, the electrooptic tensor r is given by [45]:

$$r_{IJ} = \begin{bmatrix} 0 & -r_{22} & r_{13} \\ 0 & r_{22} & r_{13} \\ 0 & 0 & r_{33} \\ 0 & r_{51} & 0 \\ r_{51} & 0 & 0 \\ -r_{22} & 0 & 0 \end{bmatrix} \qquad (2.32)$$

Let us consider Eq. 2.29 and assume that the waveguide supports only two modes that differ only for their polarization, either TE or TM. The relation between the incident E^{E} (E_2) and the diffracted E^{M} (E_3) optical mode can in this case be expressed by the following coupled-mode equations [46]:

$$\begin{aligned}\frac{dE^{\mathrm{E}}}{dx_1} &= j\frac{\beta_{\mathrm{E}}N_{\mathrm{M}}^2 pS}{4}E^{\mathrm{M}} \\ \frac{dE^{\mathrm{M}}}{dx_1} - j\Delta K E^{\mathrm{M}} &= j\frac{\beta_{\mathrm{M}}N_{\mathrm{M}}^2 pS}{4\beta_{\mathrm{E}}h}E^{\mathrm{E}}\end{aligned} \qquad (2.33)$$

where the magnitude of momentum mismatch relates to the Bragg condition [46]:

$$\Delta K = \frac{\beta_{\mathrm{E}}}{2h}\left\{1 - \frac{N_{\mathrm{M}}^2}{N_{\mathrm{E}}^2} + 2\frac{k_{\mathrm{R}}}{\beta_{\mathrm{E}}} + \left(\frac{k_{\mathrm{R}}}{\beta_{\mathrm{E}}}\right)^2\right\} \text{ with } h = 1 + \frac{k_{\mathrm{R}}}{\beta_{\mathrm{E}}} \qquad (2.34)$$

i.e. $\Delta\mathbf{K} = \beta_{\mathrm{E}} + \mathbf{k_R} - \beta_{\mathrm{M}}$, and $\beta_{\mathrm{E}}, \beta_{\mathrm{M}}$ are the TE and TM propagation constants, respectively, and $N_{\mathrm{E(M)}}$ is the corresponding effective refractive indices. Full mode conversion will be achieved when the phase-matching condition, $\Delta K = 0$, is satisfied:

$$\left|\beta_{\mathrm{E}} + k_{\mathrm{R}}\right| = \left|\beta_{\mathrm{M}}\right| \text{ or in scalar form } \quad \frac{2\pi N_{\mathrm{E}}}{\lambda_0} + \frac{2\pi f_{\mathrm{R}}}{v_{\mathrm{R}}} = \frac{2\pi N_{\mathrm{M}}}{\lambda_0} \qquad (2.35)$$

where λ_0 is the optical wavelength in vacuum. By solving Eq. 2.35 one can determine the center frequency (f_{c}) at phase matching:

$$f_c = \frac{v_R \Delta N}{\lambda_0} \text{ or } \lambda_R = \frac{\lambda_0}{\Delta N} \tag{2.36}$$

where $\Delta N = |N_E - N_M|$. Equation 2.36 expresses the relation at phase-matching between the optical wavelength and the frequency of the SAW. Equation 2.36 is also used to convert the acoustic frequency band into optical bandwidth and vice versa. Within these bands the AO interaction efficiency stays above 50% of its maximum value at perfect phase-matching.

From the coupled-mode equation, Eq. 2.33, we can determine the normalized intensity of the diffracted (converted) optical mode at the exit of the crystal ($x_1 = L$) with respect to the input (incident) value at the entrance of the crystal ($x_1 = 0$) [46]:

$$I_d = 1 - I_i = \left[\frac{s}{2}\right]^2 \frac{\sin^2\left[\sqrt{\left(q^2 + (s/2)^2\right)}\right]}{q^2 + (s/2)^2} \tag{2.37}$$

where I_i denotes, in our case, the intensity of the incident (TE) optical mode. The variables q and s are given by [46]:

$$q = \frac{\Delta K L}{2} \text{ and } \left(\frac{s}{2}\right)^2 = \frac{\pi^2 N_E^3 N_M^3 p^2 |S|^2 L^2}{4\lambda_0^2} \tag{2.38}$$

where L denotes the interaction length. At phase-matching ($q = 0$, $\Delta K = 0$), taking the first order approximation of Eq. 2.37 and assuming very small values of s, it allows us to determine the so-called diffraction or, more specifically, mode conversion efficiency (η) [46]:

$$\eta \approx \frac{\pi}{4}\frac{N_{\mathrm{E}}^3 N_{\mathrm{M}}^3 p^2 \left|S\right|^2 L^2}{\lambda_0^2} \tag{2.39}$$

By substituting Eq. 2.18 into Eq. 2.39, η can be expressed as a function of the acoustic power (P_{R}):

$$\eta \approx \frac{\pi}{2\lambda_0^2} M_2 \left(\frac{P_{\mathrm{R}} L}{w}\right) \tag{2.40}$$

In Eq. 2.40 the quantity

$$M_2 \equiv \frac{N_{\mathrm{E}}^3 N_{\mathrm{M}}^3 p^2}{\rho v_{\mathrm{R}}^3} \tag{2.41}$$

is the *figure of merit* and determines the inherent efficiency of the AO crystal (waveguide) regardless the interaction geometry. From Eq. 2.40 we can also determine the efficiency and the strength of the AO interaction, which is usually expressed by the so-called AO coupling coefficient (κ):

$$\kappa = \frac{\eta}{L} = \frac{\pi}{2\lambda_0} M_2 P_{\mathrm{A}} \tag{2.42}$$

where $P_{\mathrm{A}} = P_{\mathrm{R}} / w$ is the acoustic power density. From Eq. 2.42 one can see that complete polarization conversion occurs when:

$$\kappa L = (l + 1/2)\pi \tag{2.43}$$

where l is an integer number. The mode profiles of the interacting optical mode TE(TM) and of the SAW can be calculated numerically, so that κ can be expressed in the following way [36]:

$$\kappa = \frac{\omega}{8P_0} \iint \left(E^{\mathrm{M}}\right)^{*} \Delta\varepsilon E^{\mathrm{E}}\, dx_2\, dx_3 \qquad (2.44)$$

where P_0 is power of the optical mode.

Equation 2.40 shows that the higher the material refractive index and the lower the acoustic velocity, the higher the AO efficiency. After choosing the appropriate material, one needs to optimize the design, i.e. the interaction geometry. If the acoustic attenuation and geometrical errors in the waveguide design ($\partial\Delta N / \partial x_1$) are negligible, then, according to Eq. 2.40, the optimization of the interaction can be achieved by a correct choice of the length (L) with respect to the width of the acoustic beam (w), i.e. the ratio L/w.

Besides the acoustic efficiency, another crucial parameter is the 3-dB AO bandwidth, which, as it was said above, can be either expressed in terms of acoustic frequency or optical wavelength. The 3-dB or FWHM bandwidth corresponds to the difference between the highest and the lowest acoustic frequencies or optical wavelengths, corresponding to which the normalized diffracted intensity (I_{d}) is reduced by 50%. A rough idea of the filter bandwidth can be gathered using the interference criterion. The nearest point of zero conversion efficiency corresponds to the

following situation: in the first half of the device, the interaction between acoustic and optical waves is in-phase, while in the second half of the device, it is out-of-phase, leading to a complete cancellation of the mode conversion. This corresponds to a total phase mismatch of π, more generally this occurs when the phase mismatch per beat length ($\Delta\delta$) is equal to π / N, where N is the number of beat lengths. This produces a characteristic optical bandwidth ($\Delta\lambda$):

$$\Delta\lambda_{\mathrm{FWHM}} \approx 0.8\frac{\lambda_0^2}{L\Delta N} = 0.8\Delta \tag{2.45}$$

It can be seen from Eq. 2.45 that the filter bandwidth is strongly dependent on both geometry (L) and material (ΔN). Therefore, a narrow AO bandwidth can be achieved by either increasing L or using a highly birefringent medium. As it was pointed out in [46] the birefringence is often not constant over the interaction volume of the crystal ($\delta(\Delta N)$ that is to say: for a fixed acoustic frequency, different regions of the crystal will generate phase matching at slightly different optical wavelengths.. In this case the, one can define a maximum resolution factor (R_{max}) of the AO filter:

$$R_{\mathrm{max}} = \frac{\lambda_0}{\Delta\lambda_{\mathrm{FWHM}}} = \frac{\Delta N}{\delta(\Delta N)} \tag{2.46}$$

Correspondingly, the maximum length of the filter, beyond which there is no increase in resolution, is

$$L_{\max} = \frac{\lambda_0}{\delta \Delta N} \tag{2.47}$$

Note that, this relation strictly applies to a lossless case for both the acoustic and optical waves. However, in most practical cases, the attenuation factor might need to be taken into account along with error due to variation in the birefringence. We will consider all these effects in the following chapters, when we design the AO filters.

Chapter 3 - Modeling and design

3.1 Introduction

The main objective of the modeling is to allow investigation of physical mechanisms and at the same time creating design tools. The design is essential for the development of application specific devices with high efficiency. It is thus crucial the availability of fast and accurate modeling tools for device design. However these two features, speed and accuracy, are difficult to be implemented at the same time. Fast modeling tools usually produce less accurate results, while very accurate tools tend to be slow. In this chapter we will evaluate a broad range of modeling approaches, with the aim of optimizing the device design in terms of calculation speed and accuracy.

As it was pointed out in the previous chapter, investigating AO interactions imply first the study of acoustical and optical propagation in the material. The acoustic and optical propagation if they happen in waveguide geometry can be investigated separately. Each wave propagation is governed by differential equations that must be solved taking into account the boundary conditions associated to the device geometry. In order to obtain the solutions for the situation of interest in our work, we will make use of two different modeling techniques: analytical (*fast*) and numerical (*slow*) method, respectively.

The analytical method, which is based on a scalar approximation, is powerful and offers a quick computation, allowing us to achieve approximate solutions, for example, with respect to the number of excited SAW modes in an ASL transducer along with the corresponding spatial profiles. Since this model includes several approximations, the obtained solutions are not always accurate. In order to increase accuracy for the solutions, numerical methods, such as the finite element method (FEM), can be used. FEM is very time consuming. It is not the scope of this thesis to develop numerical codes. For this reason we will use commercial modeling software COMSOL MULTIPHYSICS for the numerical analysis. In addition to the aforementioned methods, we also consider the so-called impulse response model [8] that enables us to determine the performance of the proposed ASL transducers in terms of the electromechanical coupling coefficient K^2, as it was explained in the previous chapter.

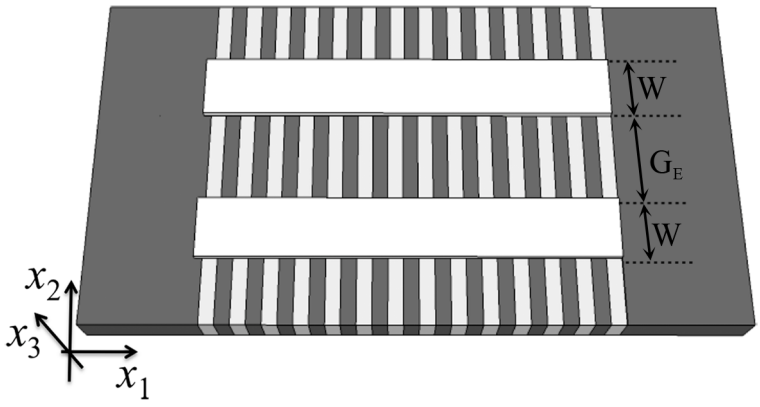

Figure 3.1: A scheme of the proposed ASL transducer with coplanar electrodes.

The ASL transducer, which will be the core of the devices proposed in this thesis, is shown in Figure 3.1. It includes a region of periodically poled (also named "periodically domain inverted") ZX $LiNbO_3$ (PPLN) substrate, on top of which two coplanar electrodes with electrode's width W and gap G_E are placed along the x_1 direction. The period of the ASL structure is denoted by Λ and the lengths of poled (inverted) and unpoled (not inverted) domains of the ASL are a and b, respectively. The poling will change the third rank tensor, i.e. pieozoelectric tensor e, of $LiNbO_3$, whereas the magnitude of the tensor itself will not change. On the contrary, even tensors, such as stiffness c and dielectric tensor ε, remain unchanged through the different oriented domains. So, taking into account the structural conditions of a PPLN based ASL, the modified electromechanical wave equation Eq. 2.12 becomes:

$$\begin{aligned} &\rho \frac{\partial^2 u_i}{\partial t^2} - c_{ijkl} \frac{\partial^2 u_k}{\partial x_j \partial x_l} - \tilde{e}_{kij} \frac{\partial^2 \phi}{\partial x_k \partial x_j} = 0 \\ &\tilde{e}_{ikl} \frac{\partial u_k}{\partial x_i \partial x_l} - \varepsilon_{ik} \frac{\partial^2 \phi}{\partial x_i \partial x_k} = 0 \end{aligned} \tag{3.1}$$

with $\tilde{e}(x_1) \equiv ef(x_1)$ and

$$f(x_1) = \begin{cases} +1 & \text{in positive domain} \quad 0 \le x_1 < a \\ -1 & \text{in negative domain} \quad a \le x_1 < a + b = \Lambda \end{cases} \tag{3.2}$$

We will start deriving analytical models to calculate the modal propagation of the SAW excitation in the ASL transducer. Subsequently, for a correct interpretation of the results, some

features of FEM implementation in COMSOL MULTIPHYSICS will be presented. Also the impulse response model will be derived for the ASL transducer. Finally, we will use these modeling tools to design AO filters.

3.2 Analytical model for modal calculation of the SAW excitation in the ASL transducer

Based on earlier analysis (see Chapter 2), due to the discontinuity of the electric field at the electrode (electrical loading effect) the SAW under a metallic plate (shorted surface case) propagates more slowly than the SAW on a free surface. This condition allows us simplifying the model structure shown in Figure 3.1 as an alternation of "slow" (s) and "fast" (f) regions. The length of the electrode is assumed to be infinite in the x_1 direction, so that each region becomes a semi-infinite ZX-$LiNbO_3$ substrate, where the "slow" and "fast" region refers to the area covered with and without infinitely thin metallic plate, respectively. By solving the electromechanical wave equation (Eq. 2.12) we can determine the SAW velocity $v_{f(s)}$ for each region. Thus the dependence of Eq. 2.12 in x_3 can be dropped, so that a 3D geometry can be simplified into a 2D representation, as it is shown in Figure 3.2.

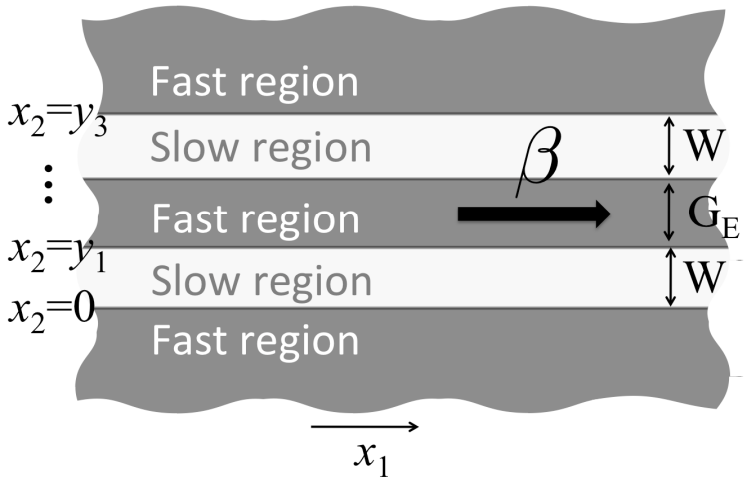

Figure 3.2: Simplified 2D geometry for the proposed ASL transducer

As it was described in Chapter 2, the SAW propagates in an elliptical shape with a major axis perpendicular to the substrate surface, which, in our case, corresponds to the u_3 component. So, if we consider only this component, the SAW propagation in both slow and fast regions can be described by the scalar potential $\psi \equiv u_3$, with ψ satisfying the following wave equation:

$$\frac{\partial^2 \psi_{s(f)}}{\partial x_1^2} + \frac{\partial^2 \psi_{s(f)}}{\partial x_2^2} + \left(\frac{\Omega}{v(x_2)} \right)^2 \psi^2{}_{s(f)} = 0, \qquad (3.2)$$

where $v(x_2)$ corresponds to the distribution of the SAW velocity in x_2, given by

$$v(x_2) = \begin{cases} v_{\mathbf{f}} & x_2 < 0 \\ v_{\mathbf{s}} & 0 < x_2 < y_1 \\ \vdots & \\ v_{\mathbf{f}} & y_3 < x_2 \end{cases} \tag{3.3}$$

In Eq. 3.3, $v_{\mathbf{s(f)}}$ denotes the SAW velocity of the combined material consisting of the substrate covered with (s) and without (f) metallic layer.

Let us suppose that the SAW mode propagates along the x_1-axis with a phase velocity $v_{\mathbf{g}}$, then the corresponding propagation constant will be $\beta = \Omega / v_{\mathbf{g}}$ (we assume a time harmonic behavior of the field with frequency Ω). The general solution of the scalar potential wave equation Eq. 3.2 is given by:

$$\psi(x_1, x_2) = \xi(x_2) e^{-j\beta x_1} \tag{3.4}$$

Since we are interested in confined acoustical modes, the fields must be evanescent in the outermost region (outside the electrodes). Therefore, the solution $W(x_2)$ (Eq. 3.4) satisfying this condition will be given by:

$$\xi(x_2) = \begin{cases} Ce^{\zeta_{\mathrm{f}} x_2} & x_2 < 0, \\ A_1 e^{-i\zeta_{\mathrm{s}}(x_2 - y_1)} + B_1 e^{i\zeta_{\mathrm{s}}(x_2 - y_1)} & 0 < x_2 < y_1, \\ \vdots & \vdots \\ A_3 e^{-i\zeta_{\mathrm{s}}(x_2 - y_1)} + B_3 e^{i\zeta_{\mathrm{s}}(x_2 - y_1)} & y_2 < x_2 < y_3, \\ De^{-\zeta_{\mathrm{f}} x_2} & y_3 < x_2, \end{cases} \tag{3.5}$$

where $\zeta_f \equiv \left(\beta^2 - k_f^2\right)^{1/2}$ and $\zeta_s \equiv \left(k_s^2 - \beta^2\right)^{1/2}$ with $k_f = \Omega / v_f$ on the fast region and $k_s = \Omega / v_s$ on the slow region, respectively. To ensure the waveguiding condition, ζ_f in Eq. 3.5 must be a real and positive value.

In Eq. 3.5, C, A, B, and D are constants that will be calculated through boundary conditions analysis. As the scalar potential and its derivative normal to the discontinuities multiplied by the effective stiffness constant are continuous at the interface between fast and slow regions, we assume that the metallic plate is much thinner compared to the thickness of the $LiNbO_3$ substrate. Therefore, the effective stiffness between two regions can be assumed to be approximately equal and the boundary conditions become:

$$\psi_s = \psi_f \tag{3.6}$$

and

$$\frac{\partial \psi_s}{\partial x_2} = \frac{\partial \psi_f}{\partial x_2} \tag{3.7}$$

Substituting Eqs. 3.6 and 3.7 into Eq. 3.4, we then obtain a linear relation between the field amplitudes on both sides of the layered medium as it is given by the following linear matrix equation:

$$\begin{bmatrix} 0 \\ C \end{bmatrix} = \begin{bmatrix} m_{11} & m_{12} \\ m_{21} & m_{22} \end{bmatrix} \begin{bmatrix} D \\ 0 \end{bmatrix} \tag{3.8}$$

The mode condition corresponds to: $m_{11} \equiv 0$. By applying this condition we can determine the modal constants (β) by searching all the zeros that correspond to the confined modes. Also, we can determine the corresponding mode profile for given mode values.

3.3 Implementation of Finite Element numerical modeling in COMSOL MULTIPHYSICS

3.3.1 Introduction

In the finite element approach, the problem domain is discretized into smaller regions called element, which are connected at specific points called nodes (see Figure 3.3). Depending on the dimension of the domain, the element can be triangular, quadrilateral, and tetrahedral. The solution to the unknown acoustic displacement, potential, electromagnetic fields will be determined at these nodes. The unknown parameters are named as degrees of freedom (DOF). If the domain is infinite, then it will have infinite DOF whereas for the case of finite element the DOF will be finite. As the solutions are given at the nodes, the continuity of the solution will be taken care of by introducing an interpolating function connecting the nodes. The choice for this function determines how the field varies across a single element in the domain. Typically, a polynomial function is chosen as a shape function and the number of the nodes assigned to the element will determine the polynomial order.

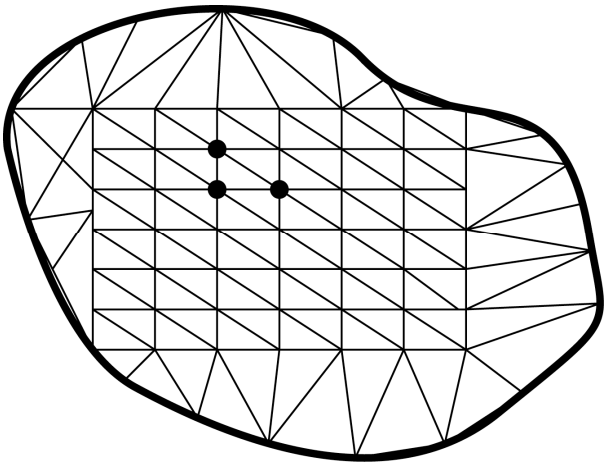

Figure 3.3: A typical domain meshed with triangular element in the FEM simulation. Black dots are the corresponding nodes connecting the elements.

Once the element type is defined, the differential equation solution is approximated by a continuous polynomial function and expressed in terms of unknown values defined at each node. After the whole elements in the domain are considered, it forms a simple system of equations that will be solved. Before solving this equation, the boundary conditions need to be properly addressed in order to obtain a final solution with some degrees of numerical error. Finally, the resulting system of equation will be solved numerically with a technique used in COMSOL MULTIPHYSICS

COMSOL provides modules with built-in differential equations specified for the corresponding physical problem. So, in our case, a COMSOL's structural mechanics module is used for the acoustic problem, while an RF module is for the optics part. For either one

of these modules, the following is the algorithm that is considered for COMSOL simulation:

1. Model definition

In this step, a model structure is designed and defined. The material properties, e.g. Aluminum for the electrodes and $LiNbO_3$ for the substrate, are assigned accordingly, together with the selection of the mesh type. After that the corresponding boundary conditions are applied and then the problem domain is meshed. The mesh size should be tuned according to the required as well as available computer resources. As a rule of thumb, the finer the mesh the more precise the results are. However, as a side effect, the computational memory and time required to solve the problem will increase too. Therefore, a trade off between the accuracy of the result and the computation time has always to be searched.

2. Solving

Two methods will be applied to solve the problems in COMSOL, eigenvalue or eigenfrequency (modal analysis) and harmonic analysis. Modal analysis will give general solutions to the differential equations that are basically the SAW and the optical modes, respectively. For the acoustic problem, in particular, this analysis can be used as a starting point to determine frequencies of interest that will be used as an input values for the harmonic analysis. The particular solutions to the differential equation will be obtained with the harmonic analysis, so that the response of the structure or device, e.g. ASL transducer, in terms of e.g. the

admittance (Y) can be determined. For the optics problem, the modal solution will be considered.

3. Post-processing

In the post-processing, the solution will be visualized in 2-D or 3-D, which allows us validating the simulated results. In addition, COMSOL provides many built-in mathematical functions to determine e.g. the complex admittance (Y) of the transducer device.

3.3.2 Model assumptions

In principle, if the structure considered in the simulation reflects the reality, the obtained solution should be close to the measured data. However, this would require a longer computational time and additional computer resources. Therefore, the problem (model structure) needs to be first simplified in an appropriate manner to achieve a good trade off between computational resources, processing time and accuracy of the results.

3.3.2.1 ASL transducer

3-D modeling

Reduction of model thickness: As it was discussed in the previous chapter, the SAW penetration depth is usually around one wavelength and beyond this value the intensity becomes negligible. We thus assume the SAW depth to be equal to four wavelengths.

Periodic boundary condition: Since the ASL structure is periodic in the propagation direction and the electrode length is always much

larger compared to the lattice period, the computational domain can be reduced to one period cell, thanks to the periodic boundary condition,.

Perfectly-Matched Layer (PML): We consider additional layers that absorb unwanted reflected waves that would degrade the solution.

Once the above approximations are applied, the simplified structure to be solved becomes that of Figure 3.4.

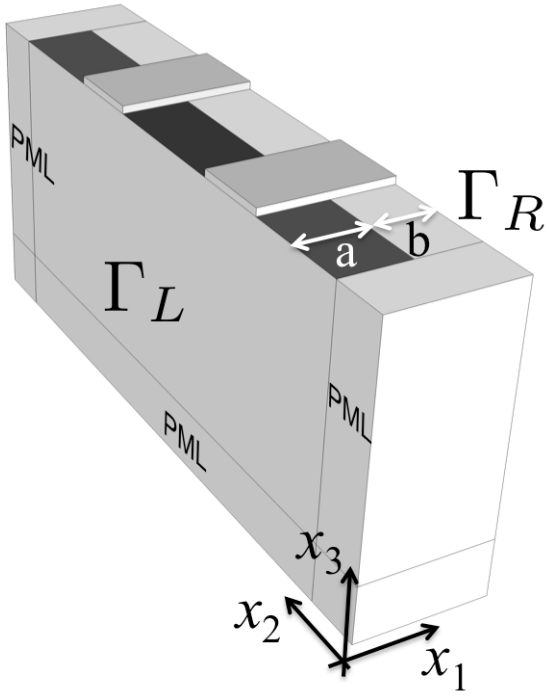

Figure 3.4: A 3D anisotropic and piezoelectric unit cell of the ASL transducer.

In Figure 3.4, Γ_R and Γ_L refer to the imposed periodic boundary condition: $\Gamma_R(x_1 + \Lambda, u, \phi) = e^{i\beta\Lambda}\Gamma_L(x_1, u, \phi)$.

2-D modeling

The above 3-D modeling allows us determining the excited SAW modes in the ASL transducers. Due to the periodic boundary condition, the structure is considered to be infinite along the direction of propagation. This makes difficult the calculations and in addition, even if the problem is made finite, its 3-D modeling using COMSOL would remain cumbersome. We thus simplify it by using a crossed-field approximation [47], as it is common for IDT structures. This approximation allows us reducing the problem from 3-D to 2-D.

As the coplanar electrodes generate the two electric fields components: E_3 and E_2 (Figure 3.5), we can separately treat the contribution of each field component to the acoustic generation. Depending on the field component, two modeling structures configurations are defined as it is shown in Figure 3.6 and Figure 3.7. These will be solved separately.

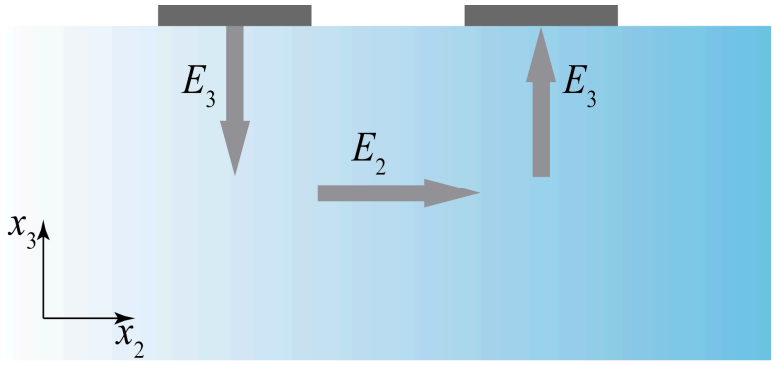

Figure 3.5: A 2-D cross-section of the ASL transducer.

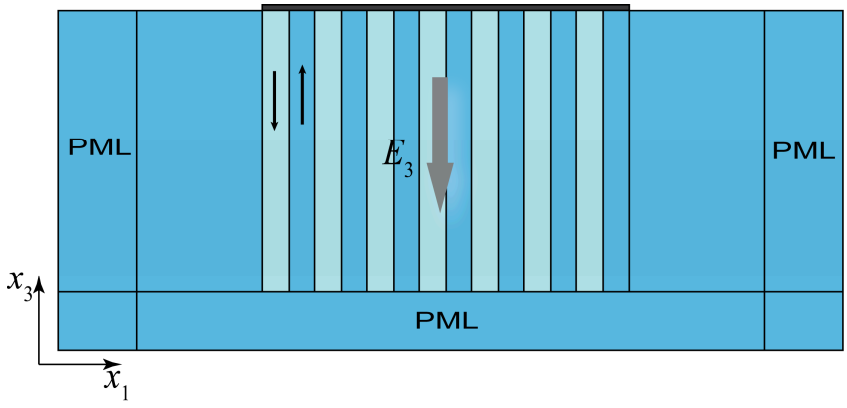

Figure 3.6: 2-D modeling structure of the ASL transducer for the case of E_3 field. Small arrows indicate the poling, while the bigger one indicates the electric field.

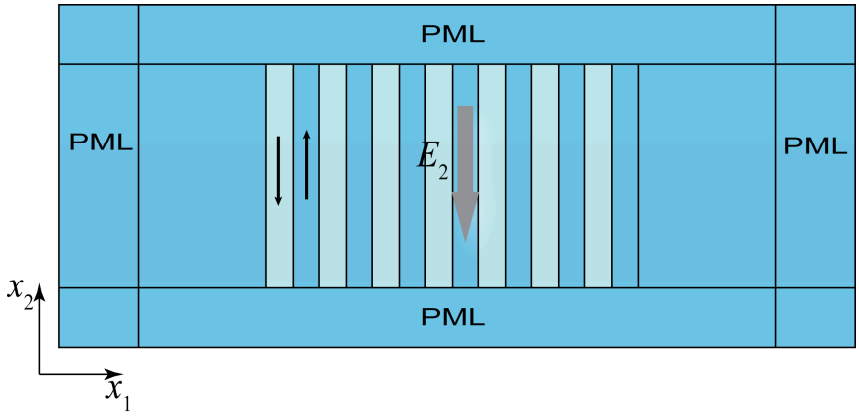

Figure 3.7: 2-D modeling structure of the ASL transducer for the case of E_2 field. Small arrows indicate the poling, while the bigger one indicates the electric field.

For a modeling structure based on E_3 field component, the substrate surface is covered by 200 nm thick Aluminum electrode with a finite length covering the ASL structure (Figure 3.6). The $LiNbO_3$ crystal orientation remains the same, i.e. ZX-$LiNbO_3$. The PML is applied on the right and the left of the structure and also from the bottom of the structure.

The modeling structure based on E_2 field component (Figure 3.7) is essentially similar to the E_3 modeling above, but the material orientation of the substrate is YX-$LiNbO_3$ and the PML is imposed surrounding the structure.

3.3.2.2 Ti-$LiNbO_3$ channel waveguide

The geometry of Ti-$LiNbO_3$ channel optical waveguide is illustrated in Figure 3.8. The guided optical mode is assumed to propagate along x_1 axis. Unlike the above SAW problem, in this

case 2-D (x_2, x_3) plane of the Ti-$LiNbO_3$ waveguide is considered in the simulation to determine the optical modes. We first need to define the refractive index profile of a Ti-$LiNbO_3$ waveguide.

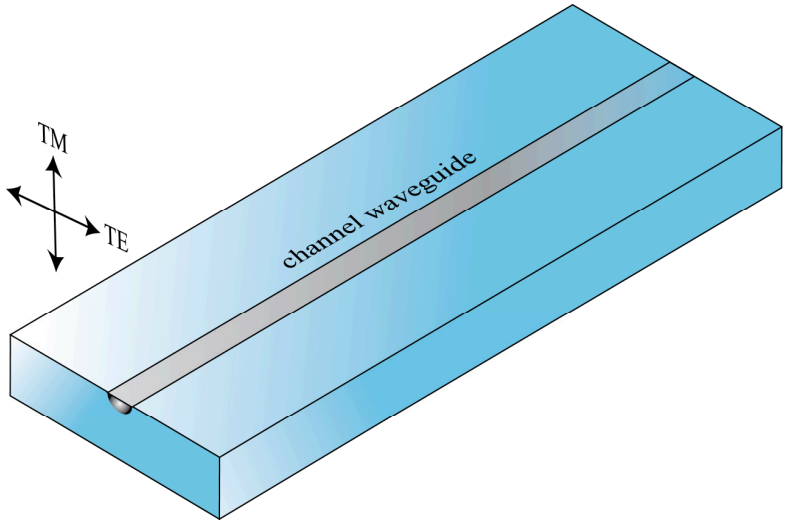

Figure 3.8: Ti-$LiNbO_3$ channel waveguide.

As $LiNbO_3$ is an anisotropic medium, depending on the polarization of the light and on the crystal cut, we have to to consider either an extraordinary or an ordinary index, which can be described as:

$$n_{e(o)}(\lambda_0, x_2, x_3) = n^b_{e(o)}(\lambda_0) + \Delta n_{e(o)}(\lambda_0, x_2, x_3) \qquad (3.9)$$

where λ_0 is the optical wavelength in vacuum and the subscript *e* or *o* denote the extraordinary axis or the ordinary axis, respectively, and the superscript *b* refers to the bulk. The first part of the Eq. 3.9 corresponds to wavelength dependent bulk index and the second term represents the waveguide contribution caused by Ti^{4+}-ions indiffusion.

The Sellmeir dispersion equations define the bulk index for both extraordinary and ordinary waves [48]:

$$n_o^b(\lambda_0) = \sqrt{4.9048 - \frac{0.11768}{0.0475 - \lambda_0^2} - 0.027169\lambda_0^2} \qquad (3.10)$$

and

$$n_e^b(\lambda_0) = \sqrt{4.582 - \frac{0.099169}{0.044432 - \lambda_0^2} - 0.02195\lambda_0^2} \qquad (3.11)$$

The waveguide index contribution is different for ordinary and extraordinary axis. For the extraordinary index a linear dependence on Ti-concentration c(x_2, x_3) is assumed, whereas for the ordinary index change a power-low dependence is considered:

$$\Delta n_{e(o)}(\lambda_0, x_2, x_3) = d_{e(o)}(\lambda_0) h_{e(o)}(x_2, x_3) \qquad (3.12)$$

where $d_e(\lambda_0) = 0.839\lambda_0^2/(\lambda_0^2 - 0.0645)$, $d_o(\lambda_0) = 0.67\lambda_0^2/(\lambda_0^2 - 0.13)$.

In Eq. 3.12, $h_o(x_2, x_3) = [Ec(x_2, x_3)]^\gamma$, and $h_e(x_2, x_3) = Fc(x_2, x_3)$. F and E represent the material constants. On the basis of a diffusion model and anisotropy effects, the Ti^{4+} concentration c(x_2, x_3) in the waveguide is given by $c(x_2, x_3) = c_0 f(x_3) g(x_2)$ where $c_0 = \tau / aD_B$,

$$f(x_3) = \exp(-x_3^2 / D_B^2) \tag{3.13}$$

and

$$g(x_2) = 0.5\{erf\left[(W_{Ti} / 2D_S)(1 + 2x_2 / W_{Ti})\right] + erf\left[(W_{Ti} / 2D_S)(1 - 2x_2 / W_{Ti})\right]\} \tag{3.14}$$

W_{Ti} and τ are the Ti strip width and thickness before diffusion, respectively. D_B and D_S are the bulk and surface diffusion length, respectively, that are given by

$$D_S = 2\sqrt{tD_S^0 \exp(-E_S^0 / kT)} \text{ and } D_B = 2\sqrt{tD_B^0 \exp(-E_B^0 / kT)} \tag{3.15}$$

In Eq. 3.15 t denotes the diffusion time, T is the diffusion temperature during fabrication, k the Boltzman constant, D_B^0 and D_S^0 bulk and surface diffusion constants, and E_B^0 and E_S^0 bulk and surface activation energies, respectively. The relevant constants for z-cut $LiNbO_3$ are in Table 3.1.

Table 3.1: Summary of technology parameters describing Ti indifussion and corresponding refractive index profile in $LiNbO_3$.

	parameter	default value	Dimension
Difussion parameters	D_S^0	3.75e-4 [49]	cm^2/s
	E_S^0	2.22 [49]	eV
	D_B^0	1.4e-2 [49]	cm^2/s
	E_B^0	2.6 [49]	eV
Index-change	F	1.2e-23 [50]	cm^3

fit-parameters	E	1.3e-25 [50]	cm^3
	γ	0.55 [50]	-
Ti properties	A	1.57e-23	cm^3

Once the refractive index of the system is defined, the corresponding magnetic or electric metal boundary condition is imposed.

3.4 Impulse response model

The advantage of this method is that it predicts the absolute amplitude and hence the power of the SAW field excited by the ASL transducers. A complete description of the model for the case of IDT is given in ref. [8]. Here we present an adaptation of the model to ASL transducers.

We assume that the power is constant over x_2, provided that the electrode's width and gap are constant. Let us also suppose that the response to the electrical excitation $a^2(t)$, which also represents the elastic power density of excited SAW, is given by

$$a^2(t) = \int_{-\infty}^{\infty} P_1(x_3,t)dx_3 \tag{3.16}$$

where P_1 is the component of Poynting vector in x_1 direction. In the case that any generated spurious waves are neglected, we obtain

$$\frac{d\bar{W}_s}{dt} = \frac{d\bar{W}}{dt} + \int_{-w/2}^{w/2}\int_{-\infty}^{\infty} P_1(x_3,t)dx_2dx_3 \tag{3.17}$$

where $w \equiv 2W + G_E$ denotes the total length in x_2, $\bar{W}_s$ is the energy from electric sources and $\bar{W}$ is the stored acoustic energy. If we substitute Eq. 3.16 into Eq. 3.17: Eq. 3.17 becomes

$$\frac{d\bar{W}_s}{dt} = \frac{d\bar{W}}{dt} + wa^2(t) \tag{3.18}$$

When the electrodes are short-circuited at t = 0, the response $a(t)$ is given by a sine curve of frequency $f_R = v_R / \lambda_R$ with duration $T = N / f_R$, where N is the number of ASL periods:

$$a(t) = \begin{cases} -a_0 \sin(2\pi f t) & 0 < t < N / f_R \\ 0 & t < 0 \end{cases} \tag{3.19}$$

By integrating Eq. (3.18) and considering $\bar{W}_s = 0$ for t > 0, the generated acoustic energy becomes:

$$\bar{W}_{ac} = \bar{W}(0) - \bar{W}(\infty) = w\int_0^\infty a^2(t)dt = \frac{wa_0^2 N}{2f_R} \tag{3.20}$$

From the definition of the electromechanical coupling coefficient K^2 of the SAW given in Eq. 2.26 , the amplitude of the response is

$$a_0 = K\sqrt{\frac{C_T f_R}{wN}} \tag{3.21}$$

where C_T denotes the capacitance of the coplanar electrodes. Here, we assume that the applied voltage is 1V. The impulse response is the derivate of the step response:

$$h(t) = -\frac{d}{dt}a(t) = a_0 2\pi f \cos(2\pi f t) = K\sqrt{\frac{C_T f_R}{wN}} 2\pi f \cos(2\pi f t) \quad (3.22)$$

In ref. [8], it is known that $G_a(f) = w|H(f)|^2$ where $H(f)$ corresponds to the Fourier transform of the impulse response $h(t)$ and G_a is the radiation conductance of the transducers that expresses the equality of mechanical energy generated by the transducer and dissipated electrical energy. So the radiation conductance is given by

$$G_a(f) = \pi^2 K^2 C_T N f_R \left(\frac{\sin X}{X}\right)^2 = G_0\left(\frac{\sin X}{X}\right)^2 \quad (3.23)$$

where $X = N\pi\frac{f - f_R}{f_R}$.

In Eq. 3.23 $G_0 = \pi^2 K^2 C_T N f_R$ corresponds to the radiation conductance at a resonance frequency $f = f_R$. Thus, the mean value of the SAW power is given by $\langle P \rangle = G_0|U|^2$ where U is the potential being applied to the transducer.

3.5 Structural parameters

In the previous section, the basic simulation tools were discussed. Before we can apply those tools to real problems, we need to introduce the geometrical and material parameters of the device. The material constants, such as stiffness, piezoelectric, and dielectric constants of $LiNbO_3$ are taken from ref. [38], while the rest of the relevant constants, e.g. Al, is taken from ref. [39].

3.5.1 Coplanar electrodes

For the SAW excitation, the electrodes are designed so that the excited electrical field covers almost half of the thickness of the substrate from the surface. This condition is satisfied if the effective width of the electrodes $w_{eff} = W+G_E$ is less then half of the substrate thickness. Since the thickness of the actual $LiNbO_3$ substrate is 500 µm, the lateral width $w_{eff} \leq 250$ µm, e.g. $W = G_E = 100$ µm.

Aluminum is chosen for the metallic electrodes because it is relatively lighter (small mass density ρ = 2700 kg/m^3) compared with other metals, e.g. Gold (ρ = 19300 kg/m^3), so that possible shifts in the resonant frequency due to mass loading effects are strongly reduced. For the same reason, the thickness of the electrodes is chosen as small as possible, 200 nm in our case.

3.5.2 ASL structure

In principle, we design the ASL structure, i.e. period (Λ), such that the desired phase matching wavelength of the AO filter interaction is obtained, which will also depend on the optical

waveguide geometry. Here, we consider an ASL structure with a lattice period Λ = 20 µm. Using the relations $f_R = v_R / \lambda_R$ and $\lambda_R \equiv \Lambda$, the calculated resonant frequency of the SAW is expected to be at around 190 MHz in ZX-$LiNbO_3$. For the 2-D modeling, 11 periods of the ASL is considered in the simulation, which will also define the length of the electrodes.

3.5.3 Ti-LiNbO3 channel waveguide

The Ti-$LiNbO_3$ channel waveguide has to be designed so that it supports a single mode for both TE and TM polarizations at a given optical wavelength (λ_0). In this thesis work the wavelength range of interest goes from 1.4 µm to 1.6 µm. and in that range also the phase matching for the AO filters has to occur. We therefore choose to work with 5 µm, 6 µm, and 7 µm wide optical waveguides. The ordinary and extraordinary index of the bulk $LiNbO_3$ as a function of optical wavelength (λ_0) is shown in Figure 3.9, according to aforementioned Sellmeier dispersion equations (Eqs. 3.10 and 3.11). The extraordinary refractive index profile of 6 µm wide Ti-$LiNbO_3$ waveguide at λ_0 = 1455 nm is shown in Figure 3.10.

To determine the refractive index of Ti-LiNbO3, the following parameters are considered in the simulation: diffusion time t = 7 hours, temperature T = 1333 K, Ti film thickness τ = 110 nm, which are taken from the fabrication parameters.

.

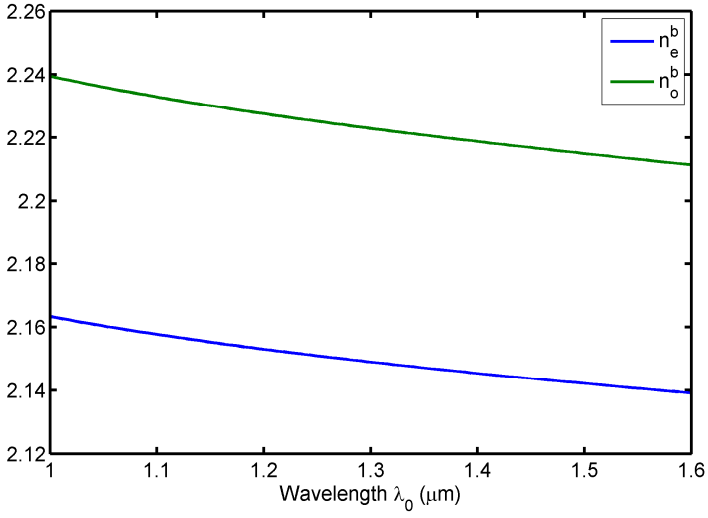

Figure 3.9: Extraordinary and ordinary indices of bulk $LiNbO_3$ as a function of optical wavelength (λ_0).

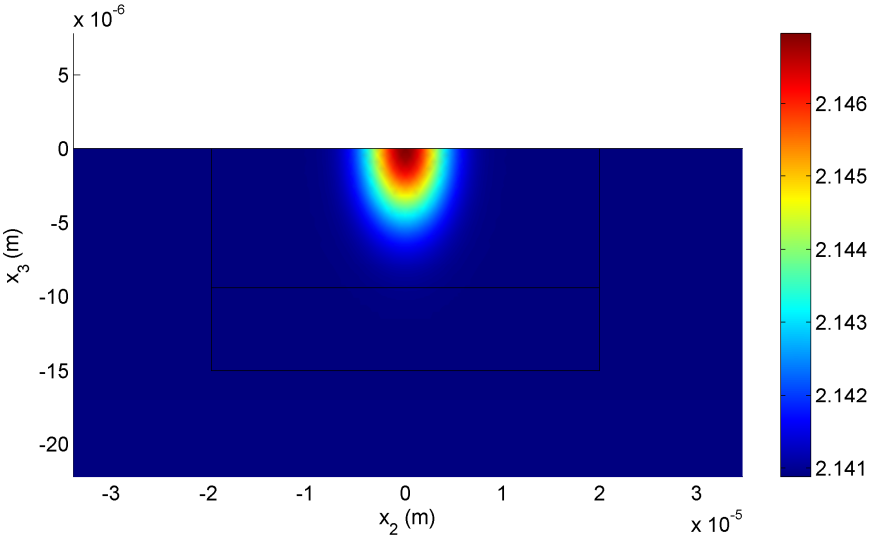

Figure 3.10: The extraordinary mode profile at λ_0 = 1455 nm of a 6 μm wide Ti-$LiNbO_3$ waveguide.

3.6 Computational results

In the previous sections we have chosen the device parameters. In this section we apply the described modeling tools. First, we consider the ASL transducers and then we consider the optical waveguide. Finally, we will discuss the AO filter device.

3.6.1 ASL transducers

3.6.1.1 Modal analysis

The modal velocity of all confined SAW modes excited by the ASL transducer are firstly calculated with the scalar approximation by solving Eq. 3.2. The electrode width W is varied from 30 to 100 µm, while the gap G_E between the electrodes is equal to the width, i.e. $G_E = W$. The FEM simulation in COMSOL is performed with electrode width step-size of 10 µm.

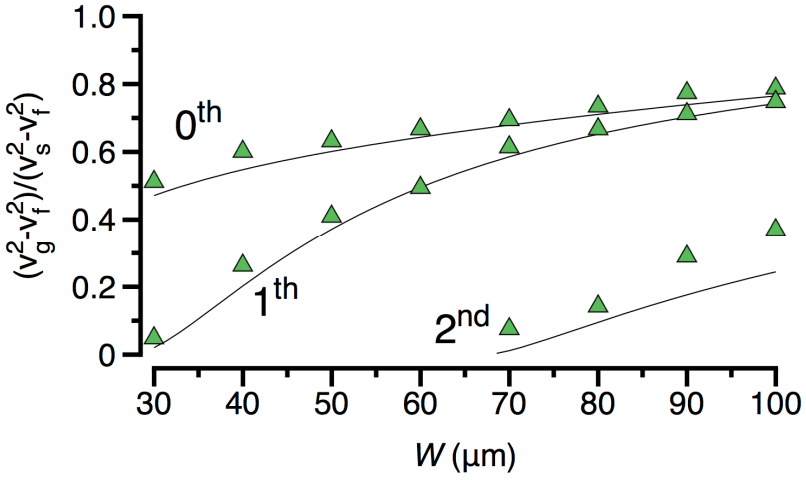

Figure 3.11: Normalized modal velocity as a function of electrode's width (W) of a 20 µm period ASL transducer

calculated with scalar approximation (solid line) and FEM simulation (triangles), respectively.

Figure 3.11 shows the calculated normalized modal SAW velocity as a function of the electrode width (W) using both analytical model and FEM (COMSOL). We see that the number of excited SAW modes obtained by both models is in good agreement, despite the fact that the modes above 80 μm start deviating. Furthermore, from these results one can see that for electrode widths ranging from 30 to about 70 μm, the ASL transducer excites two modes: a symmetrical (0^{th}) and an anti-symmetrical (1^{th}) mode, respectively (Figure 3.12). Above 70 μm electrode width, a higher order mode can also be excited.

The mode profiles of the ASL transducer $G_E = W = 60$ μm calculated by both methods are given in Figure 3.12. From the mode profile, the displacement below the electrodes is larger because the acoustic wave tends to propagate on the slow region (under the metalized surface), this being a similar effect to the SAW waveguiding explained in the previous chapter. Nevertheless it is interesting to note that the symmetrical mode (0th) (Figure 3.12 (a) or (c)) tends to be localized in the central region between the electrodes whereas the anti-symmetrical mode (Figure 3.12 (b) or (d)) is rather located under the electrodes.

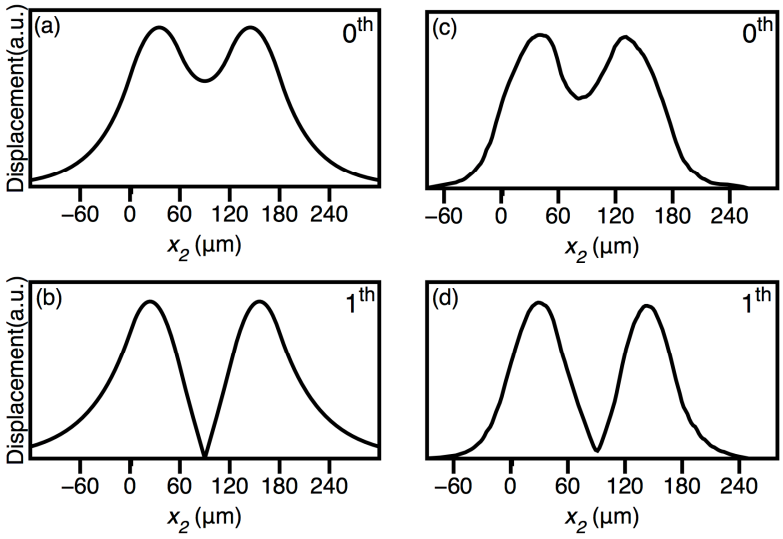

Figure 3.12: Mode profiles of the ASL transducer with W = G_E = 60 μm calculated with scalar approximation ((a) and (b)), and FEM ((c) and (d)), respectively.

3.6.1.2 Harmonic analysis

Once the excited modes in the ASL transducers are known, a harmonic analysis is performed at around identified modal frequencies, determined using the previous analysis. As it was previously explained, the harmonic analysis enables us to investigate the response of the device related to the SAW excitation, i.e. by means of admittance analysis. The complex admittance of the device will be determined using the following relation:

$$Y = \frac{j\Omega Q}{V} \tag{3.24}$$

where, Y denotes the complex admittance, Q represents the charges flowing on the electrodes determined numerically from the

simulation, Ω is the sweeping angular frequency, and V is the driving voltage applied to the structure. The AC driving voltage amplitude V oscillates between ± 1V.

The calculated absolute value of the complex admittance for transducer with $G_E = W = 60$ μm electrodes and the corresponding conductance G_a are shown in Figure 3.13. As the structure is considered to be infinite in the simulation, the two distinct observed peaks correspond to two excited modes as it was also predicted by the previous modal analysis.

A 3-D displacement profile of the fundamental SAW mode at frequency 189.66 MHz is shown in Figure 3.14. From this we can plot the components of the displacement, u_1 and u_3, against the depth coordinates (Figure 3.15). These components quickly drop over a wavelength distance from the surface. In addition u_1 and u_3 are more pronounced than u_2 indicating that the SAW is polarized predominantly on the sagittal-plane, as it is expected. Furthermore, at the surface of the substrate u_1 and u_3 displacements are 90^o out-of-phase with each other (Figure 3.16), which is one of the important properties of Rayleigh SAW.

From the above results, we can say that the SAW excited by the ASL transducer is of Rayleigh type as it is also the case for IDT.

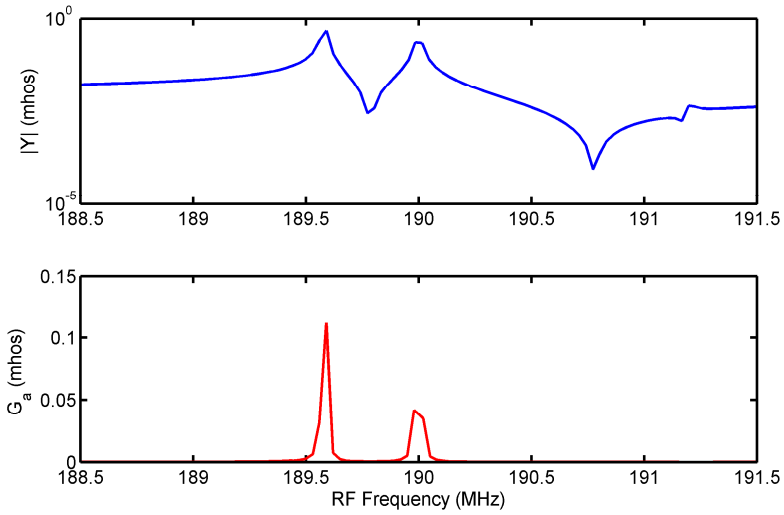

Figure 3.13 The absolute value of complex admittance (|Y|) (*above*) and the conductance (G_a) (*below*) of the ASL transducer with $W = G_E = 60$ μm.

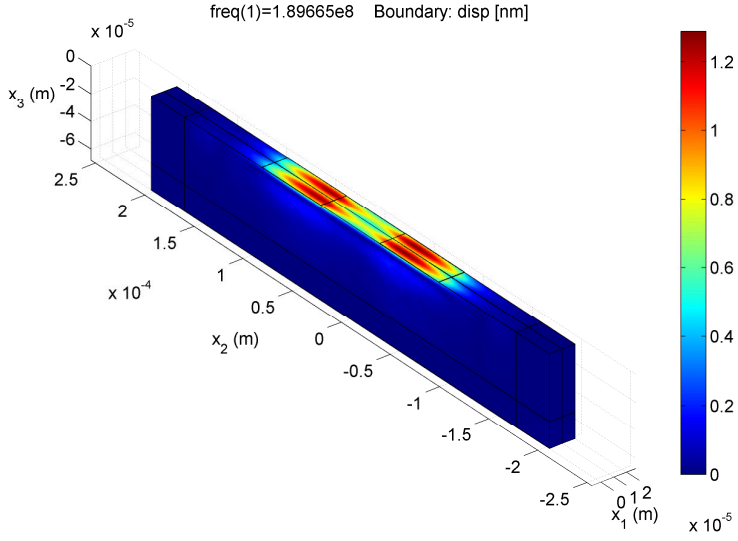

Figure 3.14: The displacement profile of symmetrical mode obtained from ASL transducer in the case of $W = G_E = 60$ μm.

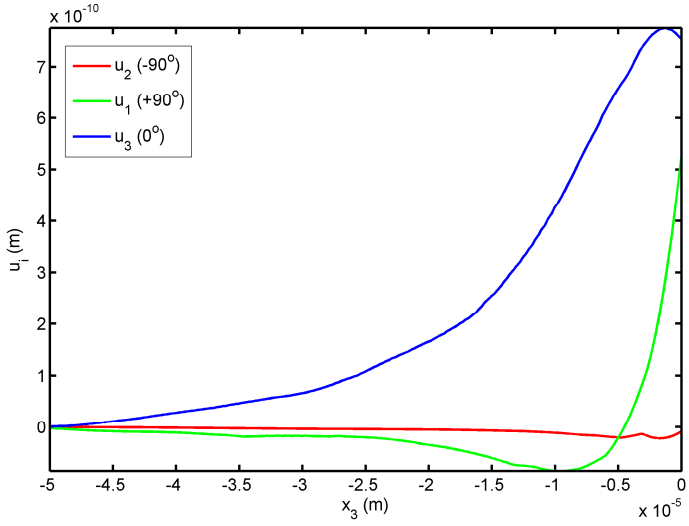

Figure 3.15: The amplitudes of each displacement component are plotted as a function of the depth coordinate. The numbers in brackets in the legend give the phase-shift relative to the u_3 component.

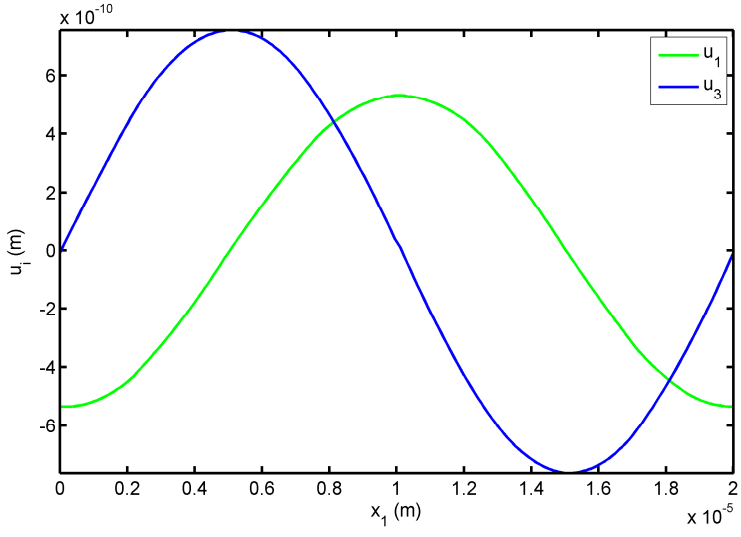

Figure 3.16: Phase difference between displacement components of the SAW generated by the ASL transducer.

3.6.1.3 Propagation analysis

With respect to the SAW propagation in the ASL transducer, the 2-D harmonic analysis is carried out using COMSOL according to the structures outlined in Figure 3.6 and Figure 3.7. In the simulation the input frequency is swept from 150 MHz to 500 MHz to cover all possible excited acoustic waves by the ASL transducer and then the corresponding admittance is calculated for each case.

The calculated absolute values of the admittance (|Y|)) for E_3 and E_2 are shown in Figure 3.17. Two resonant frequencies at around 195 MHz and 350 MHz, respectively, are present. The corresponding displacement profiles at resonance are shown in Figure 3.18 and Figure 3.19, respectively. The resonant frequency at 195 MHz thus corresponds to a SAW excitation propagating at a velocity of 3900 m/s, while the resonant frequency at 350 MHz corresponds to a longitudinal bulk acoustic wave (L-BAW) with a velocity of 7000 m/s.

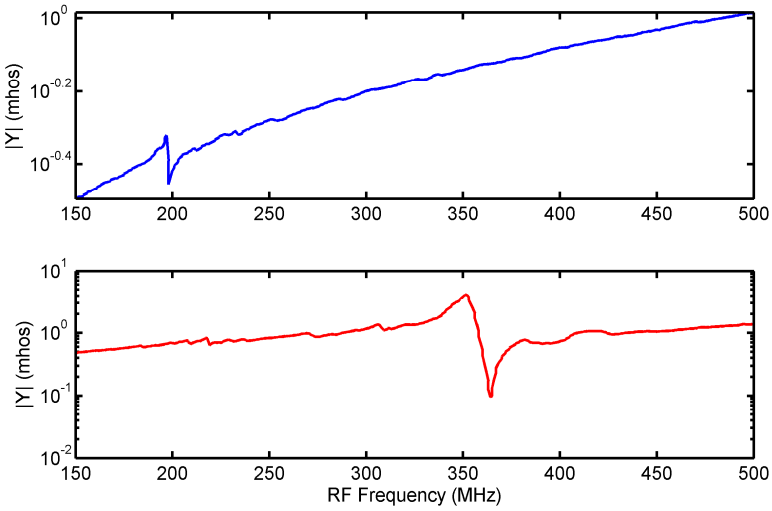

Figure 3.17: The absolute value of the complex admittance (|Y|) as a function of RF frequency obtained when E_3 (*above*) and E_2 (*below*) are considered, respectively, in the modeling.

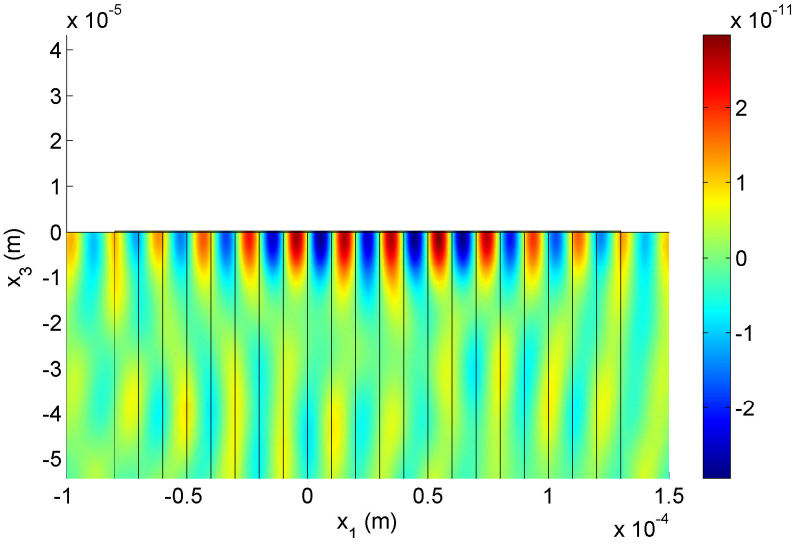

Figure 3.18: The profile of the out of plane component of the displacement (u_3) of the SAW at the resonance frequency of about 195 MHz obtained when E_3 considered.

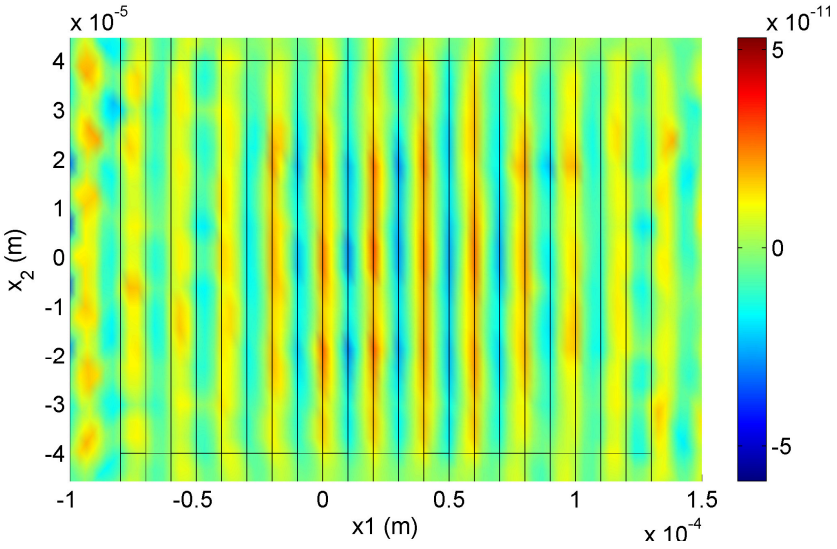

Figure 3.19: The profile of u_1 displacement at the resonance frequency of around 350 MHz corresponding to the bulk acoustic wave generation when E_2 considered.

We can infer from these results that the SAW excitation in ASL transducers is mainly induced by the component E_3 through the coupling of E_3 and e_{31}, whereas the component E_2 induces the excitation of bulk longitudinal acoustic wave via E_2 and e_{22} coupling.

Furthermore, Figure 3.18 shows that the elastic energy of the SAW seems to be localized within the transducer (inside the ASL structure) close to the surface of the substrate, and only very little of its energy outside. To further investigate this phenomenon, we have performed simulation on an IDT structure for comparison. As it is expected, contrary to the ASL case, in the IDT structure, at the

resonant frequency, the SAW propagates away from the transducers (see Figure 3.20).

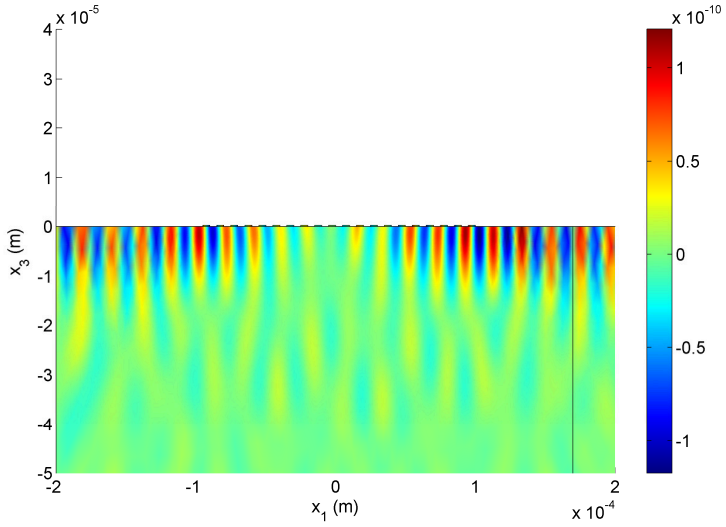

Figure 3.20: The displacement profile of SAW u_3 component at the resonant frequency, excited by the IDT.

From the presented 2-D model, we may infer that the SAW excited by the ASL transducer does not propagate but it is rather confined within the transducer. This will also imply that the length of the ASL transducer will determine the overall filter's length. This effect requires further experimental validations, a subject for the next chapters of this thesis.

3.6.2 Ti-LiNbO3 channel optical waveguide

In order to determine the guided modes in a Ti-LiNbO3 channel waveguide, a 2-D modal analysis is performed using COMSOL. Figure 3.21 shows the distribution of TE and TM modes

as a function of optical vacuum wavelength λ_0 for 5, 6, and 7 μm width optical waveguides, respectively. From these results, one can see that the waveguides support a single mode in both TE (β_E) and TM (β_M) polarization in the wavelength range of interest. The TE and TM mode profiles at λ_c = 1460 nm of a 6 μm width waveguide are shown in Figure 3.22 and Figure 3.23, respectively.

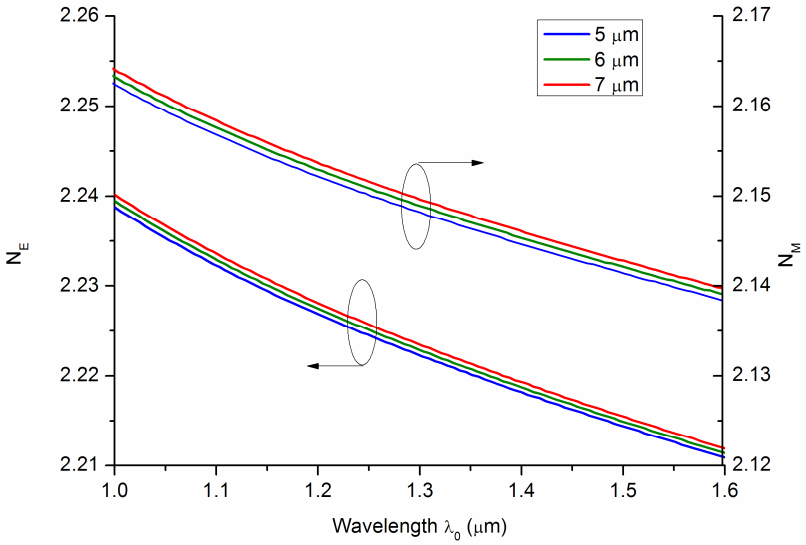

Figure 3.21: TE and TM modes of 5, 6 and 7 μm wide TE-$LiNbO_3$ as a function of optical wavelength λ_0.

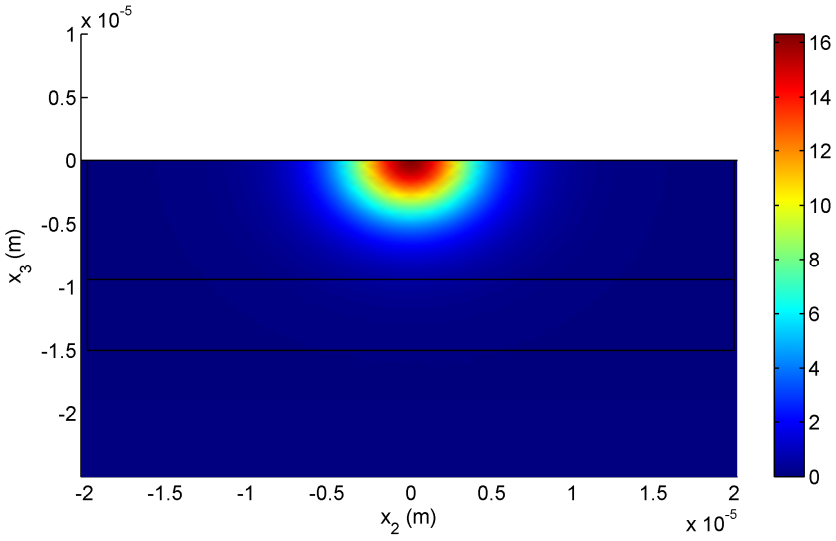

Figure 3.22: Mode profile of TE mode of a 6 µm wide Ti-$LiNbO_3$ at λ_0 = 1460 nm.

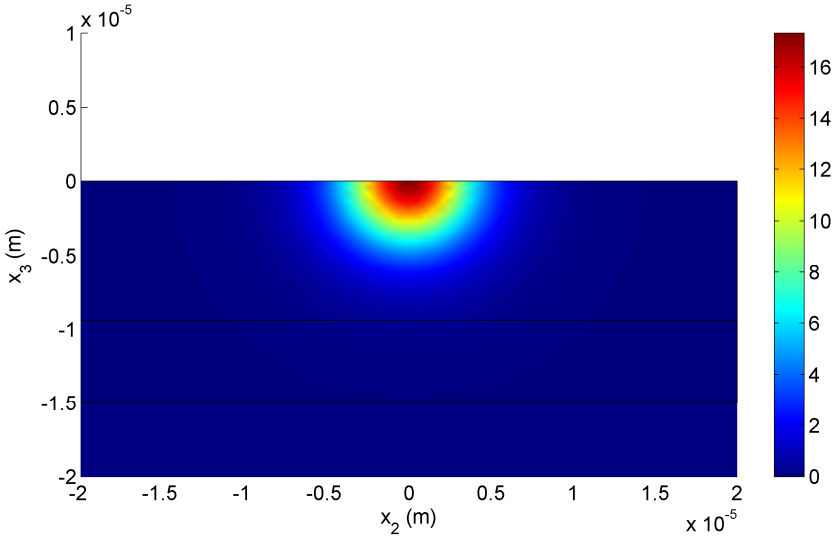

Figure 3.23: Mode profile of TM mode of 6 µm wide Ti-$LiNbO_3$ at λ_0 = 1460 nm.

3.7 Design of AO filters

In order to design an AO filter in accordance with the specified filtering properties, we need to apply the analytical expressions underlying the AO interactions presented in the previous chapter along with the simulation results that have been discussed previously.

We aim at a filter with the following specifications:

- Center wavelength inside the telecommunication windows (C-band, L-band, etc)
- Maximum filter efficiency as large as possible
- FWHM bandwidth as small as possible
- Low "cross-talk"

Initially we will focus the modeling on polarization conversion (TE to TM and vice versa) at a single optical wavelength. The study will then be easily extended to wavelength tunable polarization converters, possibly over a large range without significant reduction in performance with respect to the fixed wavelength case. The modeling and design of AO filters have great similarity to those of grating based- passive filters presented [51].

3.7.1 Center wavelength

From previous chapters we know that full mode conversion will take place when the phase-matching condition $\Delta K = 0$ is satisfied for given optical wavelength λ_0 and SAW frequency f_R. The center wavelength $\lambda_0 = \lambda_c$ is expressed by Eq. (2.36). This

allows us determining the wavelength by making use of the previously calculated optical modes, in which we consider $k_R = 2\pi/\lambda_R$, $\lambda_R = \Lambda$ and $\Lambda = 20$ µm. The calculation results are shown in Figure 3.24. The center wavelength λ_c for three different optical waveguides, 5 µm, 6 µm, and 7 µm wide, is in the 1456 to 1462 nm range, which is suitable for fiber-optic telecommunication.

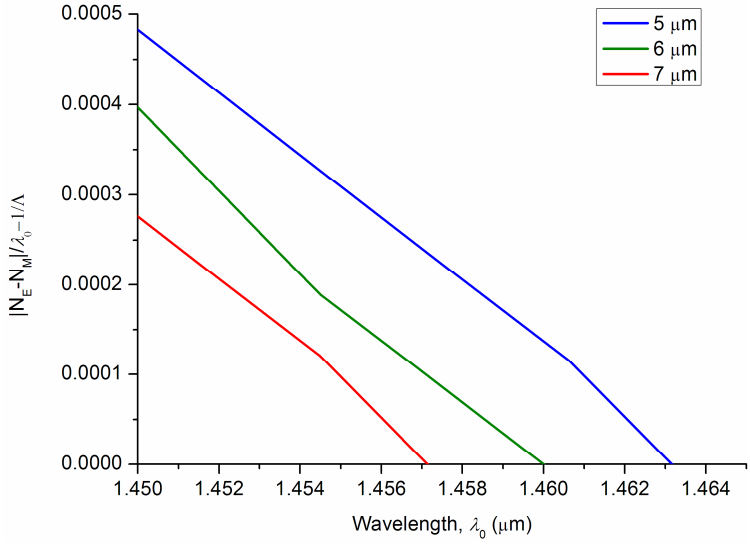

Figure 3.24: Phase-matching condition of the filter consisting of 20 µm period ASL transducer and 5, 6 and 7 µm wide Ti-$LiNbO_3$ waveguide.

3.7.2 Maximum filter efficiency

The proposed AO filter device relying on the TE-TM mode conversion will achieve maximum efficiency at the phase-matching condition, $\Delta K = 0$: $\eta_{max} = \sin^2(\kappa L)$, where the AO coupling coefficient (κ) is given by Eq. 1.42. If we assume that the filter is *lossless*, then the maximum conversion efficiency can reach 100%.

Otherwise (*non lossless* filter), the attenuation, e.g. optical attenuation (α), has to be considered, making the corresponding maximum conversion efficiency:

$$\eta_{\max} = \frac{1}{1-\left(\frac{\Delta\alpha}{2\kappa}\right)^2} \sin^2\left(\kappa L\sqrt{1-\left(\frac{\Delta\alpha}{2\kappa}\right)^2}\right) \exp(2\bar{\alpha}L) \qquad (3.25)$$

where $\Delta\alpha = \alpha_2 - \alpha_1$ denotes the difference between two modal attenuation coefficients, and $\bar{\alpha} = (\alpha_1 + \alpha_2)/2$ is the average modal attenuation coefficient. Here, we define α such that negative value corresponds to the attenuation. For practical cases, $(\Delta\alpha/2\kappa)^2 << 1$, the optimum length becomes:

$$L_{\text{opt}} = \frac{1}{\kappa}\arctan\left(\frac{-\kappa}{\bar{\alpha}}\right) \qquad (3.26)$$

and correspondingly the maximum efficiency:

$$\eta_{\max} = \sin^2\left[\arctan\left(-\frac{\kappa}{\bar{\alpha}}\right)\right] \exp\left[2\frac{\bar{\alpha}}{\kappa}\arctan\left(-\frac{\kappa}{\bar{\alpha}}\right)\right] \qquad (3.27)$$

According to Eq. 3.27, it is a function of the average attenuation $-\bar{\alpha}$ relative to coupling coefficient κ only. Figure 3.25 shows the maximum efficiency as a function of $-\bar{\alpha}/\kappa$. It is important to have large coupling coefficient κ relative to the average attenuation factor $\bar{\alpha}$ if one wants to obtain high efficiency. In practice, a filter efficiency above 90% can be achieved, if the ratio $-\bar{\alpha}/\kappa$ is smaller than 0.033. Hence, the AO coupling κ must be at least 30

times larger than $|\overline{\alpha}|$. In addition, the highest maximum efficiency can be obtained with a filter length according to Eq. 3.26. In the following of this chapter we will assume the filter *lossless* for simplicity. This allows us understanding more straightforwardly the underlying mechanisms. For more precise calculations the loss should always be included

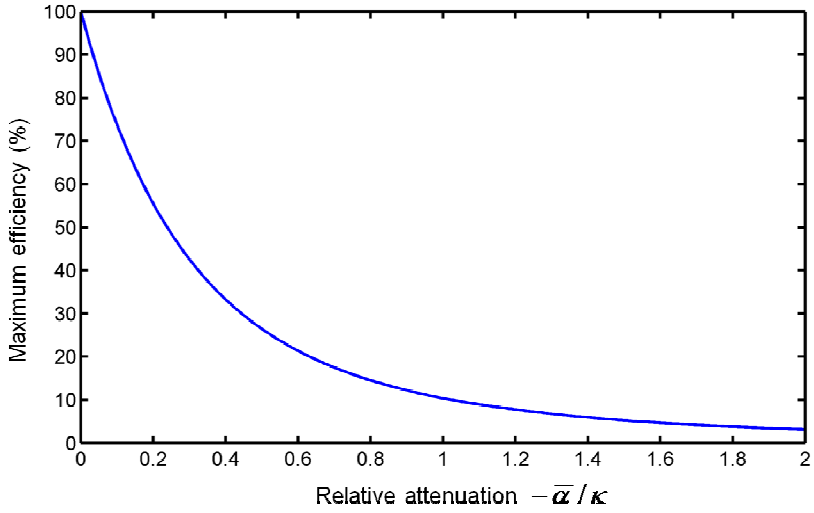

Figure 3.25: Maximum diffraction efficiency as a function of relative attenuation $-\overline{\alpha}/\kappa$.

3.7.3 FWHM bandwidth

The FWHM bandwidth, also called 3-dB bandwidth, of the filter device is given by Eq. (2.45). In the following we further discuss possible ways for optimizing the FWHM bandwidth. In order to design a device with optimum FHWM, we first investigate the relation between a wavelength shift and the deviation from phase-matching.

At the center wavelength λ_c, by definition, the deviation from phase-matching is zero ($\Delta K(\lambda_c) = 0$). In the case of small deviation, we can apply the Taylor expansion of $\Delta K(\lambda_c)$ around λ_c in order to determine the wavelength shift $\Delta\lambda_{\mathrm{HM}}$ as a function of ΔK_{HM} that denotes the phase-matching deviation corresponding to 50% of the maximum conversion:

$$\Delta K_{\mathrm{HM}} = \Delta K(\lambda_c + \Delta\lambda_{\mathrm{HM}}) \approx \Delta\lambda_{\mathrm{HM}} \left(\frac{\partial \Delta K}{\partial \lambda_0} \right)_{\lambda_0 = \lambda_c} \tag{3.28}$$

The FWHM bandwidth $\Delta\lambda_{\mathrm{FWHM}}$ equals twice the wavelength shift $\Delta\lambda_{\mathrm{HM}}$:

$$\Delta\lambda_{\mathrm{FWHM}} = 2\Delta K_{\mathrm{HM}} \left[\left(\frac{\partial \Delta K}{\partial \lambda_0} \right)_{\lambda_0 = \lambda_c} \right]^{-1} \tag{3.29}$$

In the case of a *lossless* filter, the derivative of ΔK with respect to wavelength:

$$\left(\frac{\partial \Delta K}{\partial \lambda_0} \right)_{\lambda_0 = \lambda_c} = \frac{2\pi}{\lambda_c} \left[\left(\frac{\partial (N_M - N_E)}{\partial \lambda_0} \right)_{\lambda_0 = \lambda_c} - \frac{(N_M - N_E)}{\lambda_c} \right] \tag{3.30}$$

$(N_M - N_E)/\lambda_c = 1/\Lambda$. By inserting this into Eq. 3.30 and then Eq. 3.30 into Eq. 3.29, we obtain:

$$\Delta\lambda_{\mathrm{FWHM}} = \frac{\lambda_c \Lambda \Delta K_{\mathrm{HM}}}{\pi} \left[\Lambda \left(\frac{\partial (N_M - N_E}{\partial \lambda_0} \right)_{\lambda_0 = \lambda_c} - 1 \right]^{-1} \tag{3.31}$$

The next step is to find ΔK_{HM} such that the efficiency of the filter is half its maximum by using Eq. (2.37):

$$\frac{(\kappa L)^2 \sin^2(sL)}{(sL)^2} = \frac{1}{2}\eta_{max} = \frac{1}{2}\sin^2(\kappa L) \tag{3.32}$$

where $(sL)^2 = (\kappa L)^2 + (\Delta K_{HM} L/2)^2$. $\Delta K_{HM} L$ weakly depends on κL. We can then define a function $f(\kappa L)$ as FWHM factor, that is basically expressed by $f \equiv \Delta K_{HM} L$. Inserting $f(\kappa L)$ into Eq. 3.31, the FWHM becomes:

$$\Delta\lambda_{FWHM} = \frac{\lambda_c \Lambda f(\kappa L)}{L\pi}\left[\Lambda\left(\frac{\partial(N_M - N_E)}{\partial\lambda_0}\right)_{\lambda_0=\lambda_c} - 1\right]^{-1} \tag{3.33}$$

Solving Eq. (3.32) numerically allows to determine $f(\kappa L)$ as given in Figure 3.26.

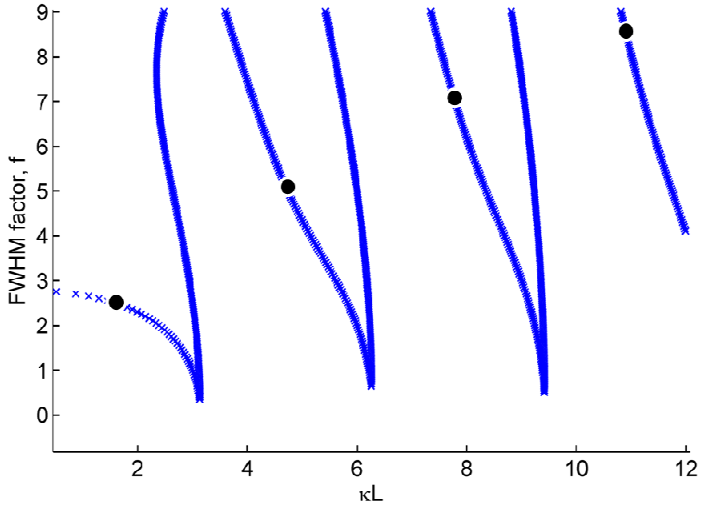

Figure 3.26: The FWHM factor *f* as a function of κL. Black dots corresponds to value of $\kappa L = \pi/2, 3\pi/2, ..., 5\pi/2$.

In practice, κL is chosen so that $\kappa L = (l + 1/2)\pi$ to achieve optimum conversion efficiency. The values are marked with circles in Figure 3.26. From Figure 3.26 one can see that the best choice is to take $\kappa L = \pi/2$ in order to have both efficiency and FWHM bandwidth of the filter optimized. The corresponding value of the FWHM factor is $f(\pi/2) \approx 2.506$ while the FWHM becomes:

$$\Delta\lambda_{FWHM} \approx 0.8\frac{\lambda_c \Lambda}{L}\left[1 - \Lambda\left(\frac{\partial(N_M - N_E}{\partial\lambda_0}\right)_{\lambda_0=\lambda_c}\right]^{-1} \qquad (3.34)$$

It is clear from Eq. 3.34 that for minimum bandwidth operation, one needs to achieve $\kappa L = \pi/2$ and, at the same time, the length of the device should be large enough for increased efficiency. However, in the real case, it should not be too large to avoid

possible degradations due to attenuation, as it had been previously discussed.

Figure 3.27 shows the FWHM of the filter as a function of device length with 6 μm wide optical waveguide. For a 10 mm long filter the expected FWHM bandwidth is about 2.33 nm.

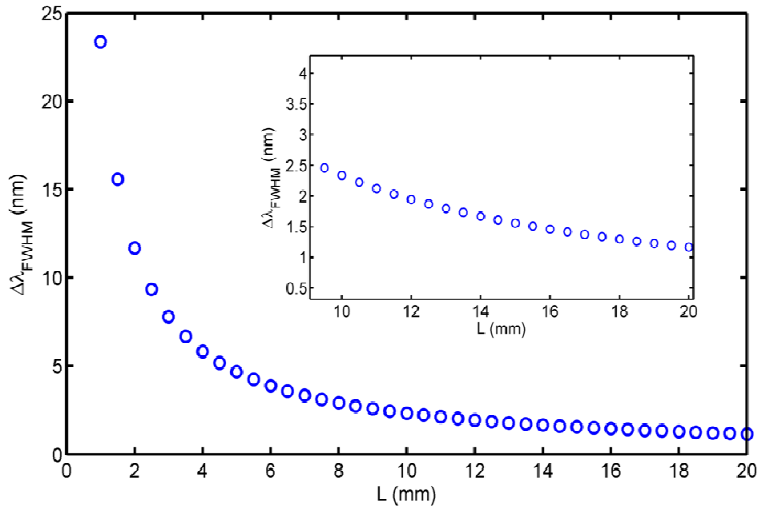

Figure 3.27: FWHM as a function of AO filter length consisting of 20 μm period ASL transducer and 6 nm wide Ti-$LiNbO_3$.

3.7.4 Cross-talk

To be able to apply the AO filter in WDM systems, the filter needs to be designed in such way that one channel can be selected while the signals of the other channels are sufficiently suppressed. Therefore, the filter has to have sufficiently large bandwidth to allocate the signal corresponding to the selected channel and at the same time narrow enough to ensure that the side channels do not

fall within the passband range. In practice it is convenient to introduce the so-called *-20 dB distance* of a filter, which is the distance from center wavelength corresponding to which the side mode suppression is -20 dB (1%). If the distance from one channel to the next is at least equal to the -20 dB distance then the cross-talk between two neighboring channels can be considered acceptable.

In the design we aim at a filter having a -20 dB distance as small as possible in order to make it possible to place more channels in a given wavelength range, hence increasing the transmitted bandwidth. The maxima of the side lobes are approximately located at wavelengths corresponding to the condition: $\sin^2(sL)=1$, where $(sL)^2=(\kappa L)^2+(\Delta KL/2)^2$ and κL is given by Eq. (2.43) for optimum conversion. From this we obtain the envelope $E(\Delta K)$ given by

$$E(\Delta K)=\frac{\kappa^2}{\kappa^2+(\Delta K/2)^2} \tag{3.35}$$

Considering lossless filters (100% maximum conversion), ΔK can be found by setting the envelope $E(\Delta K)$ to 0.01, thus producing $\Delta K_{-20\mathrm{dB}}\approx 20\kappa$. Using the same procedure for FWHM bandwidth, the -20 dB distance denoted by $\Delta\lambda_{-20\mathrm{dB}}$ is given by

$$\Delta\lambda_{\text{-20dB}}=20\kappa\frac{\lambda_c\Lambda}{2\pi}\left[\Lambda\left(\frac{\partial(N_M-N_E}{\partial\lambda_0}\right)_{\lambda_0=\lambda_c}-1\right]^{-1} \tag{3.36}$$

Eq. 3.36 implies that to minimize $\Delta\lambda_{-20\text{dB}}$ the coupling coefficient κ should be as small as possible. By comparing this to FWHM bandwidth given by Eq. (3.34), we find that

$$\Delta\lambda_{-20\text{dB}} \approx 6.28\Delta\lambda_{\text{FWHM}} \tag{3.37}$$

for the case of $\kappa L = \pi/2$.

3.7.5 Relative tuning range

If the case of filter tunable filters, it is desirable to achieve a tuning range that is as large as possible, relative to the FWHM bandwidth of the filter itself. The tuning relation is given by Eq. (2.36) showing that the tuning can be achieved either by varying the difference between the effective indices of the modes $\Delta N = |N_E - N_M|$ or by varying the frequency of the SAW (i.e. the SAW wavelength $\lambda_R(\Lambda)$).

To vary the SAW wavelength one could use chirped ASL, i.e. periodic structures with varying period Λ. This concept has been extensively described in ref. [22] in which the bulk AO tunable filter is demonstrated using a linearly chirped ASL. By inserting the calculated guided modes into Eq. (2.36) allows us determining the frequency tuning as it is reported in Figure 3.28.

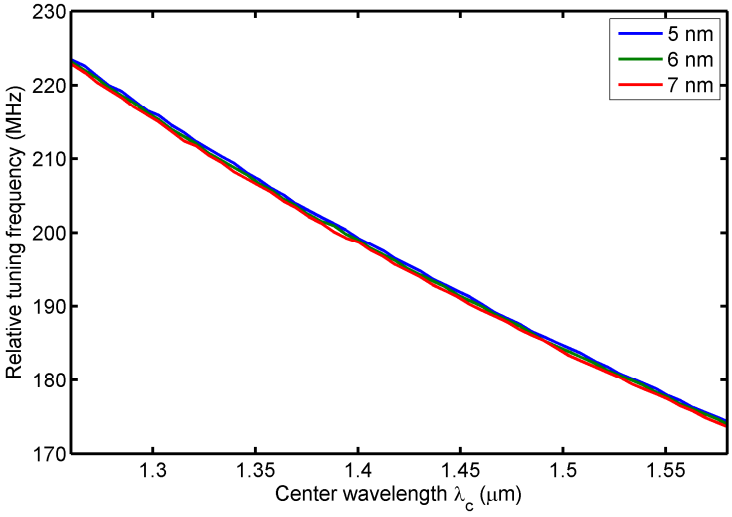

Figure 3.28: Relative frequency tuning as a function of center wavelength λ_c.

If the filter is tuned by varying ΔN, then the tuning range can be calculated using the phase-matching condition $\Delta K = 2\pi/\lambda\Delta N - k_R = 0$. At the center wavelength of the filter and at phase-matching, we have $2\pi/\lambda_0\Delta N_c - k_R = 0$ where ΔN_c denotes $|N_E - N_M|$ at the center wavelength. Due to the tuning mechanism, ΔN_c changes to

$$\Delta N_c^* \equiv \Delta N_c + \delta(\Delta N_c) \tag{3.38}$$

Thus, the phase-matching condition is no longer satisfied at the original center wavelength. In order to find out the new center wavelength λ_d at which the phase-matching condition is satisfied, we have also to consider that ΔN_d at the new wavelength λ_d is different from ΔN_c, due to dispersion:

$$\Delta N_d \approx \Delta N_c^* + \left(\frac{\partial \left(\Delta N_c^* \right)}{\partial \lambda} \right)_{\lambda = \lambda_c} \left(\lambda_d - \lambda_c \right) \tag{3.39}$$

Inserting Eq. 3.39 into Eq. 3.38 and assuming $\delta(\Delta N_c)$ to be dispersion-less, ΔN_d becomes:

$$\Delta N_d \approx \Delta N_c + \delta(\Delta N_c) + \left(\frac{\partial (\Delta N_c)}{\partial \lambda} \right)_{\lambda = \lambda_c} (\lambda_d - \lambda_c) \tag{3.40}$$

We know that at phase-matching $\Delta N_{\mathrm{d}} = \lambda_{\mathrm{d}} / \Lambda$ and $\Delta N_c = \lambda_c / \Lambda$ for the cases with and without detuning, respectively. By inserting these relations into Eq. 3.40 and denoting the tuning range as $\Delta \lambda_{\mathrm{T}} \equiv \lambda_{\mathrm{d}} - \lambda_{\mathrm{c}}$, we obtain:

$$\Delta \lambda_{\mathrm{T}} \approx \Lambda \delta \left(\left| N_E - N_M \right| \right) \left(1 - \Lambda \left(\frac{\partial \left(\left| N_E - N_M \right| \right)}{\partial \lambda} \right)_{\lambda_0 = \lambda_{\mathrm{c}}} \right)^{-1} \tag{3.41}$$

According to Eq. 3.41, the tuning range mainly depends on the birefringence change $\delta\left(\left| N_E - N_M \right| \right)$:

$$\frac{\Delta \lambda_{\mathrm{T}}}{\Delta \lambda_{\mathrm{FWHM}}} \approx 1.3 \frac{\delta \left(\left| N_E - N_M \right| \right) L}{\lambda_{\mathrm{c}}} \tag{3.42}$$

at $\kappa L = \pi / 2$.

3.8 Fabrication tolerances

In practical cases the performance of an AO filter are limited by fabrication tolerances, i.e. intrinsic errors of the technological

processes used for the device. Imperfections such as non uniformity in Λ or effective indices (N_E, N_M) along the device can lead to deviations from the phase-matching condition, i.e. $\partial \Delta K / \partial x_1 \neq 0$, that will subsequently induce broadening of the passband. In addition, this also produces a reduction in the maximum efficiency. We believe that the error in Λ can be considered negligible thanks to the photolithography precision while the error due to refractive index variation, e.g. Ti-$LiNbO_3$ channel waveguide and/or variation in the birefringence of the $LiNbO_3$ crystal, is more likely to occur. Errors in birefringence lead to a reduction in the interaction length and thus in optimum filter length, as it is given by Eq. (2.47). Errors due to waveguide fabrication will lead to certain maximum interaction length which is named the *coherence length* (L_c), as we introduce in the following part.

We assume that we are converting from a TE mode (N_E) to a TM mode (N_M) via an AO interaction. In the ideal case, for maximum power conversion into the TM mode, the following condition needs to be satisfied:

$$\left((2\pi / \lambda_c) N_M L - (2\pi / \lambda_c) N_E L\right) = N 2\pi \qquad (3.43)$$

However, due to the errors, the converted electromagnetic field start going out-of-phase and the total power in the TM mode will thus start decreasing. This poses a limit on the length of the structure to a value L_c. In fact the phase difference between the TE and TM mode at the end of the structure should not exceed π with

respect to the value given in Eq. 3.43. Such condition can be expressed as:

$$2\pi/\lambda_c \int_0^{L_c} \left(N_M(x_1) - N_E(x_1)\right) dx_1 = N2\pi \pm \pi \qquad (3.44)$$

We have assumed that the error is linear in x_1 as given by $N_{M(E)}(x_1) = N_{M(E)} + \left(\partial N_{M(E)}/\partial x_1\right)x_1$. By inserting this relation into Eq. 3.44 and applying Eq. 3.43, we obtain the coherence length of the filter:

$$L_c = \sqrt{\frac{\lambda_c}{\left|\partial N_M/\partial x_1 - \partial N_E/\partial x_1\right|}} \qquad (3.45)$$

3.9 Summary on the AO filter design

Based on the previous sections, the following table presents the summary of the required parameters that need to be taken into account in order to obtain the desired performance filter performance.

Table 3.2: Summary of critical parameters for the design of an AO filter.

Objective	AO Requirement
Telecommunication window	λ_c = 1456 nm (E-band) with 6 nm wide Ti-$LiNbO_3$
Maximum efficiency	$\kappa L = (l + 1/2)\pi$
Small FWHM bandwidth	$\kappa L = \pi/2$, small, large L, L = 10 mm $\Delta\lambda_{FWHM} \approx 2.3$ nm

Small -20 dB distance	Small κ; $\Delta\lambda_{-20dB} \approx 6.3\Delta\lambda_{FWHM} = 14.4$ nm

From Table 3.2, one can conclude that $\kappa L = \pi/2$ for optimum configuration. Taking into account the fabrication errors, the optimum value for L of the ASL filter structure should be smaller than the coherence length (Eq.3.45). To counteract the attenuation, the AO coupling should be larger than $30|\overline{\alpha}|$ for more than 90% polarization conversion.

Chapter 4 - Fabrication and characterization of ASL based AO filters

4.1 Introduction

This chapter describes the fabrication process of the designed ASL based integrated AO filters as well as the characterization techniques and set-ups. The fabrication processes of the ASL structure and of the subsequent coplanar electrodes, which are the building blocks of the ASL transducer, will first be presented. This will be followed by a description of the Ti-$LiNbO_3$ channel waveguide fabrication. RF characterization of the fabricated ASL transducers will then be presented. Furthermore, the scheme of laser interferometry measurement is presented for imaging the SAW displacement. Optical characterization that includes loss measurement of the optical waveguide and AO filter response studies will be presented.

4.2 Device fabrications

Device fabrications, i.e. PPLN, aluminum coplanar electrodes, require lithography processes and wet etching carry out in a clean room environment. Two lithography processes are used employing negative and positive resists, respectively. The main difference between the two processes is that the positive process requires etching to get the desired pattern, while in the negative process the pattern is obtained through lift-off of photoresist with acetone. For clarity, Figure 4.1 and Figure 4.2 show the flowchart for each fabrication process used, i.e. the fabrication steps for the coplanar electrodes.

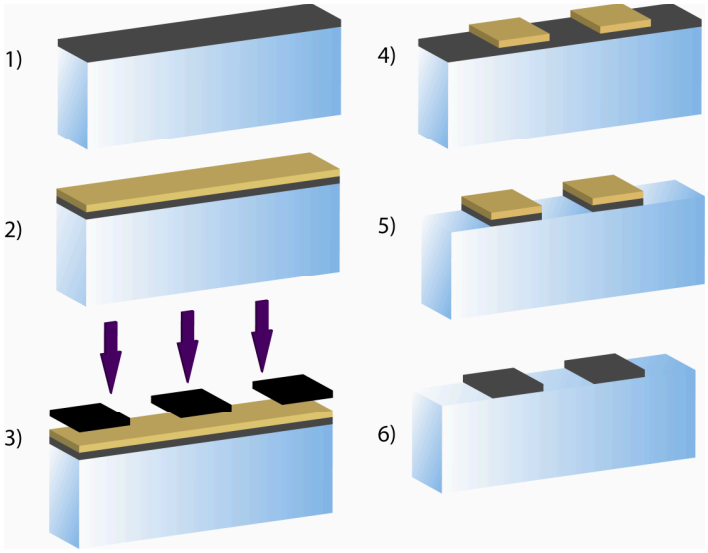

Figure 4.1: Process flow for the fabrication of the coplanar electrodes (1) Aluminum deposition with RF sputtering or thermal evaporation, (2) spin coating of positive photoresist (S-1813), (3) photo lithography, (4) development, (5) wet etching in aluminum etchant, and (6) sample cleaning with standard cleaning process.

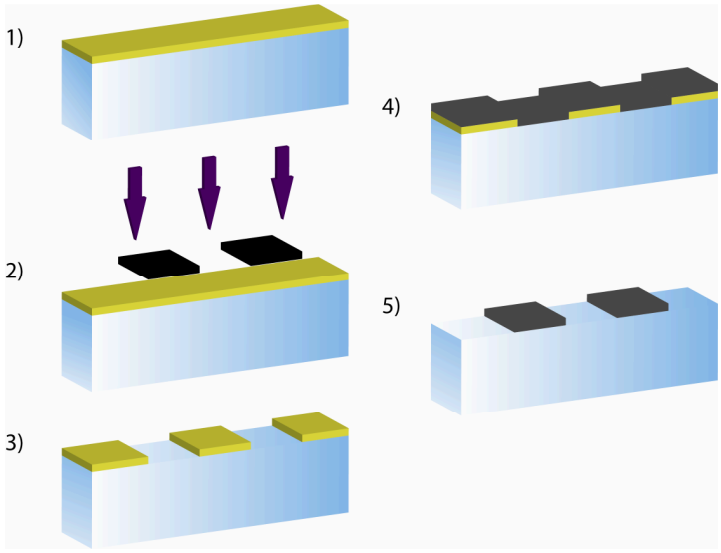

Figure 4.2: Process flow for the fabrication of the coplanar electrodes (1) spin coating of negative photoresist (AZ-5214), (2)

photo lithography, (3) development, (4) aluminum deposition with RF sputtering or thermal evaporation, and (5) lift-off of photoresist with acetone.

The steps for each process are the following ones:

Positive process:

- 1.5 μm thick S-1813 photoresist is spin coated onto the sample,
- Baking on hotplate at 90^{o} C for 5 minutes,
- UV light exposition using mask-aligner for 5.1 seconds (36 mW/cm^{2} energy),
- Development using AZ 726 solution for 40 seconds.

Negative process:

- 1.5 μm thick AZ-5214 photoresist is spin coated onto the sample,
- Baking on hotplate at 90^{o} C for 2 minutes,
- UV light exposition using mask-aligner for 5.1 seconds (36 mW/cm^{2} energy),
- Reverse bake with on hot plate at 90^{o} C for 1 minutes and 30 seconds,
- Flooding (no mask) for 18 seconds (210 mW/cm^{2} energy),
- Development using AZ 726 solution for 1 minutes 20 seconds.

The lift-off of photoresist is carried out with acetone.

4.2.1 PPLN for the acoustic superlattice (ASL) structure

For the fabrication of ASL structures, electric field poling is used [52]. The scheme of the poling setup is shown in Figure 4.3.

Lattice period of the ASL structure (PPLN) will determine the desired center wavelength (λ_c) of the filter as it is explained in the previous chapter. So, although from the design, 20 µm periods ASL transducer is suggested for the filter application, for the sake of the ASL transducer analysis, various ASL structures with different lattice periods (Λ): 15, 20, and 25 µm, are realized in this thesis work.

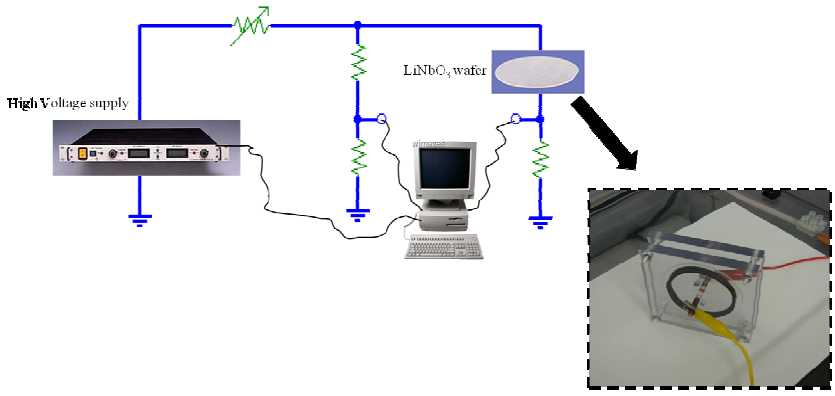

Figure 4.3: A scheme of the electric-field poling setup.

First, an insulator is deposited on +Z face to obtain gratings with the desired period (Λ = 15, 20, and 25 µm) (Figure 4.4), allowing applying the electric field only on the opened area of the substrate surface. Contact is made (see Figure 4.4) to the exposed $LiNbO_3$ surface with a liquid electrolyte consisting of LiCl in deionized water. Finally, after the application of the high voltage,

domain inversion is obtained in the region where the insulator is missing.

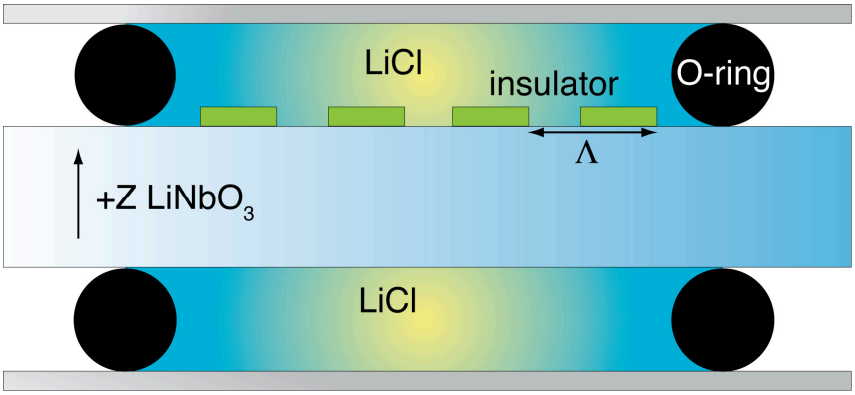

Figure 4.4: Electrode contact with electrolyte solution (LiCl) for the application of electric field for poling.

Figure 4.5: Microscope image of a sample of fabricated PPLN after etching.

The inverted domain (-Z) can be revealed by wet etching in an HF solution concentration. The etch rate is around 10 nm/min. The revealing of the domain allows the analysis of the quality of the poling, and also makes the alignment easier in lithography process for electrodes fabrication. Figure 4.5 shows a microscope photograph of an example of fabricated ASL structure with 20 μm period and 50% duty cycle, the picture obtained after 3 minutes HF etching. Note that for the filter application, the samples are not etched to reveal the domains in order to avoid unwanted optical scattering by the gratings as a result of etching.

4.2.2 Ti-$LiNbO_3$ channel waveguide

The Ti-$LiNbO_3$ waveguides are fabricated before the poling [52]. A 110 nm thick (τ) Ti film is deposited on +Z face sample substrate and the width of Ti strip (W_{Ti}) is, e.g. = 5.5 μm, to get a 6 μm wide waveguide. The samples are then placed inside a furnace for Ti diffusion at temperature (T) around 1060^{o}C for 7 hours (t). These parameters are also used in the modeling for modal calculation (see Chapter 3). A photograph of the fabricated channel waveguides is shown in Figure 4.6.

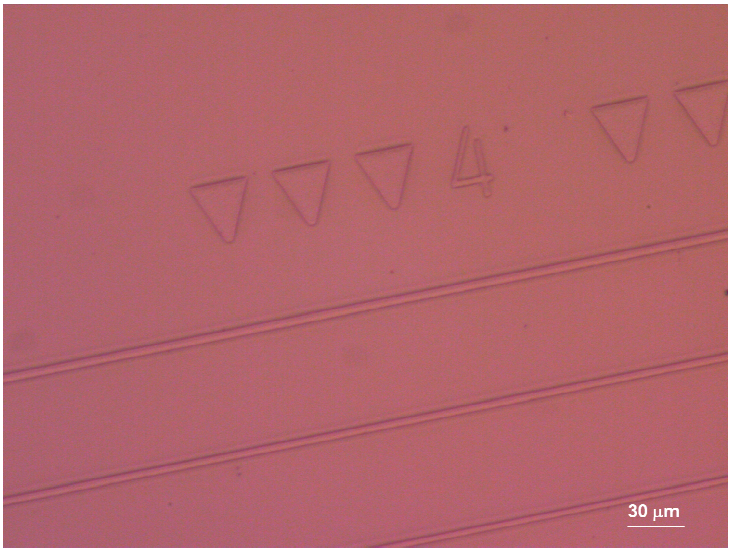

Figure 4.6: A microscope photograph showing 5, 6 and 7 μm wide Ti-$LiNbO_3$ waveguide.

4.2.3 Dicing and polishing

For the filter application, the wafer is diced to get 25 mm by 15 mm chip. In order to increase the optical coupling input and output efficiencies and to avoid back reflection effects of the SAW, the sample's edges are polished at $\theta=8^{\circ}$ (Figure 4.7).

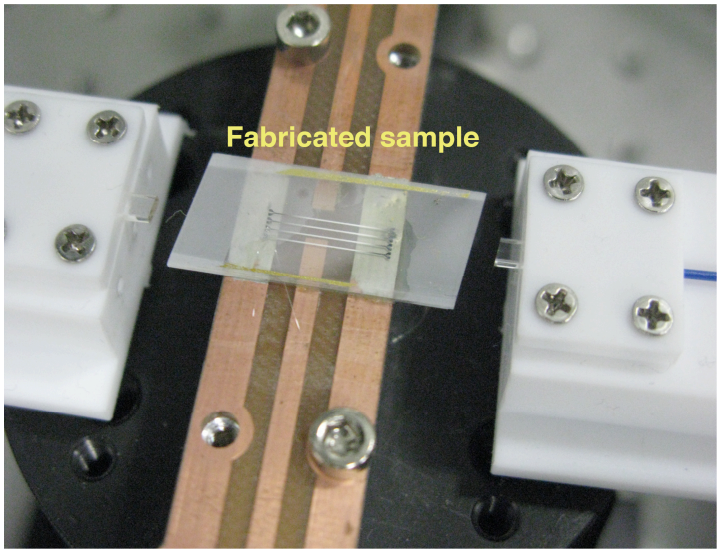

Figure 4.7: Fabricate ASL transducer at butt-coupling using commercial input and output fibre blocks.

4.2.4 Coplanar electrodes

The sample is first cleaned with a standard cleaning procedure to remove any dirt or any contaminations, e.g. dust, residue of photoresists, etc, from the surface of the substrate. The cleaning step of 5 minutes is inside a beaker filled with an acetone solution and in an ultrasonic bath; after that, the sample is cleaned with an ethanol solution and placed on an orbital shaker for about 5 minutes; and finally the sample is dried up with an N_2 gun. If a more thorough cleaning is required, a piranha solution could be used. The piranha solution is a mixture of H_2O_2 and Sulfuric acid/water with 3:1 composition. Sample cleaning with Piranha should be considered only in extreme cases since the heat produced as a result of the chemical reaction could induce mechanical stress

in the $LiNbO_3$ substrate, hence damaging or breaking the sample. In addition, an optional 5 minutes cleaning with UV Ozone could also be performed.

The fabrication flowchart for the electrodes including all the steps is shown in Figure 4. and Figure 4.2. A microscope photograph of a fabricated coplanar electrode is shown in Figure 4.8. Note that during the alignment with the mask-aligner, the mask should be carefully aligned. In particular for the filter application, the electrodes have to be aligned so that the waveguide is at the center of the gap region between the electrodes and the electrodes are parallel to the waveguide. Errors in the alignment could affect the overall filter's performances.

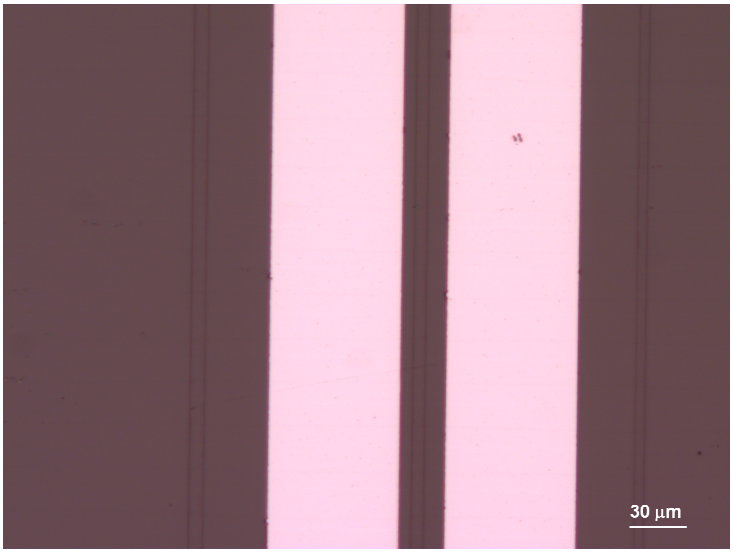

Figure 4.8: A microscope photograph of fabricated coplanar electrodes with width W = 60 µm and gap G_E = 20 µm.

4.3 Characterizations

4.3.1 RF characterization of ASL transducer devices

The fabricated ASL transducer devices are characterized using a network analyzer (NA) Agilent (PNA 5242) and a Karl Suss PM5 probe station to determine the S electrical parameters. Signal and ground probe tips (Picoprobe) with a separation of 200 µm are used for the RF connection to the pad of the electrodes. The one-port measurement is performed by connecting one transducer as it is illustrated in Figure 4.9, while the two-ports measurement requires two transducers: emitting and receiving transducer, as it is shown in Figure 4.10. A photograph of the RF characterization setup is shown in Figure 4.11.

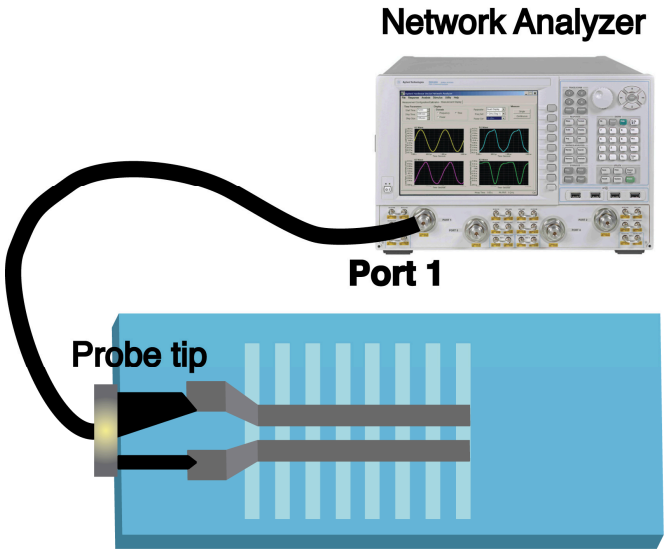

Figure 4.9: Scheme of one-port measurement for the characterization reflection response of the ASL transducer.

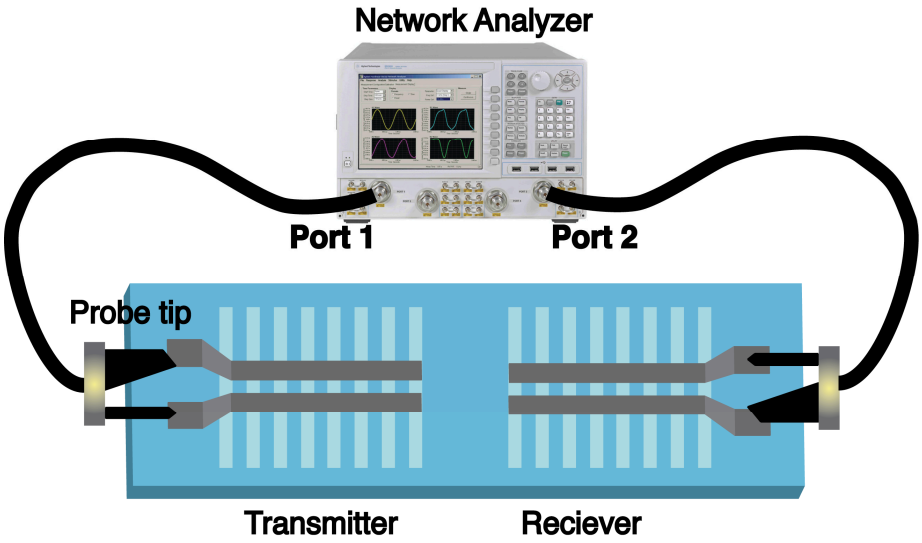

Figure 4.10: Scheme of two- ports measurement that includes emitting and receiving transducers for the acoustic wave propagation measurements.

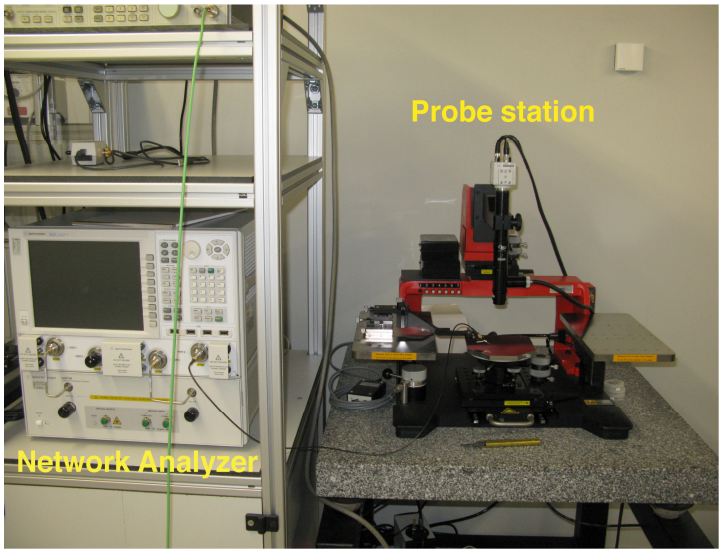

Figure 4.11: RF characterization setup.

RF frequency ranging from 100 MHz to 500 MHz with 5000 scanning points is set by the NA, covering all possible acoustic wave resonances in the transducer.

4.3.2 Laser interferometry measurement

For a direct detection of elastic energy distribution and deformation associated to the SAW generated by the ASL transducer, the out-plane motion of the substrate surface is imaged using an optical heterodyne interferometer, which is provided by the MINANO group at Institute FEMTO-ST, Besancon, France. The setup used is similar to that described in ref. [53]. It allows amplitude detection of out-of-plane component, which, in our case, corresponds to the $|u_3|$ component. The measurement setup is shown in Figure 4.12.

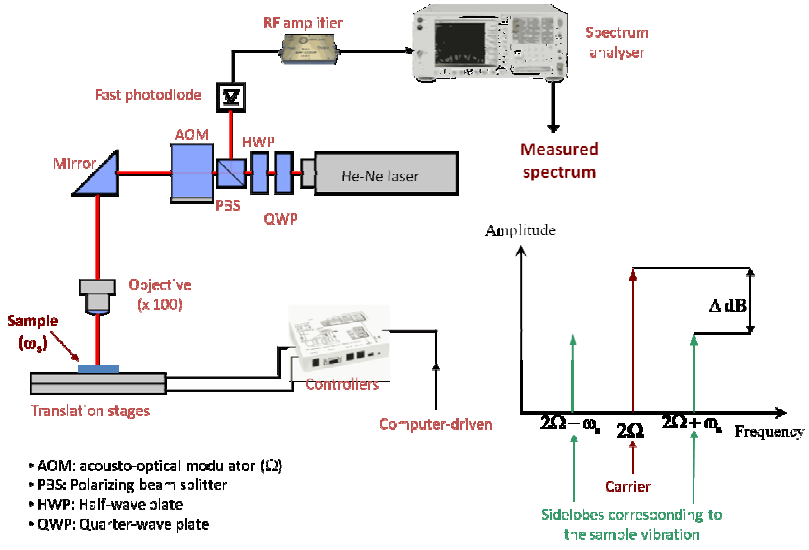

Figure 4.12: Laser interforemetry measurement setup of SAW energy and displacement.

The scanning mechanism uses a reflected laser beam from the substrate surface of the sample under measurement. The beam is generated by a He-Ne laser source and is modulated by an AO modulator (AOM) before it is focused by microscope objective onto the sample. The reflected beam is picked up by a fast photodiode and is analyzed via an RF spectrum analyzer. A typical measured spectrum is shown in the inset of Figure 4.12. The presence of the SAW (amplitude of u_3 component) will be determined by the difference in the amplitude measured at the carrier frequency of the AOM and the amplitude measured at the frequency corresponding to the sample vibration (the SAW), as described by the inset of Figure 4.12.

4.3.3 Channel waveguides

Good performance from an integrated optical filter requires high quality channel waveguides exhibiting low insertion loss (IL). The insertion intensity loss of a waveguide is defined in dB as:

$$IL\ (\text{dB}) = -10\log\left(\frac{P_{\text{out}}}{P_{\text{in}}}\right) \tag{4.1}$$

where P_{in} and P_{out} are the input and output powers of the waveguide, respectively.

There are three primary loss components contributing to the fiber-waveguide insertion loss: 1) Fresnel loss, 2) mode mismatch loss, and 3) propagation loss [54]. Fresnel loss results from the

optical reflections at both ends of a waveguide and can be roughly estimated in the following way:

$$Fresnel\ loss\,(dB) = -20\log(1-R) \tag{4.2}$$

where $R = [(1-n_i)/(1+n_i)]^2$ with i = extraordinary (e) or ordinary (o) depending on the polarization state of the propagating mode. The Fresnel loss at the edges of the waveguide actually can be reduced with an index-matching liquid or an antireflection coating [55]. The mode mismatch loss is caused by a different field profile between an optical fiber and a Ti indiffused $LiNbO_3$ waveguide. This can be evaluated by the overlap integral between the two modes. Once the insertion, Fresnel loss, and mode mismatch loss are known, the propagation loss for the waveguide can be obtained (in the unit of dB/cm):

$$\text{Propagation loss (dB/cm)} = \frac{IL - (Fresnel\ loss + mode\ mismatch\ loss)}{L} \tag{4.3}$$

The measurement step for the insertion loss is shown in Figure 4.13. A pigtailed HP 8168F tunable laser source at around 1550 nm is the optical source. A polarization maintaining (PM) fiber is aligned along the slow axis for optical transmission measurements. A pigtailing station is used to couple light into and out of the waveguide through a pair of commercial single mode fiber blocks in butt-coupling. The output optical signal is detected with a Ge photodetector and the output power is measured with a power meter.

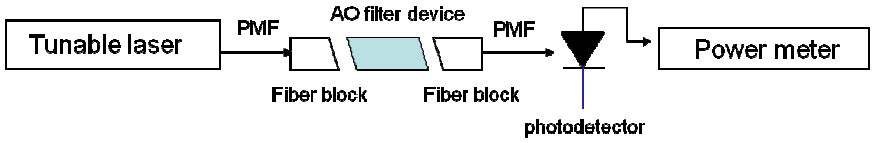

Figure 4.13: Set up for measuring the insertion loss in fabricated Ti-$LiNbO_3$ channel optical waveguides

Although three different width (5, 6, and 7 μm) channel waveguides are realized, for simplicity we consider here only those with 6 μm width. For those we performed insertion loss measurements with TE polarized light.

4.3.4 AO measurements

Integrated AO filter

The measurement set up used for AO characterization is shown in Figure 4.15. A Supercontinuum laser source from SuperK is used to generate a broad spectrum in the wavelength region of interest and the same pigtailing station as that for the optical characterization is used to couple light in and out of the waveguide. Polarizer (P) and analyzer (A) are placed before and after the sample. An Optical Spectrum Analyzer (OSA) from Yokogawa (AQ6370) is used to monitor the optical output. For the acoustic generation, an HP8642B RF signal generator and an RF amplifier from MiniCircuits are employed, this allowing reaching an output RF power in excess of 20 dBm The data acquisition is automated with a LABVIEW program.

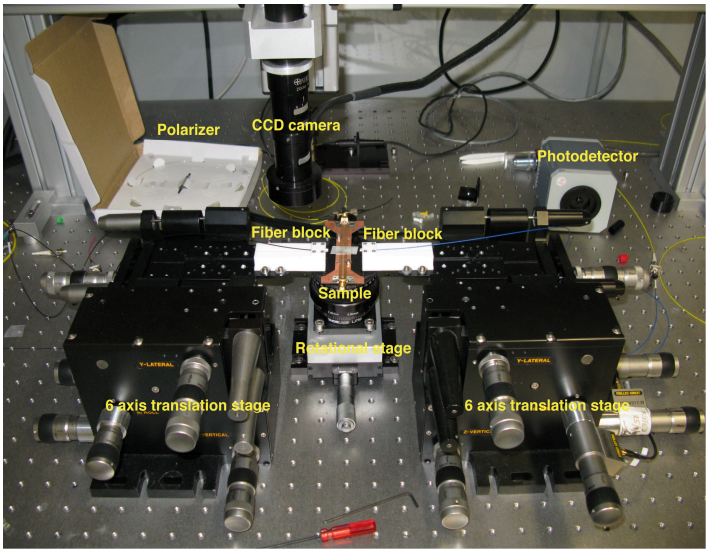

Figure 4.14: Optical measurement setup.

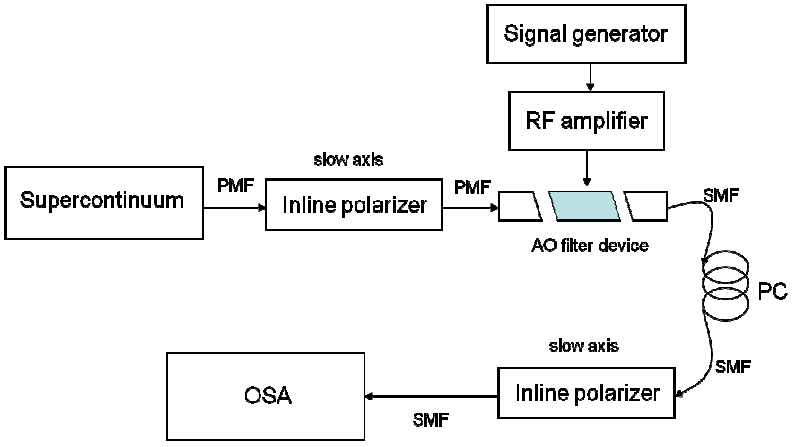

Figure 4.15: AO measurement setup. PMF and SMF are polarization maintaining and single mode fiber, respectively, PC is polarization controller.

Initially a reference optical signal is measured at $P_{RF} = 0$ (in the absence of any elastic wave). To this end, the polarizer and the analyzer are set to be parallel with respect to each other and the output optical power is measured at the optical wavelength around

the phase-matching, denoted by $P_{//}$. After that, the same measurement is repeated with orthogonal polarizer and analyzer, and the output power is measured, denoted by $P_{\perp}$. The difference between the measured optical powers gives us the reference signal denoted by $P_{\text{reff}} = |P_{//} - P_{\perp}|$, which will be used for the determination of the conversion efficiency (η) as it will be described below. For the rest of the AO measurement, the polarizer and the analyzer are kept orthogonal to each other.

For the conversion efficiency measurement, the RF frequency is set at SAW the resonance frequency resonance, and the input RF power is slowly increased. For each input RF power, the optical output (P) is measured around the phase matching wavelength. The measured conversion efficiency of the filter (η) is calculated as:

$$\eta = \left. \frac{P_{\text{on}}}{P_{\text{reff}}} \right|_{\lambda_0 = \lambda_c} \tag{4.4}$$

where $P_{\text{on}} = |P - P_{\perp}|$.

Bulk AO filter

The experimental setup is somewhat similar to that used for the integrated filter measurement, but the beam is coupled into the device with a fiber collimator while a second fiber collimator picked up the output beam. The distance between the fiber collimator and the device is set so that the beam waist in the center of the device. Since the sample's edges are polished at $\theta = 8^{\circ}$, the

sample is positioned on the translational stage, in that way the incoming beam propagates parallel to the electrodes for collinear AO interaction, an also at the center of the transducer. To refine the alignment, a design with ZEMAX is carried out. Figure 4.16 shows the actual optical alignment for bulk AO filter measurements

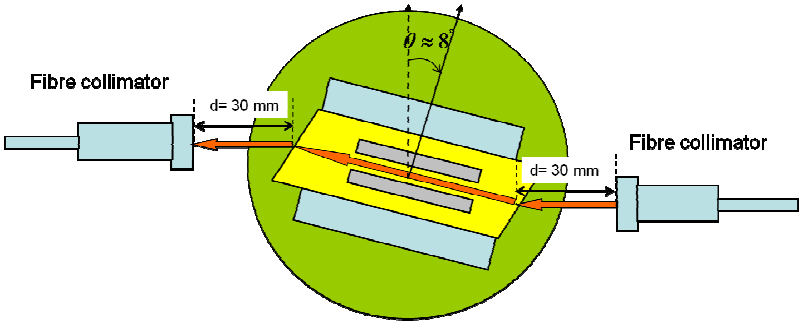

Figure 4.16: Optical alignment for collinear bulk AO measurement.

Chapter 5 - Device concepts

5.1 Introduction

In this chapter we present the conceptual designs of ASL transducer and the corresponding AO filter, together with their experimental assessments. Ways of optimizing the filter's performance particularly with respect to the filter efficiency in terms of driving RF power will be presented and discussed.

5.2 ASL transducer for acoustic wave generation

The characteristics of the excited acoustic wave in an ASL transducer are first analyzed. After that, the coupling (K^2) measurements are carried out to examine the performance of the ASL transducer for generating SAW. Transmission measurements are performed to characterize the acoustic wave propagation. In these measurements, the width and the gap of the electrodes are maintained fixed ($W = G_E = 100$ μm), so is their length (10mm), with the exception of the coupling measurement where the electrode length is varied on purpose. Note that in general the electrode length is equal to that of the ASL structure. Finally, to experimentally validate the theoretical results of Chapter 3, several devices having a pair of coplanar electrodes with different electrode width are characterized. Figure 5.1 illustrates the proposed ASL transducer.

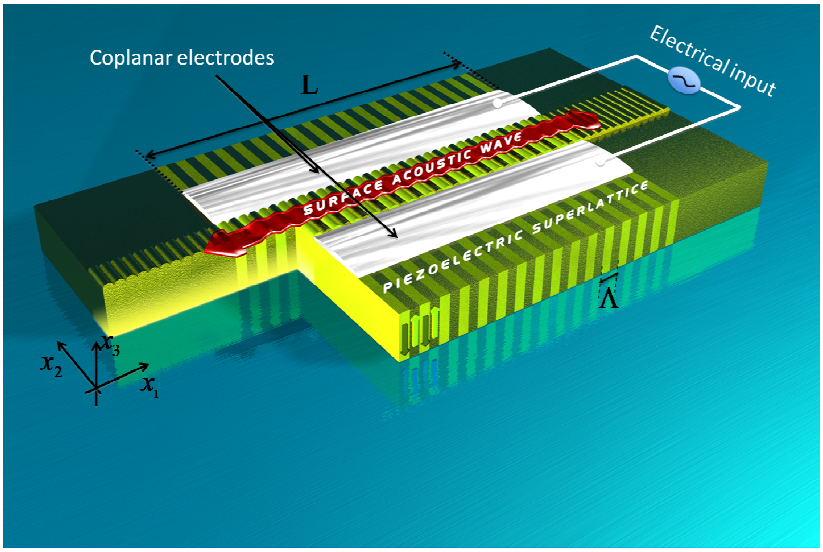

Figure 5.1: A structure of ASL based transducer in ZX-cut PPLN with coplanar aluminum electrodes configuration.

5.2.1 Characteristics of excited acoustic waves in the ASL transducer

In order to analyze the characteristics of the excited waves in the ASL transducer, the reflectance response (S11 parameter) of the transducer is measured as it is shown in Figure 4.9. For 20 μm period ASL transducer the measurements are shown in Figure 5.2.

Figure 5.2 shows two pronounced dips observed at around 190 MHz and 330 MHz corresponding to the excitation of a Rayleigh SAW and of L-BAW, propagating at 3800 m/s and 6600 m/ velocities, respectively. Two additional dips, which are less pronounced, are observed at around 220 MHz and 380 MHz, corresponding to the excitation of a leaky SAW (L-SAW) and the 2nd-harmonic of the generated SAW, respectively. The L-SAW is

mainly a shear horizontal (SH) acoustic wave propagating at 4400 m/s velocity in ZX $LiNbO_3$ [56], [57]. Higher harmonics L-BAW are also observed at 660, 990 MHz, which are not shown for clarity.

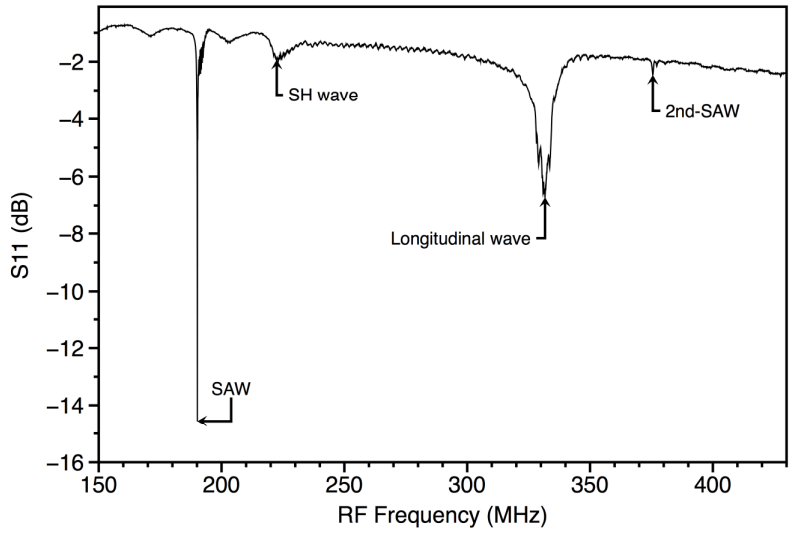

Figure 5.2: S11 as a function of RF frequency measured for a 20 μm period ASL transducer.

To further investigate the SAW and the L-BAW excitations and their dependence on the lattice period (Λ) of the ASL, two additional ASL transducers with different lattice periods (15 μm and 25 μm) are realized and characterized. The measured S11 parameters for each device are given in Figure 5.3 and Figure 5.4. The summary of the results is presented in Table 5.1. The experimental results follow well the prediction of Eq. 1.1 with λ = Λ, as well as the SAW and L-BAW excitations in an ASL transducer as it was predicted by the modeling in Chapter 3.

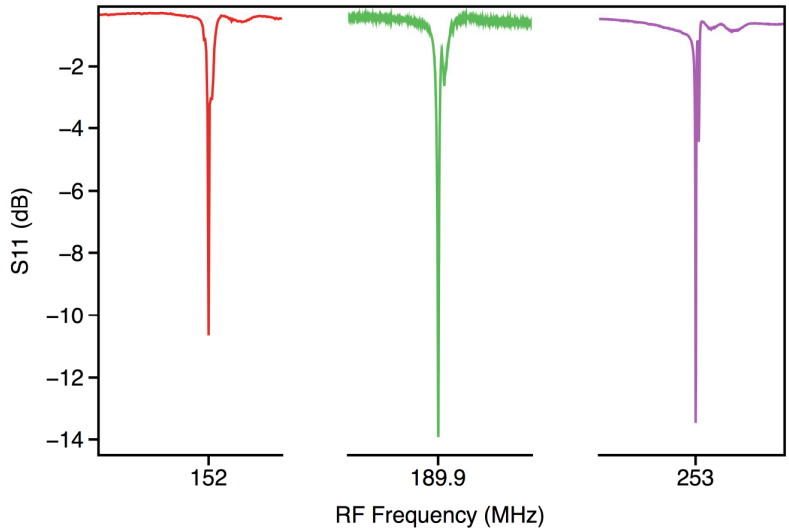

Figure 5.3: S11 parameters as a function of RF frequency measured around SAW resonance frequency for 15, 20, and 25 μm period ASL transducers, respectively.

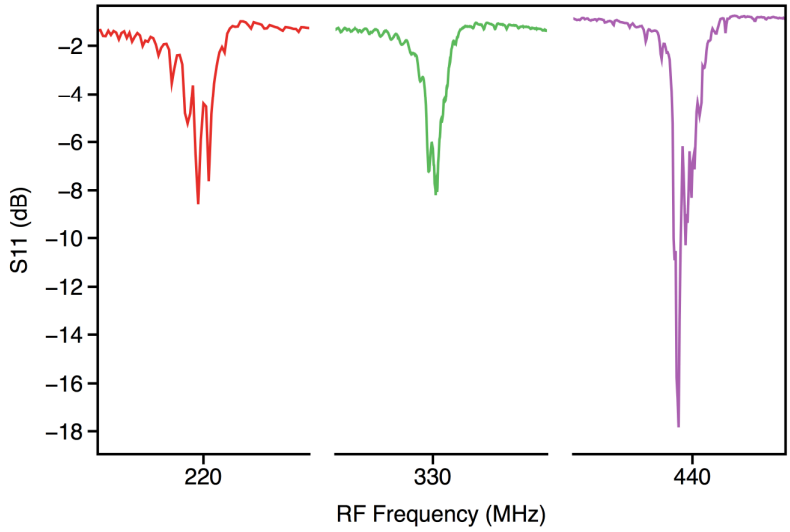

Figure 5.4: S11 parameters as a function of RF frequency measured around L-BAW resonance frequency for 15, 20, and 25 μm period ASL transducers, respectively.

Table 5.1: Summary of S11 measurements for 15, 20, and 25 μm period ASL transducers.

	SAW		L-BAW	
Lattice period (Λ) (μm)	Resonance frequency (*f*) (MHz)	Velocity = *f* x Λ (m/s)	Resonance frequency (*f*) (MHz)	Velocity Velocity = *f* x Λ (m/s)
15	253	3795	440	6600
20	190	3800	330	6600
25	152	3800	264	6600

Furthermore, as one can expect, acoustic wave generation is not observed for unpoled samples using the same electrode configuration as it is shown in Figure 5.5.

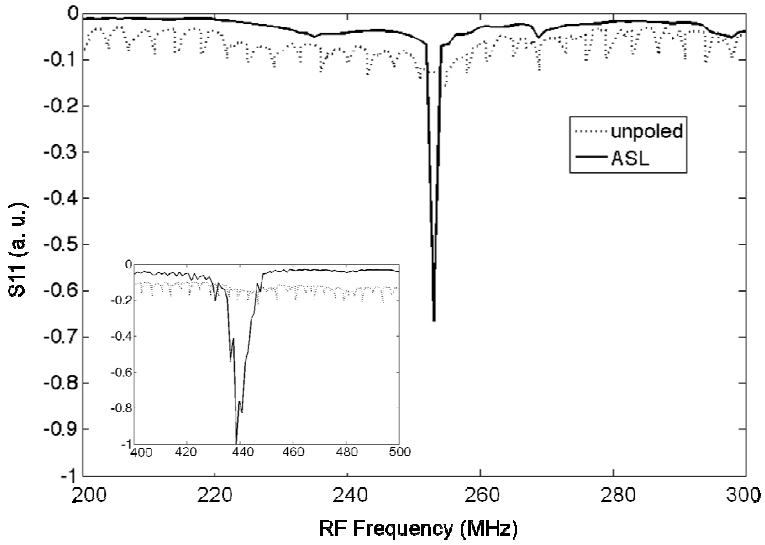

Figure 5.5: S11 parameters as a function of frequency for the ASL transducer (15 μm period, 10 mm length). Solid and

dashed lines correspond to measurements with and without ASL, respectively.

The characteristics of the acoustic wave excited by the ASL transducer, e.g. 15 µm periods, are compared with that of a standard IDT. To this end 7.5 µm period (λ = 15 µm) IDT consisting of 330 fingers is deposited on unpoled ZX-$LiNbO_3$ substrate by means of lift-off as it is described in Figure 4.2. The measured S11 for the ASL and the IDT are shown in Figure 5.6.

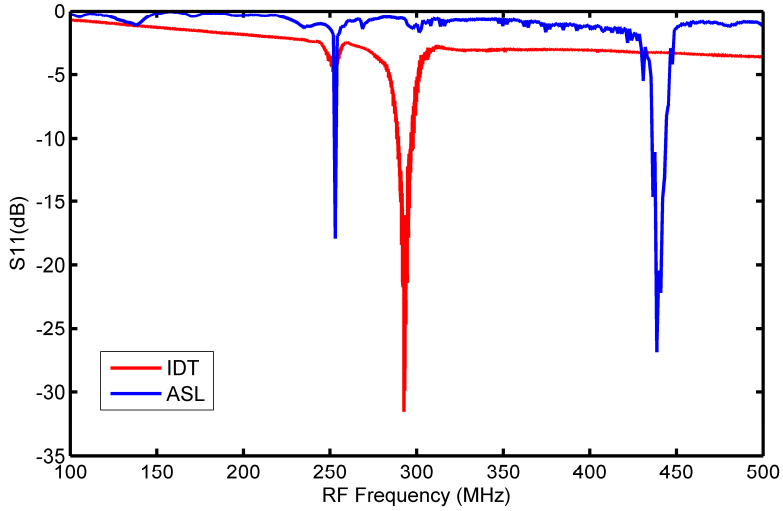

Figure 5.6: Scattering parameters (S11) as a function of RF frequency for 15 µm period ASL and 7.5 µm period IDT transducer.

Figure 5.6 shows that in both IDT and ASL transducer a SAW is excited at a frequency of 253 MHz. A strong dip for the IDT is observed at around 290 MHz, corresponding to the L-SAW excitation, which is much stronger than in the ASL case. The weak

L-SAW excitation in the case of coplanar uniform electrode ASL transducer can be explained by the fact that the electric field is mainly produced in the x_3 and x_2 directions, while, in the case of IDT, it has x_3 and x_1 components. Consequently the 6th component of the stress tensor (T) that contributes to L-SAW generation is no longer piezoelectrically active as the eE product cancels out. This actually prevents satisfying the stress free boundary condition for L-SAW.

5.2.2 Coupling (K^2) measurement

To retrieve the electromechanical coupling coefficient (K^2) of the ASL transducer, various electrode lengths, i.e. 4, 6 ,8, and 10 mm, are chosen and realized, while keeping the rest of the parameters fixed, to assess the influence of the ASL length on the transduction efficiency. For this experiment, the ASL structure has a period of 15 μm.

The scattering parameters (S11) for each electrode length are measured. To determine the coupling coefficient (K^2), the impulse model (Eq. 2.23) presented in the previous chapter is employed. The measured S11 is converted into the admittance (Y) using the following relation:

$$Y = \frac{1}{Z}\left(\frac{1-S_{11}}{1+S_{11}}\right) \tag{5.1}$$

where Z denotes the characteristic impedance of the system (50 Ohm). The corresponding radiation conductance (G_a) of the device becomes:

$$G_a = \mathrm{Re}(Y) \tag{5.2}$$

The measured conductance (G_a) for various electrodes length is given in Figure 5.7. As it is expected, a strong peak around the resonance frequency is obtained, indicating optimum transduction in the form of SAW generation. The value of G_a at the resonance frequency increases with the electrode length and reaches maximized for 10 mm (see Figure 5.7(d)), as a consequence of a maximum overlap between the electrodes and the ASL domain. By fitting the experimentally obtained conductance G_a using the expression given in Eq. 2.23. the electromechanical coupling coefficient (K^2) could be obtained and is shown in Figure 5.8.

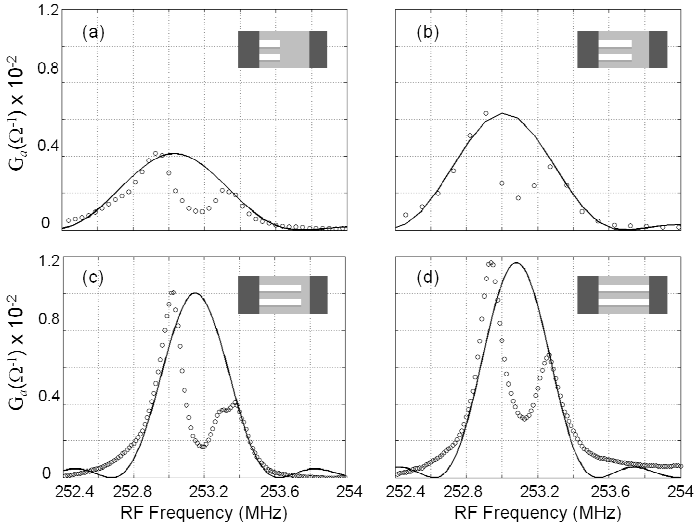

Figure 5.7: Conductance (G_a) (circles) of the ASL samples with different electrodes length: (a). 4 mm, (b). 6 mm, (c). 8 mm, and (d). 10 mm. Solid lines denote the corresponding fitting curves. The insets illustrate the variation of the electrode length with respect to that of the ASL.

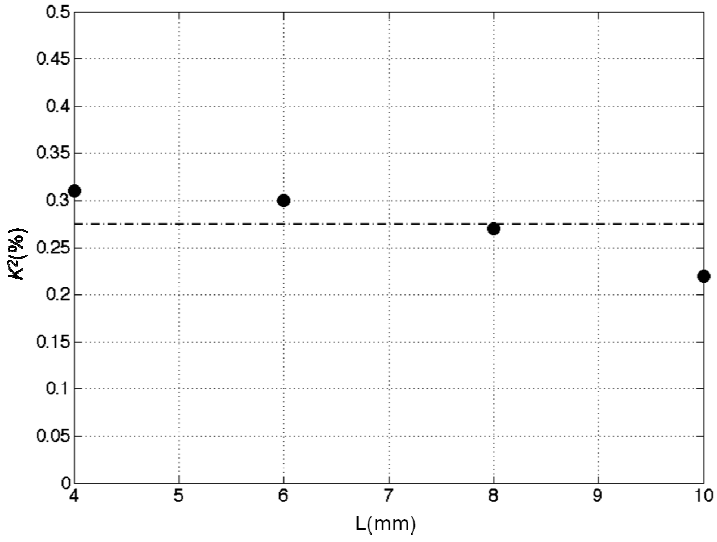

Figure 5.8: Measured electromechanical coupling coefficient (K^2) of the ASL as a function of electrode length. The dashed-line denotes the average K^2.

The average K^2 obtained is approximately 0.3% while a theoretical value is of 0.53% given in Table 2.3 for ZX-$LiNbO_3$. But, as it is shown in Figure 5.8, K^2 decreases as the length of the electrodes increases, indicating that the overlap between electrodes and inverted domains is not the only parameter to be taken into account for device optimization. A possible explanation for this dependence on length lies in the increase of diffraction losses with propagation distance as well as in the existence of imperfections in the ASL structure.

5.2.3 Transmission measurement

In the transmission measurement, in addition to the emitting ASL transducer, a receiving ASL transducer having similar characteristics is placed about 100 μm (about 6.5 lambdas with λ = 15 μm) away from the emitter to pick up the transmitted acoustic waves. Two-port measurement to determine the S21 parameter is performed along with the S11 parameter.

Figure 5.9 shows the S21 measured at the SAW frequency (253 MHz), which appears to be small, showing that there is little collected signal of the SAW at the resonance frequency. Given that the distance between the transducers is only about 6.5λ, these results, therefore, imply that the SAW energy propagating away from the transmitter is significantly small. In other words, this suggests that a large portion of the SAW energy is localized within the emitter, which basically confirms the modeling that was

presented in Chapter 3. Unlike the SAW, the L-BAW measured at 440 MHz propagates away from the transmitter as it is also indicated by the corresponding relatively large S21 value.

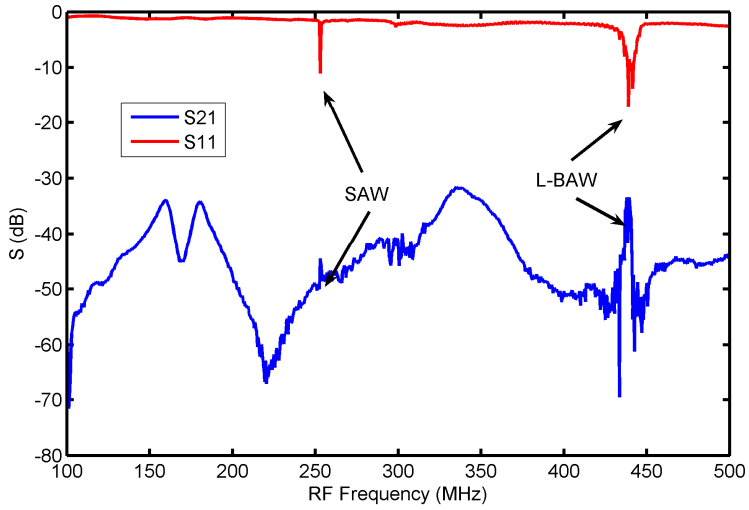

Figure 5.9: S21 and S11 parameters as a function of RF frequency for ASL transducers with 15 µm lattice period. Blue and red lines denote the measured S21 and S11, respectively.

5.2.4 Experimental on validation of the SAW modal excitation on the ASL transducer

In this measurement, various coplanar electrodes with different of electrode width, (W = 40, 60, 80, and 100 µm) and $W = G_E$ fixed, is deposited on 20 µm period ASL structure and S11 measurement is performed on each device. The electrode length is fixed at 10 mm for maximum transduction as explained previously. Figure 5.10 shows the scattering parameters (S11) of each measured device as a function of the RF frequency.

The dips suggest the presence of excited SAW modes in the ASL transducer. For the sake of clarity, the modal velocities (v_g) as a function of the electrode width (W) are calculated from the S11 data using Eq. 1.1, and compared with the calculated results from the modeling (Figure 5.11).

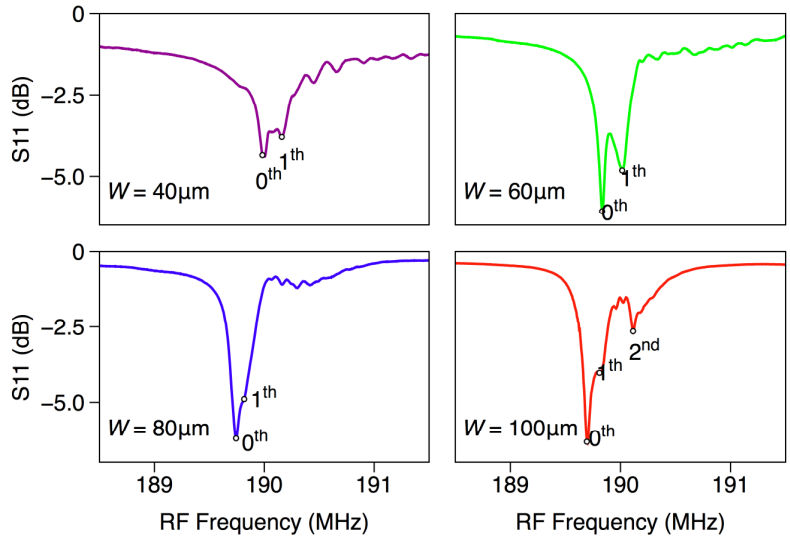

Figure 5.10: Measured scattering parameters (S11) as a function of RF frequency for samples with different electrode widths, W=G_E=40, 60, 80, and 100 μm.

In Figure 5.11, the calculated normalized modal SAW velocity from both calculations, e.g scalar approximation and FEM simulation, and measurements as a function of the electrode width (W) are shown. The measured values differ slightly from those obtained with the calculation. This is probably related to the fact that the number of periods of the ASL transducer in the experiment is finite as opposed to the infinite number considered in the

simulation. The number of measured excited modes and its trend show good agreement with the simulations.

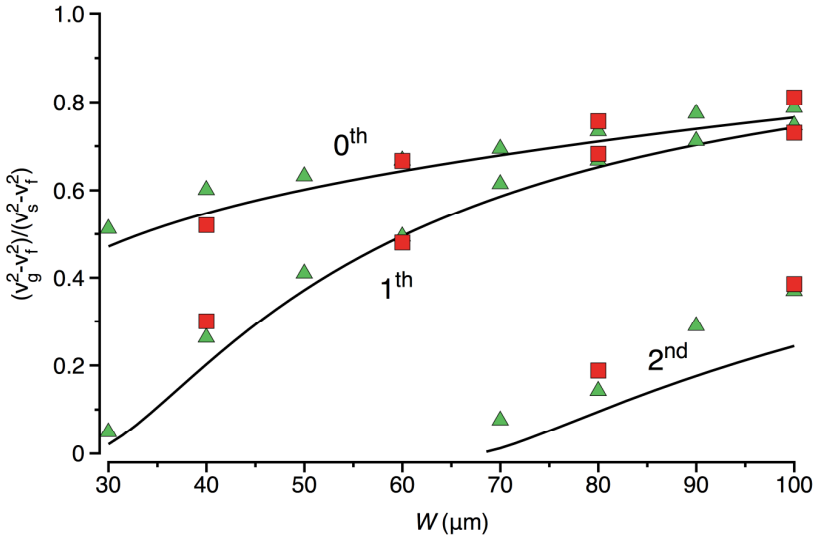

Figure 5.11: Normalized modal velocity as a function of electrode's width (*W*) in a 20 μm period ASL transducer calculated with scalar approximation (solid line) and FEM simulation (*triangles*), respectively. *Rectangle*s refer to measurement results.

To have a confirmation of the energy distribution of the SAW, the out-plane motion of the substrate surface is imaged using an optical heterodyne interferometer following the measurement scheme shown in Figure 4.12. We show the results in Figure 5.12 and the crossed-section of the mode profile across the electrode is shown in Figure 5.13. The maximum displacement in the x_3 direction is about 0.7 nm and the periodic shape reflects the spatial distribution of the PPLN domains using 15 dBm, i.e 31 mW, RF electrical powers.

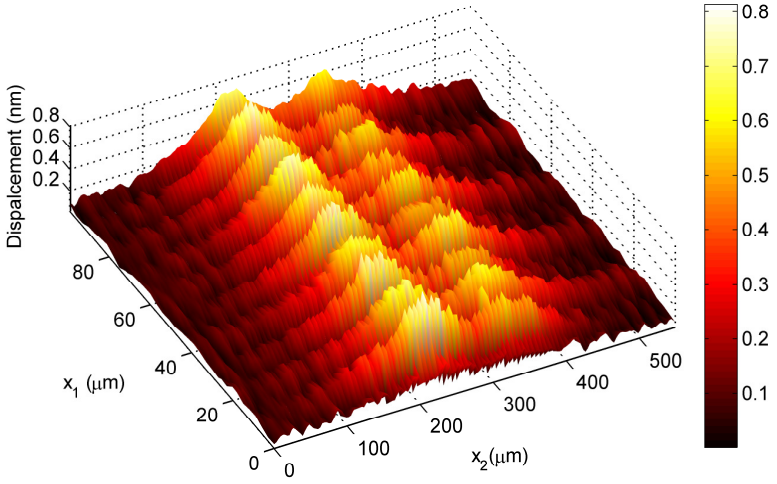

Figure 5.12: Optical mapping of the out of plane component of the fundamental SAW mode excited at frequency 189.8 MHz detected using laser-probing technique on the ASL transducer with $W = G_E = 60$ μm.

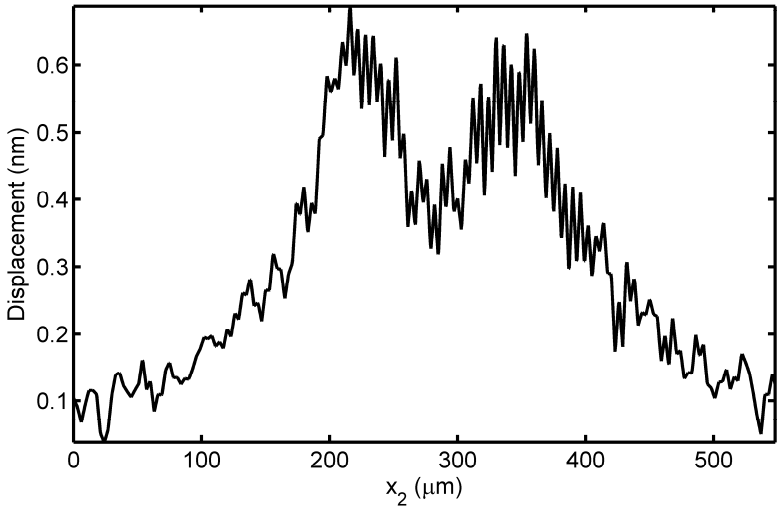

Figure 5.13: The cross-section of the acoustic beam profile along x_2 on the ASL transducer with $W = G_E = 60$ μm.

5.3 Integrated ASL based AO filter

The ASL transducer described above is employed for integrated AO filter devices. The conceptual design of the integrated AO filter is illustrated in Figure 5.14. The ASL transducer consists of a 20 μm lattice period ASL structure and coplanar electrode with $W = G_E$ = 100 μm and a 6 μm Ti-$LiNbO_3$ channel optical waveguide. The optical waveguide is first characterized to determine the insertion loss. Subsequently AO measurements are performed.

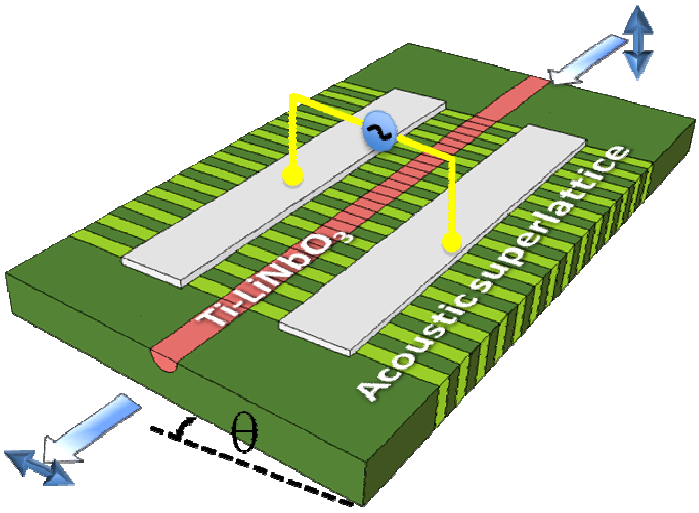

Figure 5.14: Scheme of the proposed integrated AO polarization converter based on ASL transducer with $\theta = 8^o$.

5.3.1 Loss measurement for optical Ti-$LiNbO_3$ channel waveguide

The optical loss measurement is carried out using the setup shown in Figure 4.13. First, the output power is measured without

placing the waveguide for determination of the reference signal. Two this end, the two fiber blocks are butt-coupled. The output power is measured to be -11.1 dBm. Subsequently the output power measurement is repeated with a waveguide placed on a translational stage between the fiber blocks. The insertion loss of the waveguide is thus basically determined by the difference between the measured output powers with and without the waveguide.

Three waveguides separated by 818 μm from one to another are characterized. Table 5.2 summarizes the insertion loss for all measured waveguides. The waveguide 3 has the lowest insertion loss and will be employed for throughout filter applications.

Table 5.2: Insertion loss of 6 μm channel waveguides for TE polarization.

Waveguide	Output power (dBm)	Insertion loss (dB)
1	-19.02	7.92
2	-17.31	6.20
3	-16.89	5.79

5.3.2 AO measurements

We initially characterize the ASL transducer by measuring the scattering parameter S11 and obtained the SAW resonance frequency at f_a = 189.94 MHz. The corresponding impedance match of the device around that frequency is measured to be about 65 Ω. After the electro-acoustic characterization, we measure the AO

response. By keeping P_{RF} constant at 500mW, the RF frequency f_{RF} is swept around the resonance frequency f_a and the optical output is measured around the phase matching wavelength (center wavelength), λ_c = 1456 nm (Figure 5.15). The values reported in Figure 5.15 are normalized to the peak value at phase-matching (Δ=0). At an RF power (P_{RF}) of 500mW and frequency (f_{RF}) equal to f_a (189.94 MHz), the output optical intensity is measured as a function of the wavelength (Figure 5.16). The 3-dB optical bandwidth (FWHM) $\Delta\lambda_{FWHM}$ is 2.51 nm. From Figure 5.15 the acoustic FWHM (Δf) is estimated to be about 310 kHz which is in good agreement with the theoretical prediction (Δf_{th}) $\Delta f_{th} = f_a (\Delta\lambda_{FWHM}/\lambda_c)$ = 327 kHz. From these data and using Eq. 2.45 we can estimate an interaction length L_i=9 mm, very close to the physical electrode length.

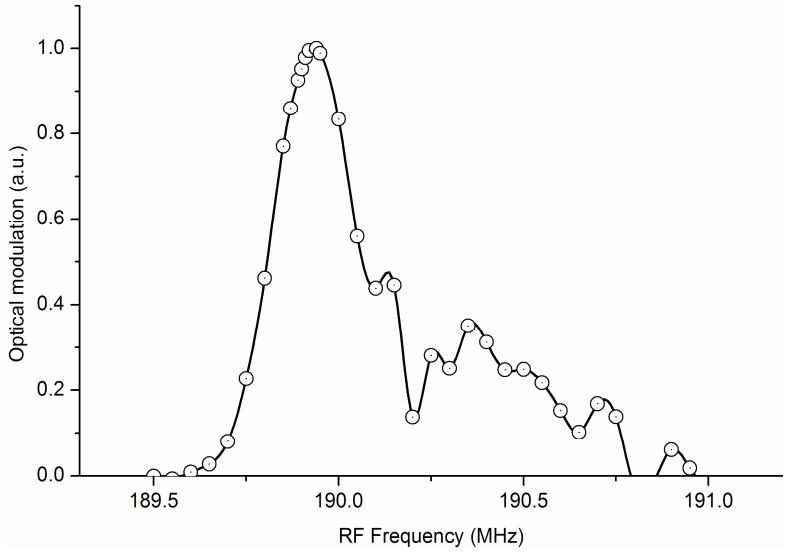

Figure 5.15: AO modulation as a function of RF frequency at center optical wavelength (λ_c =1456 nm) for a P_{RF} of 500mW.

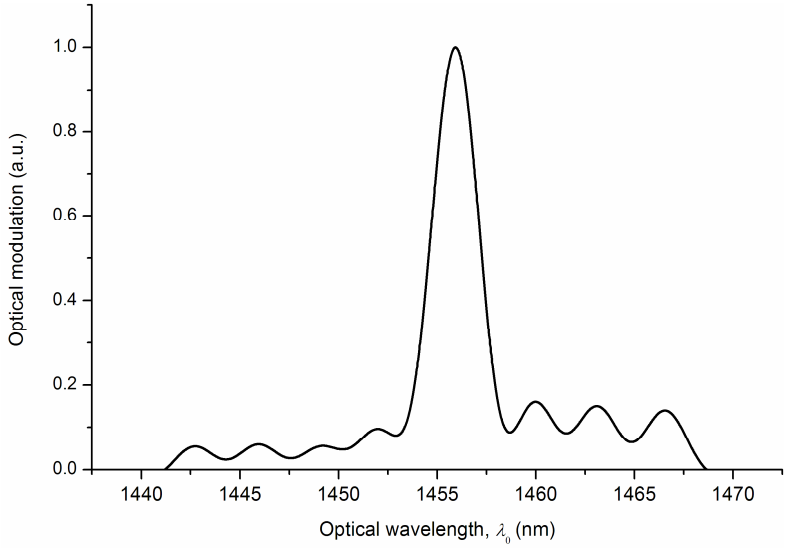

Figure 5.16: Optical modulation as a function of optical wavelength λ_0 for input RF power of 500 mW and RF frequency of 189.94 MHz.

The polarization conversion efficiency (η), i.e. the ratio between converted and transmitted power in the absence of RF signal, as a function of RF power is shown in Figure 5.17, for values of P_{RF} ranging from 100 mW to 1600 mW. One can estimate that 90% conversion is reached for P_{RF} =1W. This shows that the proposed integrated AO device is significantly more efficient than its bulk counterpart previously reported, where, for the same input power, only around 40% mode conversion is achieved [9]. The shift in the center wavelength reported in Figure 5.18 for different P_{RF} is mainly due to thermal drift associated to RF dissipation, as it has already been reported elsewhere, including ref. 9.

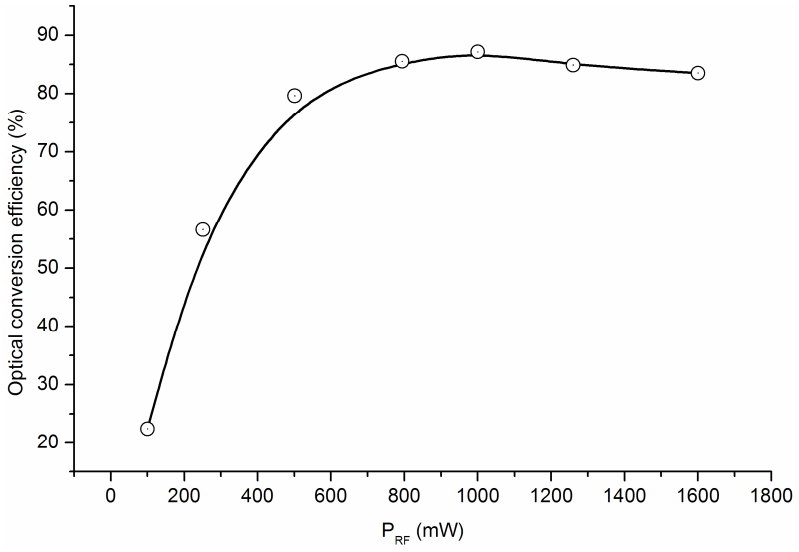

Figure 5.17: Optical conversion efficiency (η) versus RF power (P_{RF}) for the integrated AO filter. The continuous line is a fitting curve to the data.

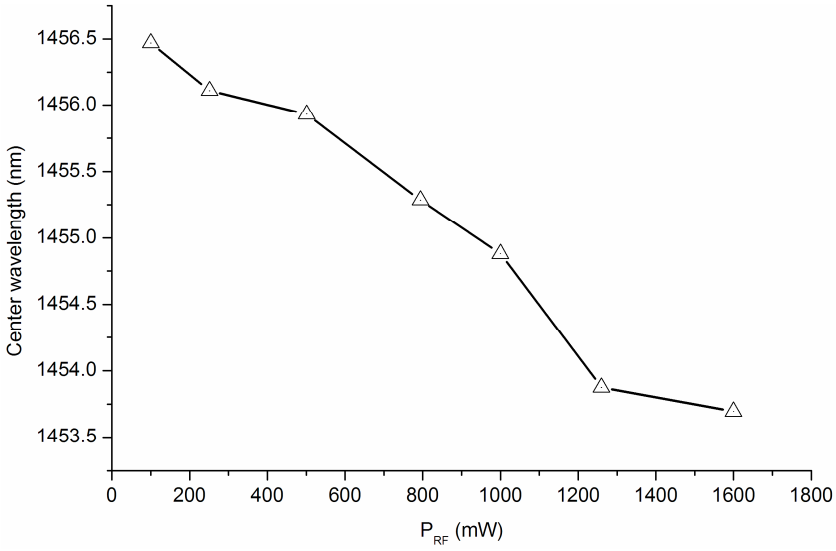

Figure 5.18. Shift of center wavelength (λ_c) observed for different RF power (P_{RF}). The continuous line is a fitting curve to the data.

The -20 dB ($\Delta\lambda_{-20dB}$) distance of the filter is 14.49 nm inferred from Figure 5.19, which is not far from the design value of 14.4 nm (see Tabel 3.2).

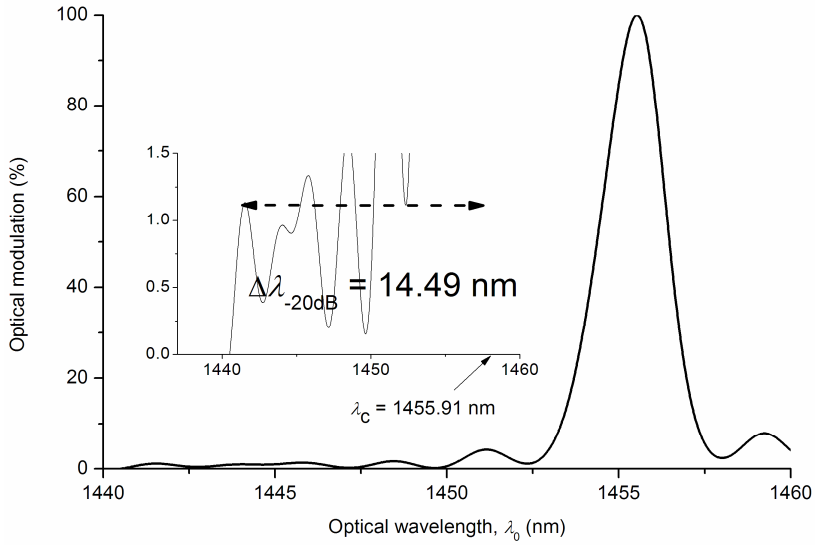

Figure 5.19: Optical modulation as a function of optical wavelength λ_0 for an RF input power of 500 mW and RF frequency of 189.94 MHz. Inset shows the -20 dB distance ($\Delta\lambda_{20dB}$).

5.4 Bulk AO filter

A scheme of the filter is shown in Figure 5.20. The filter consists of an ASL transducer with 20 μm period ASL structure and $W = G_E$ = 100 μm coplanar electrodes, corresponding to L-BAW excitation at a resonance frequency f_a = 330 MHz. Using the calculated bulk refractive indices, $n_{e(o)}$ given in Chapter 3, the phase matching wavelength of the bulk filter is expected to be around 1473 nm.

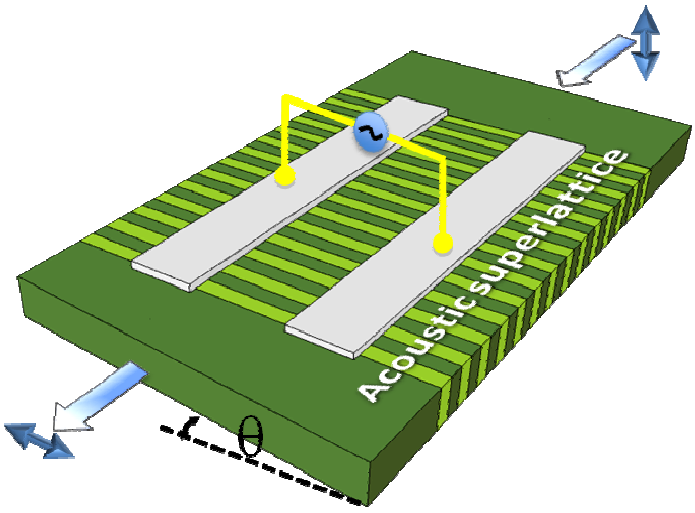

Figure 5.20: Scheme of the proposed bulk AO polarization converter with $\theta = 8^{o}$.

A series of measurements is carried out to determine the characteristics of the AO response. The RF frequency (f_{RF}) is first swept around the resonance frequency f_a = 330 MHz and the output power is measured at the phase-matching. The measurement result is shown in Figure 5.21, with the peak measured at 328 MHz. The same measurement is repeated, but the RF frequency is fixed at the phase-matching frequency, 328 MHz, and the optical wavelength is swept around the expected phase-matching wavelength 1473 nm, and the result is shown in Figure 5.22. For each measurement, the RF input power (P_{RF}) is fixed at 1 W. The measured center wavelength is λ_c = 1472.5 nm determined from Figure 5.22, which is not far from the theoretical value.

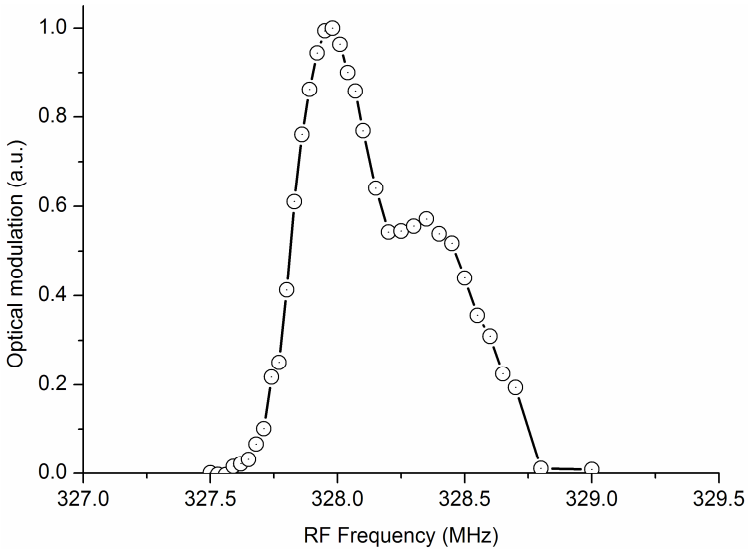

Figure 5.21: AO modulation as a function of RF frequency at center wavelength (around λ=1473 nm) for a P_{RF} of 1 W.

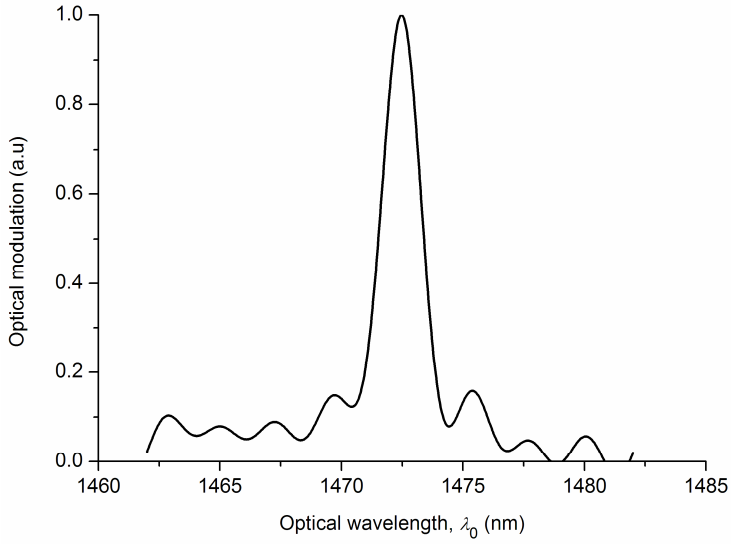

Figure 5.22: Optical modulation as a function of optical wavelength λ_0 for an RF input power of 1 W and RF frequency of 328 MHz.

To determine the performance of the filter, the efficiency (η) measurement is performed by increasing the RF power from 250 mW to 2 W. The RF frequency is fixed at 328 MHz, and the optical wavelength is swept around the center wavelength λ_c = 1472.5 nm. The output optical power is measured at the center wavelength. The results are shown in Figure 5.23. Due to the RF dissipation, as it was described earlier, the center wavelength of the bulk filter is shifted with the RF power (Figure 5.24).

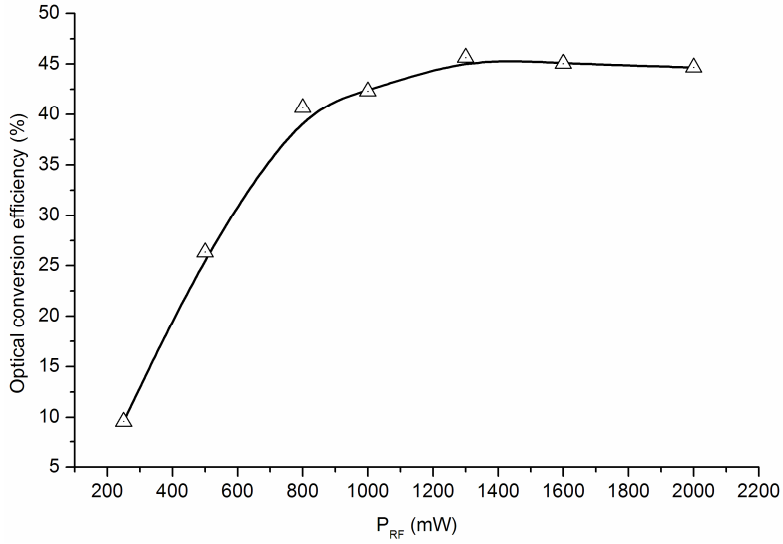

Figure 5.23: Optical conversion efficiency (η) versus RF power (P_{RF}) for the bulk AO filter. The continuous line is a fitting curve to the data.

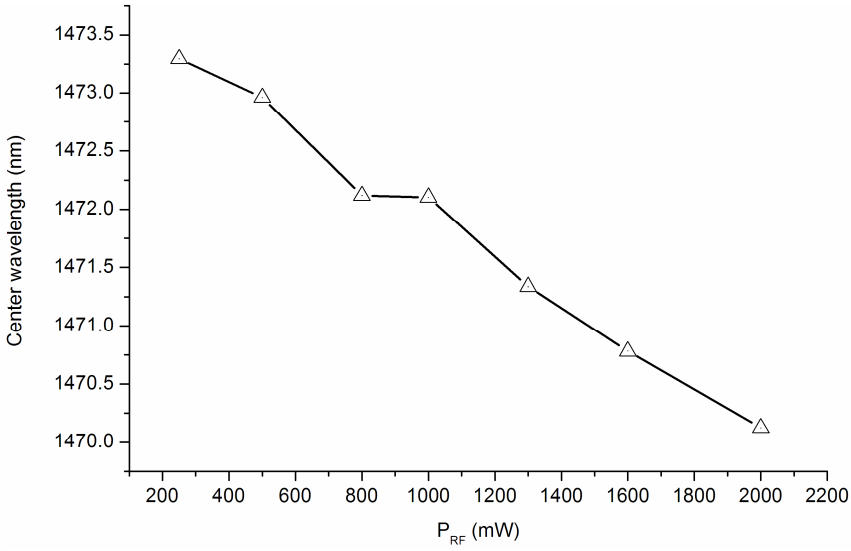

Figure 5.24: Shift of center wavelength (λ_c) observed in different RF power (P_{RF}). The continuous line is a fitting curve to the data.

Clearly, from Figure 5.23, full conversion cannot be reached even at RF power up to 2 W. Comparing to the integrated (waveguide) filter discussed previously, the efficiency of the bulk filter is inferior. The bulk filter's performance could be possibly improved by focusing more the beam onto the substrate surface where the elastic energy of the L-BAW is mostly concentrated. In this way, it could increase the overlap integral between the optical and the acoustic L-BAW beams.

5.5 Optimization of integrated AO filter structures

5.5.1 Introduction

The proof of concept ASL based monolithic integrated and bulk AO filters have been demonstrated in the previous section.

However the RF power required to achieve full polarization conversion is still high, e.g. 1 W for the case of integrated AO filter. So, in this section ways of optimizing the filter's performance particularly with respect to the filter efficiency in terms of driving RF power are presented and discussed.

5.5.2 Coplanar electrodes optimization for high AO coupling

To obtain optimum filter efficiency in accordance with Eq. 1.40 there are two parameters that need to be taken into account: the figure of merit M_2 given by Eq. 2.41 and the acoustical power density $P_A = P_R/w$. As discussed previously, the figure of merit is basically an intrinsic property of the crystal (ZX-$LiNbO_3$) and also of the Ti-$LiNbO_3$ channel waveguide being used to confine the optical mode, the efficiency thereby merely depends on the acoustical power density P_A. There are then two possible ways to increase the power density P_A: either increasing the SAW power P_R or reducing the acoustic beam width w.

The SAW power P_R radiated by the transducer is proportional to the radiation conductance G_a according to Eq. 2.23. Due to the fact that K^2, N, and f_R are usually fixed parameters that are solely determined by the properties of the PPLN structure, it is clear from Eq. 2.23 that the acoustical power P_R can be increased by increasing the static capacitance of the transducer, C_T. The acoustic beam width w can for its part be reduced via lateral confinement of the acoustic displacement that can be accomplished by means of SAW waveguides as pointed out in Chapter 1. For that reason, and given

the profiles of the acoustic mode calculated in Chapter 2, the FWHM of the acoustic beam (w) can be used as a figure of merit to have maximum power conversion efficiency.

In order to set an ASL design that would attain maximum filter efficiency by means of improving the acoustic power density P_A, we performed numerical simulations in COMSOL as outlined in Chapter 3, by considering the following electrode width: W = 60, 80 and 100 µm; and for each width W, the gap G_E is varied from 20 to 100 µm. A lower limit of 20 µm is imposed to the electrode gap in order to ease the fabrication process by leaving enough space to allow for the placement of an optical waveguide with 6 µm lateral width in the metal-free area. The overall length of the device is fixed to 10 mm. A FEM analysis in COMSOL is performed to compute static capacitance C_T of 10 mm length coplanar electrodes and the symmetrical SAW mode, i.e. the fundamental mode, is calculated employing the scalar approximation described in Chapter 2.

In Figure 5.25 we show the calculated capacitance as a function of the electrode gap (G_E). From the figure we can derive that the optimal values for both C_T and w (represented in the plot through the FWHM of the acoustic beam) are obtained when the electrode gap is 20 µm

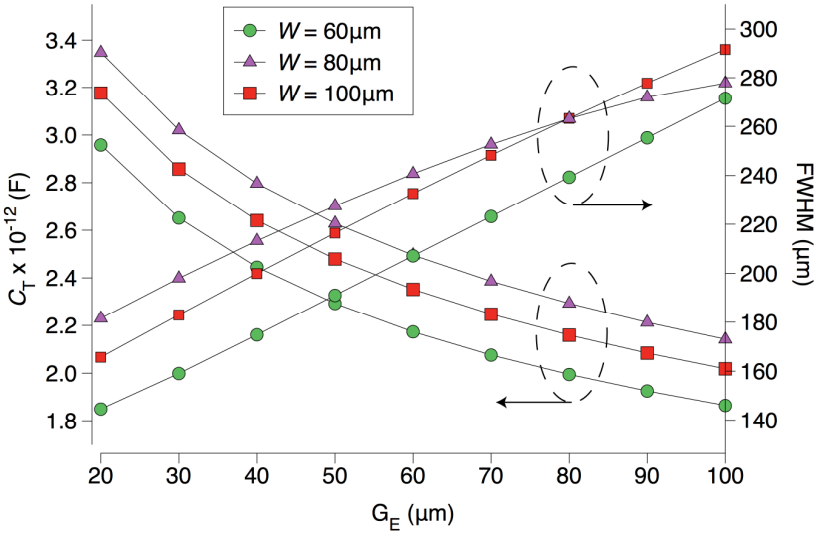

Figure 5.25: Calculated total static capacitance (C_T) (*left*) of the coplanar electrodes on ZX-cut $LiNbO_3$ and full-width-half-maximum (FWHM) of the acoustic beam (*right*) as a function of electrode gap.

Next, in order to find an optimum configuration for the electrodes for low driving power, we computed the AO coupling coefficient κ as given by Eq. 2.43 with l = 0, for varying electrode widths (from 40 to 140 µm), while keeping G_E fixed at 20 µm. To this aim the electromechanical coupling coefficient K^2 of the ASL transducer is assumed to be around 0.53% taken from the value for ZX-$LiNbO_3$ given by Table 1.3. The refractive indices for both TE and TM modes of the 6 µm wide optical waveguide at phase-matched wavelength (center wavelength) λ_c = 1455.5 nm are taken from the simulated results in Chapter 3. The photo-elastic constant p_{41}=0.05 is taken from [22] and we assumed v_R = 3795 m/s. The computed coupling coefficient κ is plotted in Figure 5.26 against

the electrode width *W*. Now, considering all the simulation results, we infer that the optimal configuration, i.e. maximum AO coupling coefficient κ is obtained at W=70 μm at G_E= 20 μm.

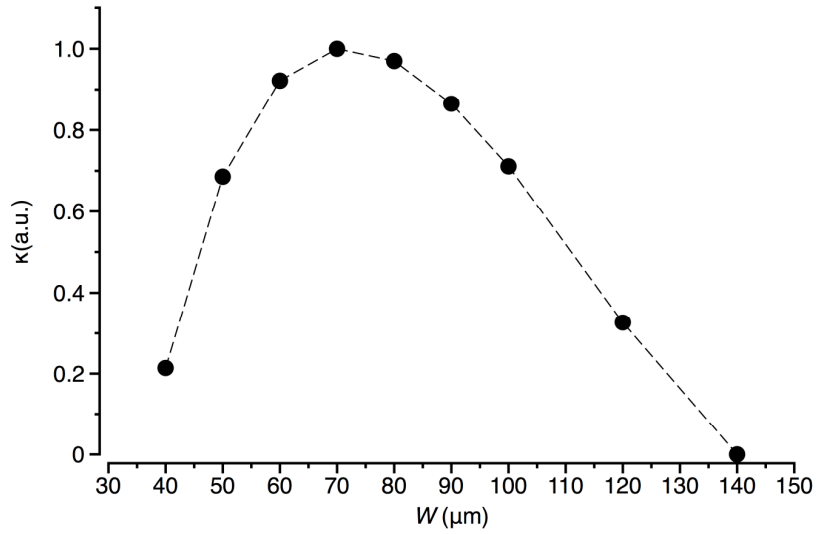

Figure 5.26: Calculated AO coupling coefficient, normalized with the maximum obtained with *W* = 70 μm, as the electrode width varied from 40 to 140 μm, while keeping GE fixed at 20 μm.

Based on the above results, several ASL transducers with different electrode width *W* = 60, 70, and 80 μm and electrode gap (G_E) fixed at 20 μm are fabricated. The AO measurement is performed with the same experimental setup as described in Chapter 4. The measurement results are shown in Figure 5.27.

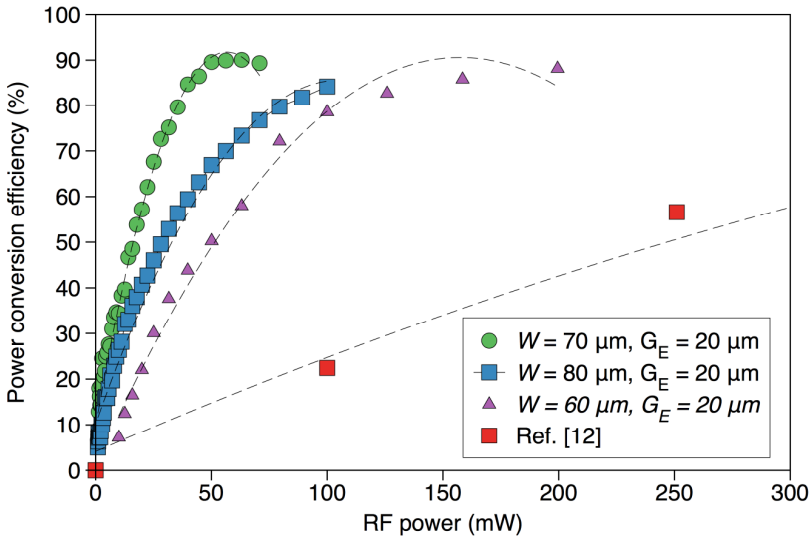

Figure 5.27: Power conversion efficiency versus RF power. Dashed lines are fitting function.

From the figure, we can see that nearly complete optical switching is achieved at low electrical powers (about 50mW) for an ASL transducer having an electrode width W = 70 µm and gap G_E = 20 µm. This result represents an improvement by a factor of 20 compared to previous results shown in Chapter 5. To get an idea of this device performance in terms of power consumption, our AO filter is compared to filter designs reported e.g. in ref. [36]. In this paper, the authors demonstrated a very low power AO filter with a 2mW driving power over a 45 mm length. By scaling our own filter down to the same length, the expected driving power of the proposed ASL filter will be of the order of 10 mW, which compares well with the required power for the filters proposed in [36]].

5.5.3 Mass-loading for diffraction less and confined SAW

As it was pointed out in Chapter 1, SAW devices are commonly based on IDTs deposited on piezoelectric substrates, which generate wide-beam SAW. Diffraction effects, particularly in the case of small acoustic aperture, set the limit for local power densities. SAW waveguides have been proposed as a solution to overcome such issue [27], [30], [31], [36]. In fact, The SAW waveguide term implies a geometrical structure which confines the lateral extent of the SAW. Different methods have been proposed to obtain SAW waveguides for example strip and slot type waveguide realized through mass-loading [27], [36], Ti or proton indiffusion [30], [31]. These techniques allow increasing the acoustic power density, which can in particular lead to an improvement in acousto-optical (AO) coupling for integrated AO filters [24], [27], [30], [31], [36]. Some problems, however, related for instance to acoustic losses associated with mass-loaded waveguides [36] or to a possible increment of optical loss as in Ti-diffused geometries, might reduce the benefit of their use.

In the previous chapter, the ASL transducer has been demonstrated as an alternative for acoustic wave generation, i.e. SAW. It has also been shown from the simulation (see Chapter 3) and experimentally demonstrated by direct imaging of the acoustic displacement with laser interferometry measurement presented in the previous section that the excited SAW generated in an ASL can be localized and confined within the region between the electrodes making ASL transducers easily integrable with optical waveguides,

and thus a good candidate for integrated AO filters. Indeed, the gap between the electrodes in ASL based transducers allows placing the optical waveguide in a metal-free region.

As it was shown in the previous section, the filter performance can be significantly improved by optimizing the geometry of the ASL transducer, which enhances the lateral confinement (w) of the SAW resulting in large acoustic power densities, and hence improving the AO coupling. To enhance even further the lateral confinement (w) of the acoustic field in view of obtaining large acoustic power densities in the gap, a way of confining the SAW is required. As in the case of IDT, confinement of the acoustic power can be achieved by means of mass-loading, which is realized through deposition of materials to decrease the SAW velocity. A further requirement, from an acousto-optical point of view, is that the deposited material needs to be optically transparent in order to prevent optical losses.

Here, localized confinement of SAW field in ASL transducers accomplished through deposition of a stack of thin films made of gold on silica is proposed. The stack acts as a guiding medium on the substrate surface, confining the wave within the gap region between the electrodes. Gold, a high density material, is used as the load to decrease the SAW velocity; the SiO_2 layer acts as a buffer layer for the optical waveguide and aims at preventing optical losses. As reported in ref. [36], the combination of these two layers enables to reduce the SAW velocity of about 3.5%. The aforementioned possible drawbacks associated to mass loading in

IDT-SAW structures, such as additional acoustic and optical losses, are avoided in the proposed mass-loaded ASL.

Figure 5.28 (inset) illustrates the geometry of the device, which consists of an ASL transducer (ASL structure and coplanar electrodes) for SAW excitation, Au/SiO_2 layers for mass-loading, and a Ti-$LiNbO_3$ optical channel waveguide, respectively.

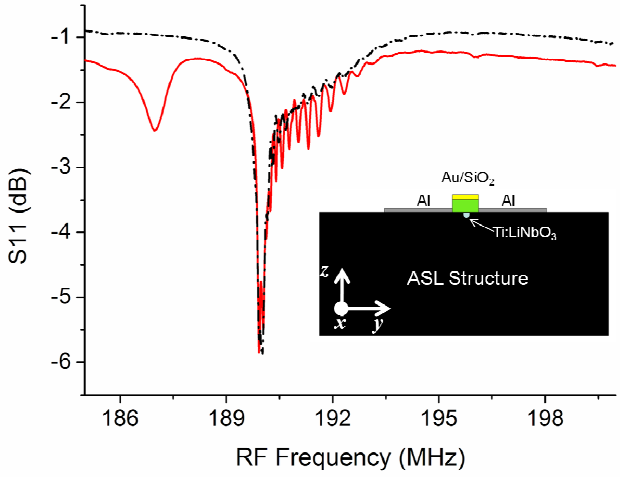

Figure 5.28: Scattering parameter S11 as a function of RF frequency measured for the sample without (black dash-dot line) and with (red solid line) mass loading, respectively. The inset shows 2-D cross section of ASL transducer with multilayer Au/SiO_2 thin films in the gap acting as a lateral guiding medium for the SAW.

In modeling the device, COMSOL simulation is performed and the model structure is defined following the analysis described in Chapter 3. Material constants for Au, Al, and SiO_2 are taken from ref. [39]. The thicknesses of the Au and SiO_2 layers are 150 nm and 400 nm, respectively. Figure 5.29(a) shows that the simulation

result, i.e. that the SAW field is confined within the gap region and its beam width is about 45 µm at a frequency of 187.56 MHz.

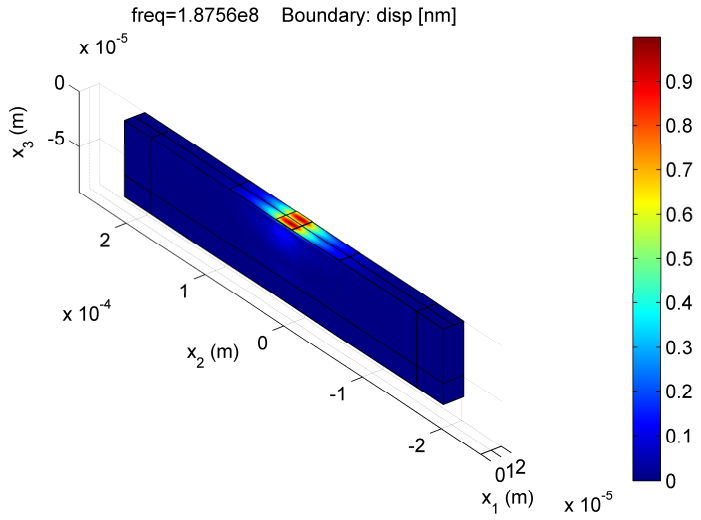

Figure 5.29: Computed normalized displacement profile of the confined SAW at frequency of 187.56 MHz.

We then fabricate the calculated device with the step of fabrication described in Chapter 4. A stack consisting of a 150 nm thick Au layer, deposited onto a 400 nm thick SiO_2 thin film, is deposited on the gap region using a lift-off process (see Chapter 4) to fabricate the acoustic waveguide (20 µm wide and 10 mm long).

In Figure 5.28 we compare the reflection responses (S11 scattering parameter) of the same sample measured, following RF measurement scheme described in Chapter 4, before and after the deposition of the acoustic guiding layer. We can see a strong dip at a resonance frequency around 189.9 MHz in both cases, which corresponds to the expected SAW generation in ZX-$LiNbO_3$. An

additional dip however appears at lower frequency around 187.5 MHz in the mass-loaded sample. This additional dip corresponds to a confined, slower velocity SAW field.

To detect the confinement we have carried out a direct measurement of the elastic displacement field on the mass-loaded sample. A scanning heterodyne laser interferometer with the measurement setup described in Chapter 4 is employed to obtain a map of the out-of-plane component of the surface acoustic wave motion at 187.5 MHz, i.e. where the additional dip in the electrical response is observed. The measurements are reported in Figure 5.30 (b), along with a microscope picture of the sample (Figure 5.30 (a)) on the same scale, which can be used as a reference for locating the elastic field in the device. The measured acoustic beam width is about 40 μm at its maximum and is close to the theoretical prediction

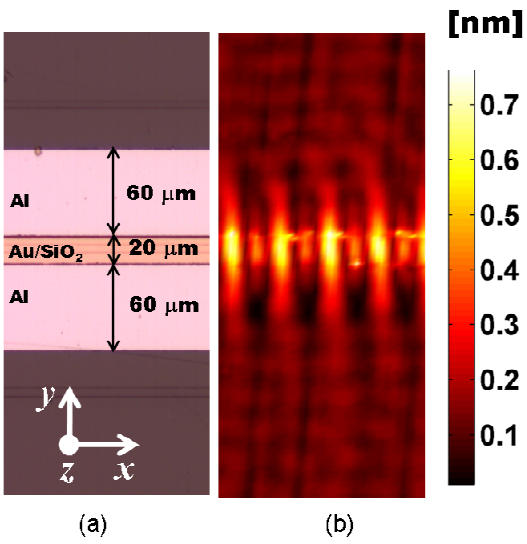

Figure 5.30: (a) A microscope picture of the sample(b) Displacement profile of confined SAW field scanned with laser interferometry at RF frequency of 187.5 MHz.

To further investigate the characteristic of the confined SAW field and to demonstrate at the same time its potential application to AO filters, we have performed AO polarization conversion. The characterization setup and the measurement steps are described in Chapter 4. For comparison we characterize both samples, with and without mass loading, in order to evaluate the impact of SAW confinement in terms of reduction of the driving RF power (P_{RF}) required for maximum mode conversion. The polarization conversion efficiency (η) is then measured as a function of the RF power at the phase- matching wavelength centered around 1456 nm. The results are shown in Figure 5.31, for values of P_{RF} ranging from 1 mW to 300 mW. We can estimate that the maximum conversion (about 90%) is achieved at about 200 mW RF power for the unloaded sample at a frequency of 189.9 MHz, while 70 mW RF

power is sufficient in the case of the mass-loading ASL device at a frequency of 187.5 MHz. The SAW confinement hence induces a significant enhancement of the polarization conversion efficiency by a factor of 3. The output optical intensity as a function of optical wavelength is then measured for the sample with mass loading at an input RF power of 63 mW. The obtained results, reported in Figure 5.31(inset), show that the 3-dB optical bandwidth (FWHM) is of the order of 2.57 nm, which corresponds to an AO interaction length of 9.7 mm, as it is estimated using Eq. 2.45. This value is very close to the physical ASL transducer length of 10 mm, which implies that the SAW confinement is across the entire physical length of the transducer and acoustic and optical losses are negligible.

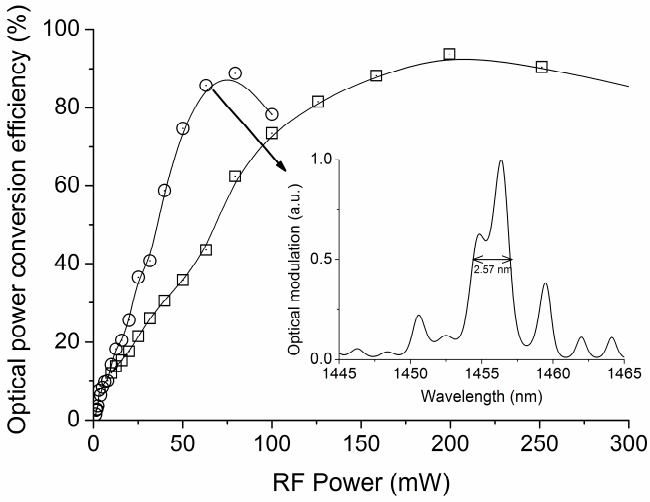

Figure 5.31: Optical power conversion efficiency as a function of electrical (RF) power: for mass-loaded sample (circles) and unloaded, reference, samples (rectangles). The inset shows output optical intensity modulation as a function of optical wavelength measured on mass loaded sample at RF power of 63 mW and frequency of 187.5 MHz.

Chapter 6 - Conclusions and future outlook

6.1 Main thesis results

Acoustic superlattices (ASLs) made of periodically poled ZX-cut lithium niobate (PPLN) associated with coplanar electrodes called ASL transducers have been proposed and investigated for the first time as an effective alternative for SAW generation. Two modeling techniques, i.e. scalar approximation and FEM analysis (2-D and 3-D modeling) implemented in COMSOL MULTIPHYSICS, have been developed and employed to examine the acoustic transduction in the ASL transducer. Both techniques give similar results with respect to the characteristics of generated SAW modes. The calculated results obtained with the 3-D FEM simulation confirm the Rayleigh nature of the generated SAW, showing that the excited SAW in the ASL is similar to that of its IDT counterparts.

From the propagation analysis in 2-D FEM simulation, it has been shown that in addition to the SAW, the ASL transducer excites longitudinal bulk acoustic wave (L-BAW). This analysis also shows that the SAW excitation in the ASL transducer is mainly induced by the E_3 electric field component, whereas the E_2 component induces the excitation of the L-BAW. Moreover, the 2-D model shows that the SAW excited by the ASL transducer does not propagate but it is rather confined within the transducer.

Several ASL transducers, with different lattice periods, have been realized and characterized, also to validate the modeling and design tools. One and two-port electrical measurements have been performed to evaluate the electro-acoustic response. In addition laser interferometry has been carried out to determine the out-of-plane component of the SAW displacement. With respect to the standard IDT configuration using the same crystal orientation, the efficiency of the SAW generation in the proposed designs is similar, while, for the same grating period, the resonance frequency that can be achieved is two times larger. In addition to the SAW, unlike its IDT counterparts, the ASL transducer can excite the L-BAW, as it had been predicted by the modeling. The two-port measurements have shown that the SAW signal collected at the receiver is small, indicating that the SAW energy remains essentially confined within the transmitter. This experimental result too is in agreement with the aforementioned theoretical predictions.

After the experimental validation of the modeling, AO filters incorporating the ASL transducer have been designed and fabricated. ASL structures with 20 μm period and coplanar electrodes have been realized along with 6 μm wide Ti-$LiNbO_3$ optical channel waveguide. In that way monolithic and integrated (waveguide) SAW based AO filters and L-BAW based bulk AO filters have been demonstrated. As for integrated SAW based AO filter, a 3-dB optical bandwidth of 2.5 nm, center wavelength of 1456 nm, and -20 dB distance of 14.49 nm are obtained at the SAW resonance frequency of 189.94 MHz. Such filter requires 1 W RF

power to achieve nearly complete polarization conversion. As for the bulk AO filter, a center wavelength of 1472.5 nm is measured at the L-BAW resonance frequency of 328 MHz. In the bulk AO filter, full conversion cannot be reached even at RF power up to 2 W. Comparing to the integrated (waveguide) filter, the efficiency of the bulk filter is significantly lower. The AO filter's central wavelength can be tuned by changing the RF power.

Several designs to improve the AO filter efficiency have been investigated. By optimizing the ASL transducer (coplanar electrodes with electrode width of 70µm and gap of 20µm), nearly complete optical switching at very low electrical powers (50mW) has been obtained, this corresponding to an improvement factor of 20 compared to previous results. An appropriate mass-loading, placed on the surface and in between the electrodes of a coplanar $LiNbO_3$ ASL, has allowed achieving strong lateral confinement of the acoustic field, thus leading to a significant improvement of the AO filter performance.

6.2 Future outlook

6.2.1 ASL transducer

ZY-$LiNbO_3$ based ASL transducer

With respect to the ASL transducer, the ZX-$LiNbO_3$ substrate used in the experiment is in fact the cut that has the lowest electromechanical coupling coefficient (see Table 2.3). Since the electric poling technique, considered to be the most feasible

technology for PPLN fabrication in this work, works mainly for Z-cut $LiNbO_3$ substrate, so the ZY-$LiNbO_3$ (domain walls parallel to x_1 axis) having $K^2 = 2.25\%$ (see Table 2.3), which is almost 5 times larger that that of ZX-$LiNbO_3$, can be considered as an alternative substrate. One problem with ZY-$LiNbO_3$ is that the domain walls would be in the x_3-x_1 plane, sometimes difficult to achieve since the natural inversion under electric field is on the x_3-x_2 plane.

Sub-wavelength SAW confinement

Apart from the mass-loading waveguide, the lateral SAW confinement may also be achieved with a defect line in the ASL structure. The fact that the SAW is not propagating in the ASL transducer suggests that the ASL structure supports a bandgap for the SAW. In fact, the presence of the bandgap in the ASL structure has been demonstrated in [58] for the case of plate wave. So, assuming that the ASL indeed supports the bandgap, one can introduce a line defect in the gap region, which is similar to the line defect in phononic crystals waveguide [59]. Here the line defect is basically an unpoled $LiNbO_3$ section. In this way, sub-wavelength SAW confinement can in principle be achieved.

6.2.2 Integrated AO filters

Despite the reported improvements in terms of RF power reduction, the ASL based integrated AO filters investigated in this thesis still present large bandwidth ($\Delta\lambda_{FWHM} > 2$ nm) and relatively large cross-talk ($\Delta\lambda_{-20dB} = 14$ nm). In addition they are not efficiently tunable. Indeed, the tuning mechanism can be somewhat

achieved via RF power, however, it is not controllable and inefficient due to thermal dissipation. The dependency on the polarization of the incoming light beam limits the applicability of these devices in several specific applications, for example when they are placed in-line in an optical telecommunication link. For these reasons the proposed devices require further development for WDM applications, this being certainly a future task.

Filter bandwidth

According to Eq. 2.45 the filter bandwidth ($\Delta\lambda_{FWHM}$) can be reduced by increasing the device length. For example a bandwidth of 1 nm can be achieved if the active filter length is 20 mm (see Figure 3.27). In general, the longer the length the higher the attenuation of the SAW. This would limit the expected efficiency improvement (half of power consumption) associated to a longer active length. However, in our case, the elastic energy does not propagate, so the attenuation effects are reduced. Furthermore, improving the filer bandwidth will also consequently improve the cross-talk ($\Delta\lambda_{-20dB}$). Using Eq. 2.37, a cross-talk as low as 6.28 nm could be achieved.

Tuning mechanism

Wavelength tuning can be achieved by using a chirped ASL structure, for example 5 nm/MHz tuning range can be obtained according to Figure 3.28. In this case, if one wants to maintain the

bandwidth and efficiency, the overall device length must be increased.

Apart from the chirped ASL, employing the defect line ASL structure described previously in conjunction to mass-loading with SiO_2/Au stack opens up another design of integrated AO tunable filter. The tuning can be achieved by the electro-optic (EO) effect. In fact, the line defect between the coplanar electrodes allows placing the optical waveguide under uniform domain, so that the EO effect will induce a refractive index change $\delta(|N_E - N_M|)$, given by

$$\delta(|N_E - N_M|) \approx \frac{1}{2} N_M^3 r_{33} \frac{V_{DC}}{\tau} \quad (7$$

where V_{DC}, $r_{33,}$ and τ are the applied DC voltage, EO coefficient, and penetration depth of DC field, respectively. Here, the overlap integral between the DC field and the optical field is assumed to be 1. By substituting Eq. 7.1 into Eq. 2.41 and omitting the dispersion term in Eq. 2.41, the EO tuning rate is given by

$$\frac{d\lambda_T}{dV_{DC}} \approx N_M^3 r_{33} \frac{\Lambda}{\tau} \quad (7$$

Polarization independent operation

Polarization independent AO filters can be achieved by using polarization beam splitters (PBS) or directional couplers that are placed at the device input and the output. The input PBS will split

the incoming signals into two branches based on their state of polarization (TE or TM polarized mode), while the output PBS will combine the converted signals.

6.2.3 Emerging application of ASL transducers

Apart from the fields directly related to the thesis work, the ASL structures offer other possible applications. We will list a few of them in the following paragraphs.

For example the metal free region between the electrodes of our transducer can be used as an active region to place nanostructures for enhancing the sensitivity of SAW based sensors. Compared with SAW delay line based SAW sensor using two IDTs (two-port device) [60], using the ASL allows the sensor to be realized in one-port configuration (reflective mode). This configuration is more compact. The mass-loading ASL structure (Figure 5.28) can also be used for launching surface plasmon polaritons (SPPs). Unlike passive metallic grating [61], the grating can be made active by the SAW. This will make it possible an electrically switchable SPP launcher. The first demonstration of active SPP launcher has been presented in [62], in which the IDT and metallic gold strip are employed and placed at a certain distance from each other. This would be the first time that ASL transducer are employed for this double purpose.

The fact that with ASLs one can launch traveling L-BAW may also find interesting applications in medical imaging, nondestructive

testing, and L-BAW delay line. For delay lines, for example, ASL structures based on “crossed-field” configuration have been demonstrated in ref. [63]. In these structures the electrodes gap is fixed by the physical dimensions of the crystal. In the ASL transducer proposed by this thesis the distance between the electrodes can be designed with high flexibility since it is photo lithographically defined.

References

[1] G. Keiser, *Optical Fiber Communications*, 4th ed. McGraw-Hill Science/Engineering/Math, 2010.

[2] M. J. O'Mahony, "Optical multiplexing in fiber networks: progress in WDM and OTDM," *Communications Magazine, IEEE*, vol. 33, no. 12, pp. 82-88, 1995.

[3] G. E. Keiser, "A Review of WDM Technology and Applications," *Optical Fiber Technology*, vol. 5, no. 1, pp. 3-39, Jan. 1999.

[4] M. S. Borella, J. P. Jue, D. Banerjee, B. Ramamurthy, and B. Mukherjee, "Optical components for WDM lightwave networks," *Proceedings of the IEEE*, vol. 85, no. 8, pp. 1274-1307, 1997.

[5] M. K. Smith, A. M. J. Koonen, H. Herrmann, and W. Sohler, "Wavelength-selective device," in *Fibre Optic Communication Devices*, vol. 4, Berlin: Springer-Verlag, 2001, pp. 262-312.

[6] C. A. Brackett, "Dense wavelength division multiplexing networks: principles and applications," *Selected Areas in Communications, IEEE Journal on*, vol. 8, no. 6, pp. 948-964, 1990.

[7] R. M. White and F. W. Voltmer, "DIRECT PIEZOELECTRIC COUPLING TO SURFACE ELASTIC WAVES," *Applied Physics Letters*, vol. 7, no. 12, p. 314, 1965.

[8] D. Royer and E. Dieulesaint, *Elastic Waves in Solids: Generation, acousto-optic interaction, applications*. Springer, 2000.

[9] V. P. Plessky and C. S. Hartmann, "Characteristics of leaky SAWs on 36-LiTaO3 in periodic structures of heavy electrodes," in *Ultrasonics Symposium, 1993. Proceedings., IEEE 1993*, 1993, pp. 1239-1242 vol.2.

[10] T. Makkonen, V. P. Plessky, W. Steichen, and M. M. Salomaa, "Surface-acoustic-wave devices for the 2.5–5 GHz frequency range based on longitudinal leaky waves." 2003.

[11] A. Isobe, M. Hikita, and K. Asai, "Q values of longitudinal leaky SAWs propagating on rotated Y-cut LN substrates along the perpendicular to the X axis," *Ultrasonics, Ferroelectrics and Frequency Control, IEEE Transactions on*, vol. 52, no. 10, pp. 1812-1816, 2005.

[12] T. Sato and H. Abe, "Propagation properties of longitudinal leaky surface waves on lithium tetraborate," in *Ultrasonics Symposium, 1994. Proceedings., 1994 IEEE*, 1994, vol. 1, pp. 287-292 vol.1.

[13] A. Isobe, M. Hikita, and K. Asai, "Propagation characteristics of longitudinal leaky SAW in Al-grating structure," *Ultrasonics, Ferroelectrics and Frequency Control, IEEE Transactions on*, vol. 46, no. 4, pp. 849-855, 1999.

[14] Y.-yuan Zhu, N.-ben Ming, W.-hua Jiang, and Y.-an Shui, "Acoustic superlattice of LiNbO3 crystals and its applications to bulk-wave transducers for ultrasonic generation and detection up to 800 MHz," *Applied Physics Letters*, vol. 53, no. 15, p. 1381, 1988.

[15] Y.-yuan Zhu, Y.-feng Chen, S.-ning Zhu, Y.-qiang Qin, and N.-ben Ming, "Acoustic superlattices and ultrasonic waves excited by crossed-field scheme," *Materials Letters*, vol. 28, no. 4-6, pp. 503-505, Oct. 1996.

[16] E. L. Wooten, R. L. Stone, E. W. Miles, and E. M. Bradley, "Rapidly tunable narrowband wavelength filter using LiNbO3 unbalanced Mach-Zehnder interferometers," *Lightwave Technology, Journal of*, vol. 14, no. 11, pp. 2530-2536, 1996.

[17] J. Sapriel, D. Charissoux, V. Voloshinov, and V. Molchanov, "Tunable acoustooptic filters and equalizers for WDM applications," *Lightwave Technology, Journal of*, vol. 20, no. 5, pp. 892-899, 2002.

[18] V. Y. Molchanov, V. B. Voloshinov, and O. Y. Makarov, "Quasi-collinear tunable acousto-optic paratellurite crystal filters for wavelength division multiplexing and optical channel selection," *Quantum Electronics*, vol. 39, no. 4, pp. 353-360, Apr. 2009.

[19] K. B. Yushkov, S. Dupont, J.-C. Kastelik, and V. B. Voloshinov, "Polarization-independent imaging with an acousto-optic tandem system," *Optics Letters*, vol. 35, no. 9, pp. 1416-1418, May. 2010.

[20] C. S. Qin, G. C. Huang, K. T. Chan, and K. W. Cheung, "Low drive power, sidelobe free acousto-optic tunable filters/switches," *Electronics Letters*, vol. 31, no. 15, pp. 1237-1238, 1995.

[21] J.-C. Kastelik, H. Benaissa, S. Dupont, and M. Pommeray, "Acousto-optic tunable filter using double interaction for sidelobe reduction," *Applied Optics*, vol. 48, no. 7, p. C4-C10, Mar. 2009.

[22] H. Gnewuch, N. K. Zayer, C. N. Pannell, G. W. Ross, and P. G. R. Smith, "Broadband monolithic acousto-optic tunable filter," *Optics Letters*, vol. 25, no. 5, pp. 305-307, Mar. 2000.

[23] S. E. Harris, S. K. T. Nieh, and D. K. Winslow, "Electronically tunable acousto-optic filter," in *Electron Devices Meeting, 1969 International*, 1969, vol. 15, pp. 70-72.

[24] D. A. Smith, J. E. Baran, J. J. Johnson, and K.-W. Cheung, "Integrated-optic acoustically-tunable filters for WDM networks," *Selected Areas in Communications, IEEE Journal on*, vol. 8, no. 6, pp. 1151-1159, 1990.

[25] K. Yamanouchi, K. Higuchi, and K. Shibayama, "TE‐TM mode conversion by interaction between elastic surface waves and a laser beam on a metal‐diffused optical waveguide." 1976.

[26] H. F. Taylor and O. Eknoyan, "Guided Wave Acousto-Optic and Electro-Optic Tunable Filter Designs with Relaxed Beam-Splitter Requirements," *Applied Optics*, vol. 39, no. 1, pp. 124-128, Jan. 2000.

[27] T. Nakazawa, S. Taniguchi, and M. Seino, "Ti:LiNbO3 acousto-optic tunable filter (AOTF)," *Fujitsu Scientific and Technical Journal*, vol. 35, no. 1, pp. 107-112, 1999.

[28] Le Binh and J. Livingstone, "A wide-band acoustooptic TE-TM mode converter using a doubly confined structure," *Quantum Electronics, IEEE Journal of*, vol. 16, no. 9, pp. 964-971, 1980.

[29] A. Kar-Roy and C. S. Tsai, "Integrated acoustooptic tunable filters using weighted coupling," *Quantum Electronics, IEEE Journal of*, vol. 30, no. 7, pp. 1574-1586, 1994.

[30] V. P. Hinkov, R. Opitz, and W. Sohler, "Collinear acoustical TM-TE mode conversion in proton exchanged Ti:LiNbO/sub 3/ waveguide structures," *Journal of Lightwave Technology*, vol. 6, no. 6, pp. 903-908, Jun. 1988.

[31] H. Herrmann, P. Mu̇ller-Reich, V. Reimann, R. Ricken, H. Seibert, and W. Sohler, "Integrated optical TE-and TM-pass, acoustically tunable, double-stage wavelength filters in LiNBO3," *Electronics Letters*, vol. 28, no. 7, p. 642, 1992.

[32] K. W. Cheung, S. C. Liew, C. N. Lo, D. A. Smith, J. E. Baran, and J. J. Johnson, "Simultaneous five-wavelength filtering at 2.2 nm wavelength separation using integrated-optic acousto-optic tunable filter with subcarrier detection," *Electronics Letters*, vol. 25, no. 10, pp. 636-637, 1989.

[33] H. Sasaki, "Efficient acousto-optic TE⇄TM mode conversion in ZnO films," *Applied Physics Letters*, vol. 25, no. 9, p. 476, 1974.

[34] Y. Ohmachi and J. Noda, "LiNbO3TE-TM mode converter using collinear acoustooptic interaction," *Quantum Electronics, IEEE Journal of*, vol. 13, no. 2, pp. 43-46, 1977.

[35] L. N. Binh and J. Livingstone, "Optimisation of a collinear acoustooptic TEm-TEn mode convertor LiNbO3," *Microwaves, Optics and Antennas, IEE Proceedings H*, vol. 127, no. 6, pp. 323-329, 1980.

[36] O. A. Peverini, H. Herrmann, and R. Orta, "Film-loaded SAW waveguides for integrated acousto-optical polarization converters," *Ultrasonics, Ferroelectrics and Frequency Control, IEEE Transactions on*, vol. 51, no. 10, pp. 1298-1307, 2004.

[37] H. Herrmann, U. Rust, and K. Schafer, "Tapered acoustical directional couplers for integrated acousto-optical mode converters with weighted coupling," *Lightwave Technology, Journal of*, vol. 13, no. 3, pp. 364-374, 1995.

[38] G. Kovacs, M. Anhorn, H. E. Engan, G. Visintini, and C. C. W. Ruppel, "Improved material constants for LiNbO3 and LiTaO3," pp. 435-438 vol.1, Dec. 1990.

[39] B. A. Auld, *Acoustic Fields and Waves in Solids*, 2nd ed. Krieger Pub Co, 1990.

[40] K. Iga and Y. Kokubun, *Encyclopedic Handbook of Integrated Optics*, 1st ed. CRC Press, 2005.

[41] C. Campbell, *Surface acoustic wave devices for mobile and wireless communications*. Academic Press, 1998.

[42] D. Morgan, *Surface Acoustic Wave Filters, Second Edition: With Applications to Electronic Communications and Signal Processing*, 2nd ed. Academic Press, 2007.

[43] D. Ciplys and R. Rimeika, "Measurements of electromechanical coupling coefficient for surface acoustic waves in proton-exchanged lithium niobate," *ULTRAGARSAS*, vol. 33, no. 3, pp. 14-20, 1999.

[44] A. A. Oliner, *Acoustic surface waves*. Springer-Verlag, 1978.

[45] J. Xu and R. Stroud, *Acousto-Optic Devices: Principles, Design, and Applications*. Wiley-Interscience, 1992.

[46] Goutzoulis, *Design and Fabrication of Acousto-optic Devices*, 1st ed. CRC Press, 1994.

[47] W. P. Mason, *Electromechanical Transducers and Wave Filters*. Van Nostrand, 1942.

[48] M. V. Hobden and J. Warner, "The temperature dependence of the refractive indices of pure lithium niobate," *Physics Letters*, vol. 22, no. 3, pp. 243-244, Aug. 1966.

[49] S. Fouchet, A. Carenco, C. Daguet, R. Guglielmi, and L. Riviere, "Wavelength dispersion of Ti induced refractive index change in LiNbO3as a function of diffusion parameters," *Lightwave Technology, Journal of*, vol. 5, no. 5, pp. 700-708, 1987.

[50] E. Strake, G. P. Bava, and I. Montrosset, "Guided modes of Ti:LiNbO3 channel waveguides: a novel quasi-analytical technique in comparison with the scalar finite-element method," *Lightwave Technology, Journal of*, vol. 6, no. 6, pp. 1126-1135, 1988.

[51] H. Berends, "Integrated Optical Bragg Reflectors as Narrowband Wavelength Filters," University of Twente, 1997.

[52] J. Amin, V. Pruneri, J. Webjörn, P. S. J. Russell, D. C. Hanna, and J. S. Wilkinson, "Blue light generation in a periodically poled Ti:LiNbO3 channel waveguide," *Optics Communications*, vol. 135, no. 1-3, pp. 41-44, Feb. 1997.

[53] P. Vairac and B. Cretin, "Electromechanical resonator in scanning microdeformation microscopy: theory and experiment," *Surface and Interface Analysis*, vol. 27, no. 5-6, pp. 588-591, May. 1999.

[54] P. Suchoski and R. Ramaswamy, “Minimum-mode-size low-loss Ti: LiNbO3channel waveguides for efficient modulator operation at 1.3 μm,” *Quantum Electronics, IEEE Journal of*, vol. 23, no. 10, pp. 1673-1679, 1987.

[55] G. Eisenstein, S. K. Korotky, L. W. Stulz, R. M. Jopson, and K. L. Hall, “Antireflection coatings on lithium niobate waveguide devices using electron beam evaporated yttrium oxide,” *Electronics Letters*, vol. 21, no. 9, pp. 363-364, Apr. 1985.

[56] R. Rimeika, D. Ciplys, P. Kazdailis, and M. S. Shur, “Anisotropic acousto-optic diffraction by leaky wave radiation in ZX-LiNbO3.” 2007.

[57] Yu Jin and S. G. Joshi, “Propagation of a quasi-shear horizontal acoustic wave in Z-X lithium niobate plates [and conductivity sensor application],” *Ultrasonics, Ferroelectrics and Frequency Control, IEEE Transactions on*, vol. 43, no. 3, pp. 491-494, 1996.

[58] I. V. Ostrovskii, A. B. Nadtochiy, and V. A. Klymko, “Velocity dispersion of plate acoustic waves in a multidomain phononic superlattice,” *Physical Review B*, vol. 82, no. 1, p. 014302, Jul. 2010.

[59] J. O. Vasseur, P. A. Deymier, B. Djafari-Rouhani, Y. Pennec, and A.-C. Hladky-Hennion, “Absolute forbidden bands and waveguiding in two-dimensional phononic crystal plates,” *Physical Review B*, vol. 77, no. 8, p. 085415, Feb. 2008.

[60] Y. L. Rao and G. Zhang, “Enhancing the Sensitivity of SAW Sensors with Nanostructures,” *Current Nanoscience*, vol. 2, pp. 311-318, Nov. 2006.

[61] J. Renger, R. Quidant, N. van Hulst, S. Palomba, and L. Novotny, “Free-Space Excitation of Propagating Surface Plasmon Polaritons by Nonlinear Four-Wave Mixing,” *Physical Review Letters*, vol. 103, no. 26, p. 266802, Dec. 2009.

[62] C. Ruppert, J. Neumann, J. B. Kinzel, H. J. Krenner, A. Wixforth, and M. Betz, "Surface acoustic wave mediated coupling of free-space radiation into surface plasmon polaritons on plain metal films," *Physical Review B*, vol. 82, no. 8, p. 081416, 2010.

[63] R.-C. Yin, S.-Y. Yu, C. He, M.-H. Lu, and Y.-F. Chen, "Bulk acoustic wave delay line in acoustic superlattice," *Applied Physics Letters*, vol. 97, no. 9, p. 092905, 2010.

List of publications

D. Yudistira, D. Faccio, C. Corbari, P.G. Kazansky, S. Benchabane, and V. Pruneri, "Electric surface potential and frozen-in field direct measurements in thermally poled silica," *Applied Physics Letters*, vol. 92, 2008, p. 012912.

D. Yudistira, S. Benchabane, D. Janner, and V. Pruneri, "Surface acoustic wave generation in ZX-cut LiNbO[sub 3] superlattices using coplanar electrodes," *Applied Physics Letters*, vol. 95, 2009, p. 052901 (**Cover page**)

D. Yudistira, D. Janner, S. Benchabane, and V. Pruneri, "Integrated acousto-optic polarization converter in a ZX-cut LiNbO3 waveguide superlattice," *Optics Letters*, vol. 34, Oct. 2009, pp. 3205-3207.

D. Yudistira, D. Janner, S. Benchabane, and V. Pruneri, "Low power consumption integrated acousto-optic filter in domain inverted LiNbO3 superlattice," *Optics Express*, vol. 18, Dec. 2010, pp. 27181-27190.

D. Yudistira, S. Benchabane, D. Janner, and V. Pruneri, "Diffraction less and strongly confined surface acoustic waves in domain inverted LiNbO3 superlattices," *Applied Physics Letters*. (*accepted for publication*)

D. Yudistira, D. Janner, V. Pruneri, "Integrated acoustic and acousto-optic filters using domain inversion," ECIO -European conference on integrated optics-, Cambridge, UK, April 7-9, 2010.

D. Yudistira, D. Faccio, C. Corbari, P. G. Kazansky, S. Benchabane, V. Pruneri, "Electric surface potential and frozen-in field measurements in thermally poled silica," Bragg Gratings, Photosensitivity and Poling in Glass Waveguides (BGPP) and the Nonlinear Photonics (NP), Quebec, Canada, 2007.